Modeling of phonon- and Coulomb-mediated capture processes in quantum dots

Magnúsdóttir, Ingibjörg

Publication date:
2003

Document Version
Publisher's PDF, also known as Version of record

Modeling of phonon- and Coulomb-mediated capture processes in quantum dots

Ph. D. Thesis

Ingibjörg Magnúsdóttir

COM, Technical University of Denmark
November 2002

In memory of my father

Abstract

This thesis describes modeling of carrier relaxation processes in self-assembled quantum-dot structures, with particular emphasis on carrier capture processes in quantum dots.

Relaxation by emission of longitudinal optical (LO) phonons is very efficient in bulk semiconductors and nanostructures of higher dimensionality. Here, we investigate carrier capture processes into quantum dots, mediated by emission of one and two LO phonons. In these investigations it is assumed that the dot is empty initially. In the case of single-phonon capture we also investigate the influence of the presence of a charge in the quantum-dot state to which the capture takes place. In general, capture rates are of the same order as capture rates into an empty dot state, but in some cases the dot-size interval for which the capture process is energetically allowed, is considerably reduced.

The above calculations are performed by assuming that the incident carrier is a free carrier described by a plane wave. Therefore, the influence of waves scattered by the quantum dot have been neglected. At certain wavelengths and dot sizes, the quantum dot can act as a Fabry-Perot mirror in which the incident carrier travels back and forth in the dot leading to a *quasi-bound* state of finite linewidth that resembles the bound states. We investigate the coupling of carriers in quasi-bound states with LO phonons and demonstrate that they can couple strongly with phonons. This leads to the formation of a mixed carrier-phonon mode that is called a *polaron*.

Capture processes mediated by carrier-carrier scattering (Auger processes) are investigated and their dependence on quantum-dot geometry is studied in detail.

Résumé

Denne afhandling omhandler modellering af relaxations mekanismer i selvdannede kvantepunktstrukturer, med vægt på ladningsbærerindfanging i kvantepunkter.

Relaxation med udsendelse af LO fononer er meget effektiv i halvlederstrukturer af højere dimensionalitet. Her er ladningsbærerindfangning med udsendelse af en eller to LO fononer undersøgt. Vi antager i disse undersøgelser at punktet er tomt før indfangningen finder sted. I tilfælde af indfangning med udsendelse af en fonon, undersøger vi indflydelsen af at en ladningsbærer er til stede i punkttilstanden før indfangningen finder sted. Generelt er tidsskalaen for denne procés den samme som for indfanging i en tom punkttilstand, men i nogen tilfælde er intervallet af punktstørrelser, hvor indfangningen er tilladt, væsentligt formindsket.

Disse beregninger er lavet med den antagelse at den indkommende ladningsbærer er fri, d. v. s. beskrevet med en planbølge. Ved visse punktstørrelser og bølgelængder for den indkommende ladningsbærer kan punktet virke som et Fabry-Perot spejl hvori ladningsbæreren er reflekteret frem og tilbage. Det kan give anledning til en *kvasi-bunden* tilstand med endelig liniebredde der ligner de bundne tilstande. Vi undersøger vekselvirkningen af ladningsbærere i kvasi-bundne tilstande med LO fononer og viser at de kan vekselvirke stærkt med fononer. Dette giver anledning til dannelsen af en blandet ladningsbærer-fonon mode man kalder en *polaron.*

Indfangningsprocesser formidlet af Coulomb-spredning (Auger processer) er undersøgt og deres afhængighed af kvantepunktgeometrien er undersøgt i detaljer.

Acknowledgments

The work presented in this thesis was carried out at Research Center COM, Technical University of Denmark (DTU), in the optoelectronics group headed by Prof. Jørn M. Hvam. The work was funded by a Ph. D. grant from DTU. I am very grateful for having obtained this grant to pursue the studies that are presented here. The work was carried out under the supervision of Prof. Jesper Mørk. Co-supervisors were Associate Research Professor Svend Bischoff, now with Alight Technologies, and Prof. Jørn M. Hvam. I owe them many thanks for their support and good input throughout the project. Jesper's insight into semiconductor physics and his 'down-to-earth' explanations have helped me many times during the project. Svend's assistance and general interest in my work is equally appreciated. I am indebted to Alexander Uskov – Sasha – who initiated most of the work presented in this thesis. Many good discussions have taken place with him throughout the project. Prof. Bjarne Tromborg is gratefully acknowledged for good collaboration and to the point input in many aspects of my work. Lone Bjørnstjerne, the optoelectronics group secretary, deserves special thanks for taking care of the practical aspects in daily work.

Part of this work was carried out at my two-month visit to the group of Prof. Gérald Bastard and Robson Ferreira at the Laboratoire de Physique et de la Matière Condensée (LPMC) de l'Ecole Normale Supérieure in Paris. I am indebted to them for their hospitality and the many things that they taught me. Many thanks go to Angela Vasanelli at the LPMC for good companionship and for helping me finding a place to stay. Fruitful discussions with the polaron expert, Olivier Verzelen, are gratefully acknowledged.

Many thanks to my office mates, Tommy Winther Berg and Lotte Jin Christiansen, for nice discussions and for creating a nice atmosphere. Many

people at COM have made it a good place to be; the people in the opto-electronics group, Christophe Peucheret, Anikó and Beáta Zsigri, Kristján Leósson, Francis Romstad, Leif Oxenløwe, Sune Højfeldt and many more.

I would like to thank my parents for their ongoing support during my studies and to my very soon husband to be, Örvar Arnarson, for being there for me.

Copenhagen, November 2002
Ingibjörg Magnúsdóttir

Contents

List of publications

Refereed journals

1. A. V. Uskov, I. Magnusdottir, B. Tromborg, J. Mørk, and R. Lang, "Line broadening caused by Coulomb carrier-carrier correlations and dynamics of carrier capture and emission in quantum dots", *Appl. Phys. Lett.* **79**, 1679 (2001).

2. T. W. Berg, S. Bischoff, I. Magnusdottir, and J. Mørk, "Ultrafast Gain Recovery and Modulation Limitations in Self-Assembled Quantum Dot Devices", *IEEE Photon. Technol. Lett.* **13**, 541 (2001).

3. I. Magnusdottir, A. V. Uskov, S. Bischoff, B. Tromborg, and J. Mørk, "One- and two-phonon capture processes in quantum dots", *J. Appl. Phys.* **92**, 5982 (2002).

4. I. Magnusdottir, A. V. Uskov, R. Ferreira, G. Bastard, J. Mørk, and B. Tromborg, "Influence of quasi-bound states on the carrier capture in quantum dots", *Appl. Phys. Lett.* **18**, 4318 (2002).

5. I. Magnusdottir, A. V. Uskov, S. Bischoff, and J. Mørk, "Geometry dependence of Auger carrier capture rates into cone-shaped self-assembled quantum dots", *Phys. Rev. B* **67**, 205326 (2003).

Conference contributions

1. I. Magnusdottir, A. Uskov, S. Bischoff, and J. Mørk, "Multiphonon capture processes in self-assembled quantum dots", in *Quantum Electronics and Laser Science Conference*, OSA Technical Digest (Optical Society of America, Washington DC, 2001), pp. 206-207.

2. T. W. Berg, S. Bischoff, I. Magnusdottir, J. Mørk, and P. Borri, "Gain Recovery Dynamics and Limitations in Quantum Dot Amplifiers", in *Conference on Lasers and Electro Optics*, OSA Technical Digest (Optical Society of America, Washington DC, 2001), pp. 358-359.

3. T. W. Berg, S. Bischoff, I. Magnusdottir, and J. Mørk, "Temperature characteristics of quantum dot devices: Rate vs. Master Equation Models", *Technical Digest Integrated Photonics Research*, pp. IMF3 1-3, Monterey, USA (2001).

4. I. Magnusdottir, A. Uskov, S. Bischoff, B. Tromborg, J. Mørk, R. Ferreira, and G. Bastard, "Influence of quasi-bound states on the carrier capture into quantum dots", in *Quantum Electronics and Laser Science Conference*, OSA Technical Digest (Optical Society of America, Washington DC, 2002), pp. 180-181.

5. I. Magnusdottir, A. V. Uskov, S. Bischoff, B. Tromborg, and J. Mørk, "Two-phonon capture processes into quantum dots: The role of intermediate states", *Physica E* **17**, 111 (2003).

6. K. Leosson, D. Birkedal, I. Magnusdottir, J. M. Hvam, and W. Langbein, "Homogeneous linewidth of self-assembled III-V quantum dots observed in single-dot photoluminescence", *Physica E* **17**, 1 (2003).

7. I. Magnusdottir, A. V. Uskov, S. Bischoff, and J. Mørk, "Geometry dependence of Auger carrier capture rates into cone-shaped self-assembled quantum dots", in *Quantum Electronics and Laser Science Conference*, OSA Technical Digest (Optical Society of America, Washington DC, 2003), pp. 148.

Chapter 1

Introduction

Quantum dots are small electron systems, nanometers in size, that can be realized by means of modern fabrication techniques. They are confined in all three spatial directions and they are sometimes referred to as artificial atoms due to the man-made confining potential that gives rise to discrete atomic-like energy levels. The basic physical properties of these confined nanostructures have appealed to many research groups around the world and furthermore, a wide variety of proposals for practical applications have emerged. Practical applications of these systems have been realized, for instance as far-infrared photodetectors [1], lasers [2, 3, 4], and optical amplifiers [5, 6]. Semiconductor lasers and amplifiers based on quantum dots are currently being extensively investigated because of their potential advantages in optical communication. Carriers in such devices are electrically pumped to barriers surrounding the dots where they then relax to the lower lying active states. The characteristic timescale, on which such carrier relaxation takes place, are therefore of special interest. This is the subject that is addressed in this thesis.

The focus of this thesis are the characteristic time constants on which capture into quantum dots takes place and the underlying mechanisms that mediate such capture processes. Chapter 2 reviews some of the basic physical properties of semiconductor quantum dots that form the necessary background in the chapters that follow. In particular, carrier interaction with phonons and other carriers that induces e. g. carrier relaxation will be discussed. In chapter 3 we will investigate phonon-mediated carrier capture into quantum dots by emission of one or two longitudinal optical

(LO) phonons and capture times for these processes will be calculated. In chapter 4, we will investigate phonon-mediated capture processes into dots where a carrier is already present in the state to which the capture takes place. We will then focus on intra-dot relaxation processes in chapter 5 mediated by carrier-LO phonon interaction. We will show that in the case of carriers in discrete and quasi-bound quantum-dot states, they interact strongly with LO phonons. This is a different coupling regime entirely from the coupling of carriers in continuum states to LO phonons, where the coupling is weak, investigated in the previous chapters. In chapter 6 we will investigate carrier capture by carrier-carrier scattering; Auger processes. These will be compared with phonon-mediated processes. The calculations in chapters 4 and 5 were performed in collaboration with Gérald Bastard and Robson Ferreira at the Laboratoire de Physique de la Matière Condensée (LPMC) in Paris.

Chapter 2

Quantum dots

The structure in which carriers are confined to a region of a few nanometers in at least one dimension is called *a nanostructure*. In *quantum wells*, the confinement is one-dimensional, leaving carriers free to move in the two-dimensional plane perpendicular to the confinement direction. Such confinement can for instance be realized by a semiconductor "sandwich" where a thin layer is introduced between layers of higher band gap, e. g. by molecular beam epitaxy. In *quantum wires*, carriers are free to move in one dimension, *quantum dashes* [7, 8] are short quantum wires and in *quantum dots* the structure is zero-dimensional in the sense that carriers are localized in all three dimensions.

In this chapter we will review some of the properties of quantum dots relevant to the work presented in the coming chapters. The material that we present is taken from Refs. [2, 9, 10, 11] unless otherwise mentioned in the text.

2.1 Fabrication methods

In this section we will sketch some of the methods that are used to realize three-dimensional confinement of carriers. A few of them are illustrated in Fig. 2.1. Micro crystals embedded in a glass matrix (a) have been used as color filters through many decades. The confinement is strong but the glass matrix is electrically isolating, which makes their practical realization as optoelectronic devices impossible. Optical gain has been demonstrated in such dots, that could render them feasible as optically pumped lasers or

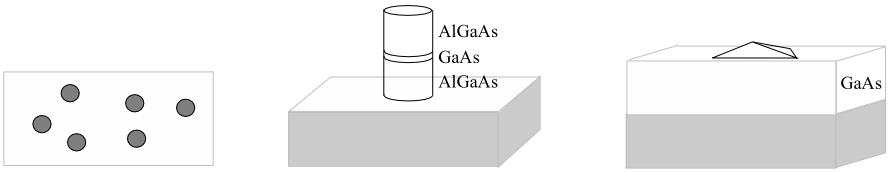

Figure 2.1: Schematic illustration of some of the different methods to make quantum dots; (a) by embedding micro crystals in a glass matrix, (b) lithographical etching and (c) by self-assembly.

amplifiers [12, 13]. By growing alternating layers, e. g. by molecular beam epitaxy, where one layer is a thin quantum well of lower band gap than the surrounding layers, free-standing dots can be realized by etching (b). Arrays of many identical dots can be produced by lithography. Circular, square or elliptic dots can be produced in this manner [14]. Such dots have the main disadvantage that the confinement potential is only a few meV and carriers are thus only confined at low temperatures, where thermal fluctuations ($\sim k_B T$) are not too large.

The quantum dots, that are the focus of the work presented here, are *self-assembled* or self-organized dots, shown in Fig. 2.1 (c). Such islands may be realized by *Stranski-Krastanow* growth [15] in lattice-mismatched systems. Growing e. g. In(Ga)As on a GaAs substrate layer by layer, a thin strained layer is formed due to the lattice mismatch. The strain energy increases with the number of layers. If the strain energy becomes too high, dislocations or defects may be introduced. However, under the right growth conditions (temperature, growth rate, etc.), strain relaxation can occur and islands are formed on a thin *wetting layer* with a few-monolayer thickness. The surface of these islands has lower energy than the environment, and a three-dimensional potential well or *quantum dot* is formed. In(Ga)As/GaAs quantum dots are typically ten or a few tens of nanometers in lateral size (parallel to the wetting layer) and 3-5 nm in height. Recent experiments indicate that InAs/GaAs dots are truncated pyramids [16, 17]. Photoluminescence spectra from such dots show broadening because the dots vary in size, shape and composition. A typical full width at half maximum is 50

meV but lower values have been reported (see [3] and references therein). This is referred to as *inhomogeneous broadening*.

2.2 Electronic properties

In periodic crystals, wave functions can be written in terms of the Bloch functions,

$$\Psi = e^{i\mathbf{k}\cdot\mathbf{r}}u(\mathbf{k},\mathbf{r}), \tag{2.1}$$

where u is a Bloch function with the periodicity of the crystal lattice. The periodic potential that migrating electrons experience gives rise to allowed and forbidden energy bands. In semiconductors at $T = 0$ K a forbidden energy band, the band gap, is between the highest occupied allowed energy band, the valence band, and the lowest unoccupied band, the conduction band. Bloch functions for the conduction band retain much of the symmetry of atomic s orbitals while the valence-band Bloch functions resemble more atomic p_x, p_y and p_z orbitals. We label conduction-band Bloch states by u_s and valence-band states by u_x, u_y and u_z. u_s has even symmetry in all three dimensions. For the valence-band Bloch functions, u_x has odd symmetry along x, etc. Conduction and valence-band Bloch functions are thus orthogonal. Bloch functions of conduction and valence bands however couple through the momentum operator, $\mathbf{p} = -i\hbar\nabla$,[1]

$$\langle u_s|\mathbf{p}|u_i\rangle = \langle u_s|p_i|u_i\rangle \neq 0, \qquad i = x, y, z, \tag{2.2}$$

because, for instance, the operation of p_x on a function of odd symmetry along x gives a function of even symmetry along x. Operating with the kinetic energy operator of the Schrödinger equation on Ψ gives

$$\frac{-\hbar^2}{2m}\nabla^2\Psi = e^{i\mathbf{k}\cdot\mathbf{r}}\left[\frac{-\hbar^2\nabla^2}{2m} + \frac{\mathbf{k}\cdot\mathbf{p}}{m} + \frac{\hbar^2k^2}{2m}\right]u, \tag{2.3}$$

and essentially the $\mathbf{k}\cdot\mathbf{p}$ term gives coupling between conduction and valence bands. The very same term gives many-band $\mathbf{k}\cdot\mathbf{p}$ methods their name. For instance, in the eight-band $\mathbf{k}\cdot\mathbf{p}$ method, all four Bloch states (u_s, u_x, u_y, u_z) couple and the spin degree of freedom gives eight states. By

[1] The operator should not be confused with the p orbitals mentioned earlier. For the rest of this section, $\mathbf{p}$, p_x, p_y and p_z are momentum operators.

assuming that $u(\mathbf{k}, \mathbf{r})$ is a slowly varying function of $\mathbf{k}$, approximated by $u(0, \mathbf{r}) \equiv u(\mathbf{r})$, the wave function can be written as

$$\Psi \approx F(\mathbf{r})u(\mathbf{r}),$$

where F is a slowly varying *envelope* function. It can be shown [18] that for a non-degenerate energy band (the conduction band), F fulfills also a Schrödinger equation of an electron with an *effective mass* moving in a potential that corresponds to the macroscopic variation of the band edge. For instance, in quantum-well structures, the macroscopic potential corresponds to the step-like variation of the band edge.

Significant research effort is devoted to the determination of material parameters of self-assembled quantum dots, including shape and strain fields. The dots have low symmetry and their strong strain fields give rise to internal fields (piezoelectric fields). Furthermore, the material in the dots and in the barrier can intermix. Consequently, modeling of quantum-dot wave functions and energy levels is an ambitious and difficult task. Methods with varying degree of sophistication have been used, from the single-band effective-mass approximation [19, 20, 21], that determines envelope functions, to eight-band $\mathbf{k} \cdot \mathbf{p}$ [22, 23, 24] and empirical pseudo-potential methods [25]. In pseudo-potential methods, the crystal potential, strain and wave functions are described on the atomistic level. The crystal potential is written as a superposition of screened atomic "pseudo potentials", where the atoms are In, Ga, As etc., and wave functions are expanded in a plane-wave basis. The resulting Schrödinger equation is the one for an electron moving in the crystal potential.

Even though eight-band $\mathbf{k} \cdot \mathbf{p}$ and pseudo-potential methods are in general considered more sophisticated than the effective-mass approximation, they cannot be more precise than the input material parameters. Presently, the input parameters, such as strain and precise shape, are not very well known. In the work that is presented in this thesis, we have chosen to "turn a blind eye" to the actual complexity of the band structure by only retaining the most important effect, namely, the discretization of energy levels due to the three-dimensional confinement. We have therefore chosen to use the single-band effective-mass approximation, also for the valence band. Part of the motivation lies also in the fact that the purpose is to calculate relaxation rates that have not been investigated in much detail in the

literature. The wave functions that have been used in the thesis are given in Appendices C and D, namely, the ones of a spherical dot and a cone. A few words about the choice of wave functions are in order: When I started the Ph. D. studies I did not have access to any advanced quantum-dot wave functions. The ultimate goal was to calculate relaxation rates in quantum-dot structures and usually, when such calculations are performed for the first time, approximations need to be made that at the same time retain the basic physical properties of the system. We chose therefore to use wave functions for a sphere because they represented three-dimensional confinement and were available. I had however come accross a paper by Robson Ferreira and Gérald Bastard, Ref. [21], where variational wave functions for a cone had been used. Robson Ferreira was kind to provide me with the program code that calculates the wave functions. I used these functions to calculate phonon-mediated capture rates (chapter 4) and Auger capture rates (chapter 6).

2.3 Carrier-carrier and carrier-phonon scattering

Carrier dynamics in semiconductors are induced by energy and momentum exchange with phonons and other carriers. In bulk and quantum-well structures, scattering rates induced by such interactions are often calculated with a perturbative approach; Fermi's golden rule (see e. g. Refs. [26, 27, 28, 29, 30]). Fermi's golden rule has been extended to also treat carrier capture and relaxation rates in quantum-dot structures [31, 32, 33, 34, 35, 36]. Expressed with Fermi's golden rule [37], scattering rates are given by

$$R = \frac{2\pi}{\hbar} \sum_{f,i} |\langle f|H_{\rm sc}|i\rangle|^2 p_i \delta(E_f - E_i), \tag{2.4}$$

where scattering processes from the initial states $|i\rangle$ into the final states $|f\rangle$ are induced by the Hamiltonian $H_{\rm sc}$. We average over initial states, with probability p_i for state $|i\rangle$, and sum over final states. E_i and E_f are the energies of the initial and final states. The δ function expresses conservation of energy in the process. This perturbative approach is often used without preamble when carrier capture and relaxation rates are calculated. We will identify situations where the perturbative approach is not adequate in chapter 5.

Carrier-carrier scattering

Coulomb interaction of two carriers that leads to relaxation of one carrier and excitation of the other is called an Auger process.

Carrier capture, in which two carriers in the wetting layer interact, leading to capture of one carrier by the quantum dot while the other carrier is excited to a higher energy in the wetting layer, has been shown to give capture times of electrons in the range 1-100 ps for two-dimensional carrier density in the wetting layer of $10^{15} - 10^{16}\mathrm{m}^{-2}$ [38]. Capture mediated by excitation of electrons has been found to be more efficient than scattering by holes. We will investigate such capture processes in chapter 6.

Intradot relaxation by carrier-carrier scattering has been shown to be very fast [21, 34, 39, 40], or on the order of a few hundred femtoseconds to several picoseconds in many cases. Interaction of a quantum-dot carrier with a wetting-layer carrier, leading to the relaxation of the quantum-dot carrier and promoting the wetting-layer carrier to a higher energy, has been investigated in Refs. [34] and [40]. Many-body effects, introduced by a screening of the Coulomb potential have been shown to be important [34]. Intradot Auger relaxation times of two quantum-dot carriers [21, 39], where one carrier relaxes and the other is excited out of the dot, have been found to be on a subpicosecond timescale and up to 100 ps.

Carrier-phonon scattering

Interaction of carriers with ionic vibrations in the crystal - phonons - give rise to energy and momentum exchange between carriers and phonons. Phonon modes are classified according to the direction of the polarization (ionic displacement) with respect to a phonon wavevector, $\mathbf{q}$, as longitudinal or transverse, and further into acoustic and optical phonons. The dispersion of acoustic modes approaches zero at long wavelengths. These low-energy modes are associated with in-phase ionic vibrations. Dispersion of optical modes depend only weakly on phonon wave vectors and it never approaches zero. Optical phonons can be excited by light, hence the name. They are associated with the contrary motion of ions within a unit cell.

A long-wavelength acoustic mode can interact with carriers through deformation potentials, i. e., the differential displacement of unit cells associated with ionic vibrations. Relaxation rates in quantum dots with emission

of LA phonons appear to be rather slow and commonly on the nanosecond time scale [31, 33]. Relaxation is furthermore considerably slowed down when the energy level spacing exceeds a few meV. Thus, in InAs/GaAs self-assembled quantum dots, where the energy level spacing is some tens of meV, efficiency of such relaxation mechanisms should be considerably reduced. In the models in Refs. [31, 33] acoustic phonons are approximated by bulk phonons. However, interface phonons may become more important due to the decrease in size when going from bulk to quantum dots. Furthermore, the interfaces may give rise to new scattering mechanisms. Knipp and Reinecke [35] have studied the influence of acoustic phonons on moving the interfaces of the quantum dot. This "ripple mechanism" could perturb electron wave functions that leads to this scattering mechanism. This mechanism is shown to be non-negligible compared to deformation potential scattering. The overall rates remain however small.

For optical phonons in polar materials, such as III-V semiconductors, the contrary motion of oppositely charged ions in a unit cell gives rise to long-range electric fields. The resulting coupling with carriers is the *Fröhlich interaction*. The Fröhlich coupling is the dominant relaxation mechanism in these materials, although the character of the coupling changes when going from bulk to nanostructures of lower dimensionality and finally to quantum dots. Interaction of carriers in discrete quantum-dot states with LO phonons is so strong that it gives rise to new entities constituted of both carriers and phonons, the polarons (see chapter 5). In this thesis we use a bulk model for the phonon modes, although the phonon spectrum and phonon modes in semiconductor nanostructures can be modified in comparison with bulk semiconductors. In self-assembled dots the material characteristics that define the spatial distribution of phonon modes do not differ significantly in the quantum dot and the barrier material. Furthermore, LO-phonon carrier relaxation rates in quantum wells do not differ significantly, when calculated by either using bulk or confined LO phonons [41, 42]. The Fröhlich Hamiltonian is derived in Appendix A.

The scattering rates that have been discussed in this section can be included in rate-equation models that describe the carrier dynamics in quantum-dot structures in terms of carrier densities or occupation probabilities. Presently, however, such scattering rates have mostly been included phenomenologically. It is of current interest to include the microscopic

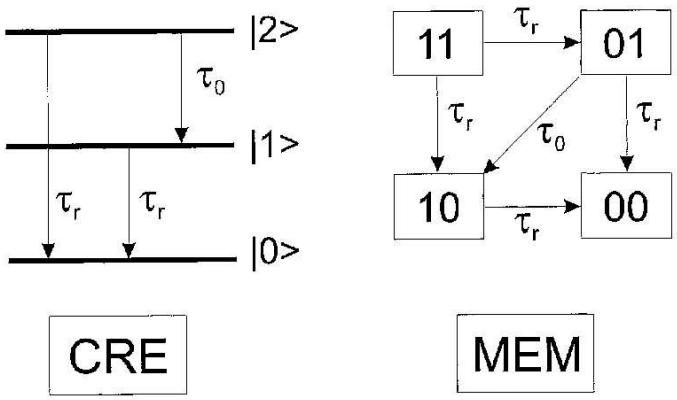

Figure 2.2: Schematic of the rate-equation model (left) and a master-equation model (right) for a two-level system. From Ref. [43].

calculations, such as the ones described here, into the more macroscopic rate-equation models. These rate-equation models will be discussed in the next section.

2.4 Modeling of carrier dynamics in quantum dots - rate equations

In systems of higher dimensionality carrier dynamics are described in terms of rate equations of averaged charge carrier densities. The self-assembled quantum-dot structures that are mostly investigated due to their potential for device applications do not only comprise discrete levels but also the few monolayer thick wetting layer through which the individual dots couple and a barrier surrounding the quantum-dot/wetting-layer system. Rate equation models that describe such structures therefore need *at least*

to couple the wetting layer and the quantum-dot system. Two approaches to modeling of quantum-dot carrier dynamics have been proposed, a direct extension of the rate-equation model used for e. g. quantum-well and bulk structures [44] and a master-equation model for the transitions between micro-states. To illustrate the differences between the rate-equation and the master-equation model, we assume two non-degenerate exciton/carrier levels. A set of rate equations for a such a system, described by the population probabilities ρ_1 and ρ_2 ($0 \leq \rho_i \leq 1$) are of the following form [43, 45];

$$\begin{aligned} \frac{d\rho_2}{dt} &= -\frac{\rho_2}{\tau_r} - \frac{\rho_2(1-\rho_1)}{\tau_0}, \\ \frac{d\rho_1}{dt} &= -\frac{\rho_1}{\tau_r} + \frac{\rho_2(1-\rho_1)}{\tau_0}. \end{aligned} \tag{2.5}$$

The intradot relaxation time is τ_0 and the radiative lifetime, τ_r, is assumed to be the same for both levels. The first term on the right-hand side of both equations accounts for the radiative recombination process. The second terms account for the intradot relaxation process. For simplicity, we have not included any pump terms or terms that account for excitation. The factor $(1-\rho_1)$ is the probability that level $|1\rangle$ is empty. The inclusion of this factor in the rate equations thus ensures that the Pauli principle is fulfilled and dot levels are not overfilled.

A corresponding master-equation model describes transitions between micro-states. Instead of describing the dynamics of each *energy level* in the rate-equation model a single micro-state describes the number of carriers in each energy level. In this particular example the micro-states of the system are filled with (n_1, n_2) carriers; $(0,0)$, $(1,0)$, $(0,1)$ and $(1,1)$. The probability to find a dot in a given micro-state is given by w_{n_1,n_2}. The corresponding master equations are then given by

$$\begin{aligned} \frac{dw_{00}}{dt} &= \frac{w_{10}}{\tau_r} + \frac{w_{01}}{\tau_r} \\ \frac{dw_{10}}{dt} &= -\frac{w_{10}}{\tau_r} + \frac{w_{11}}{\tau_r} + \frac{w_{01}}{\tau_0} \\ \frac{dw_{01}}{dt} &= -\frac{w_{01}}{\tau_r} + \frac{w_{11}}{\tau_r} - \frac{w_{01}}{\tau_0} \\ \frac{dw_{11}}{dt} &= -2\frac{w_{11}}{\tau_r}. \end{aligned} \tag{2.6}$$

Note here that the Pauli principle is fulfilled implicitly here due to the definition of the micro-states. Fig. 2.2 illustrates the differences between the rate-equation model and the master-equation model. A comparison of Eqs. (2.5) and (2.6) shows that the number of equations increases when using a master-equation model. When more energy levels/states are included the master-equation model grows very fast and becomes computationally heavy.

It has been shown that at low temperatures there are differences that occur between the master-equation model and the rate-equation model. For instance, it was shown in Ref. [46] that if inhomogeneous broadening is not taken into account, only the master-equation model can explain a dip in the transparency current at low temperature. In Ref. [43] the master-equation model is shown to model adequately low-temperature photoluminescence transients while the rate-equation model fails to do so. At room temperature the rate-equation and the master-equation model give similar results [44]. The difference between the two models lies in the fact that an uneven carrier distribution among the dots can be correctly modeled in the master-equation model whereas in the rate-equation model carriers are always distributed evenly. At low temperatures the escape time for carriers out of the dots is very long compared to the spontaneous emission time. Within this time carriers are therefore not redistributed among the dots and some dots are empty while others are filled. The master-equation model can model this behavior adequately while in the rate-equation model, carriers in each level are described by a single carrier density. This inherently assumes that carriers are distributed evenly among the levels. The rate-equation model is therefore only a good approximation when the redistribution time is small compared to any other characteristic time that tends to pull the system away from equilibrium [46]. The rate-equation model thus provides adequate modeling at room temperature.

A few words about carrier-capture times

In Eq. (2.5), terms that describe carrier capture from the wetting layer into the dot levels (pump terms) were not included for simplicity. To describe carrier capture into the upper quantum-dot level in the rate-equation model, one can write

$$\frac{d\rho_2}{dt} = -\frac{\rho_2}{\tau_r} - \frac{\rho_2(1-\rho_1)}{\tau_0} + R(1-\rho_2) + ... \tag{2.7}$$

We have ignored terms that account for carrier escape and intra-dot excitation. For $\rho_2 << 1$, R is the *number of carriers entering the level per unit time*. This is the carrier capture rate that can be calculated for instance with Fermi's golden rule. It can be measured, for instance in photoluminescence experiments as the *photoluminescence rise-time* $\tau = 1/R$ of level $|2\rangle$. If the level is degenerate with degeneracy g and each state is described with $|2, i\rangle$, the total capture rate into the level is the sum

$$R_{|2\rangle} = \sum_{i=1}^{g} R_i, \tag{2.8}$$

where R_i is the capture rate into state $|2, i\rangle$. The photoluminescence rise time is then given by $\tau_{|2\rangle} = 1/R_{|2\rangle}$. Eq. (2.7) can also be written in terms of the quantum-dot carrier density, $n_{\mathrm{QD}} = \rho N_D$, where N_D is the number of dots in a macroscopic volume, that comprises many dots, and we have neglected spin degeneracy for simplicity. We have also assumed here that all the dots are identical.

We will show in chapters 3 and 6 that at low to moderate wetting-layer carrier densities, n_{W}, we can write

$$R = (A + Cn_{\mathrm{W}})n_{\mathrm{W}}, \tag{2.9}$$

where the first term describes phonon-assisted capture and the second term describes Auger carrier capture. This dependence can be understood by the fact that in phonon-assisted capture, one carrier is involved and the capture is therefore *linear* in n_{W}. In Auger carrier capture, two carriers interact in the wetting layer, leading to the capture of one carrier and excitation of the other, and the capture rate is therefore *quadratic* in n_{W}. The capture term in Eq. (2.7) can then be written in the rate equation for the wetting-layer carrier density as

$$\frac{\partial n_{\mathrm{W}}}{\partial t} = \ldots - RN_D(1 - \rho_2) \tag{2.10}$$

$$= \ldots - (A + Cn_{\mathrm{W}})n_{\mathrm{W}}N_D(1 - \rho_2) \tag{2.11}$$

$$= \ldots - \frac{n_{\mathrm{W}}}{\tau_c}(1 - \rho_2), \tag{2.12}$$

with *the effective capture time* τ_c [38]. The effective capture time,

$$\frac{1}{\tau_c} = (A + Cn_{\mathrm{W}})N_D, \tag{2.13}$$

is the property of the *quantum-dot ensemble* whereas R is the property of a *single quantum dot*. Throughout this thesis we calculate the capture rate R unless otherwise mentioned.

Chapter 3

Phonon-mediated carrier capture into quantum dots

In polar materials, such as III-V semiconductors, the carrier-LO phonon interaction leads to very efficient relaxation mechanisms in systems of higher dimensionality. Carrier capture into quantum dots by emission of one LO phonon has been shown to be efficient, or on the order of a few ps to 100 ps [21]. Such a process is depicted schematically in Fig. 3.1. The single-phonon capture rate that is calculated in Ref. [21] is efficient for only a very small range of dot sizes. This arises due to an energy conservation requirement, i. e., the impinging carrier "loses" energy that amounts to the LO phonon energy. This, and the fact that dot state energies decrease fast with increasing dot size for the strongly confined self-assembled quantum dots, leads to a rather small range of dot sizes for which capture may take place. A way to overcome such restrictions is carrier capture by emission of more than one phonon. Capture by multiple LO-phonon emission was proposed in Ref. [47], where non-degenerate pump-probe measurements (pump and probe are of different wavelenghts) were performed on self-assembled InAs/GaAs quantum dots. By pumping in the wetting layer and GaAs while probing the ground state transition, photoluminescence rise times on the order of 10 ps were measured. De Giorgi *et al.* [48] measured also photoluminescence rise times of a few ps, and suggested that carrier-phonon scattering mechanisms are the dominant capture mechanisms at room temperature.

This chapter presents calculations of phonon-mediated carrier capture

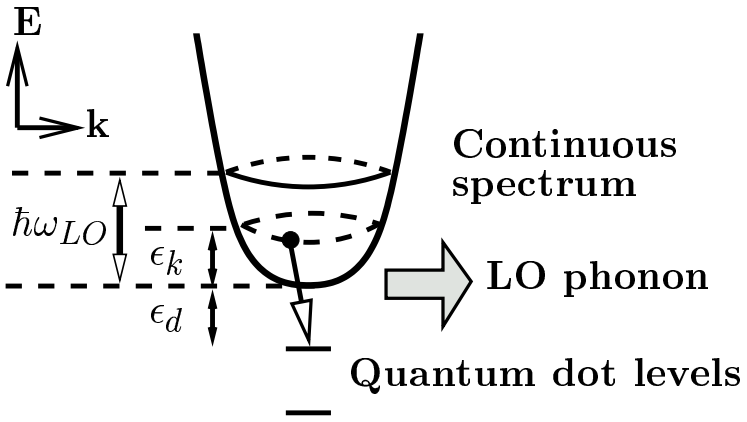

Figure 3.1: Single-phonon capture process into a quantum dot where the onset of the continuum is at the quantum dot barrier. Due to an energy conservation requirement, the discrete levels cannot be separated more than $\hbar\omega_{\mathrm{LO}}$ from the onset of the continuous energy spectrum and the energy of the incident carrier, ϵ_k, is less than $\hbar\omega_{\mathrm{LO}}$.

rates into quantum dots. This includes capture by emission of a single LO phonon and by emission of two LO phonons. Calculations of the two-phonon-mediated process presented here (and in Ref. [49]) are, to our knowledge, the first ones to be published on the matter.

We model the quantum dot by a spherical dot with a finite confinement potential in the effective-mass approximation. Due to the spherical symmetry, quantum-dot states can be characterized by an angular momentum quantum number, ℓ, an azimuthal quantum number, m, and spin, s. The wave functions and energy levels are discussed in Appendix C. Figure 3.2 shows energy levels of an electron in a spherical dot as a function of quantum-dot radius, a. Actually, the *binding energies* are shown, i. e. the distance of the levels from the quantum-dot barrier. The energy levels can be characterized by (ℓ, n), where n denotes the n-th energy level ℓ to become bound to the dot. n is illustrated for $\ell = 0$ in Fig. 3.2. For each ℓ, the azimuthal quantum number, m, fulfills $-\ell \leq m \leq \ell$. Counting spin degeneracy, each energy level is therefore $2(2\ell + 1)$ times degenerate. For dot radius below about 2.8 nm, no states are bound in the dot. The first level, $(0, 1)$, becomes bound at $a \approx 2.8$ nm. The second level to become bound is $(1, 1)$, then $(2, 1)$, $(0, 2)$ and so forth.

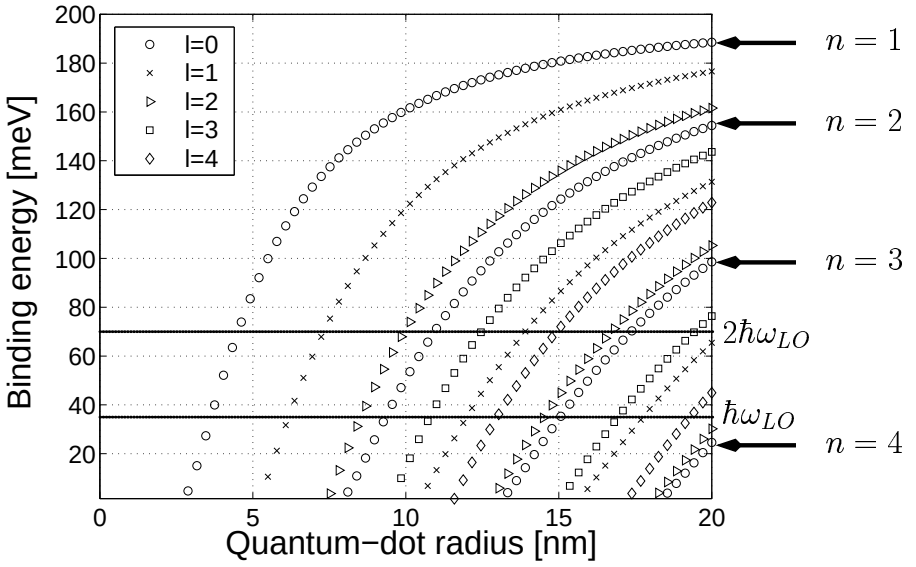

Figure 3.2: Binding energies of levels with $\ell \in [0, 4]$ for an electron with $m^* = 0.07m_0$ in a spherically symmetric quantum dot with confinement potential $V_0 = 200$ meV.

In the following we will present calculations of the *total capture rate* into the energy level (ℓ, n),

$$R_{\ell,n} = 2 \sum_{m=-\ell}^{\ell} R^s_{\ell,n,m}, \tag{3.1}$$

where $R^s_{\ell,n,m}$ is the capture rate into the state (ℓ, n, m, s). The spin state of a particle does not change in the capture process because the carrier-LO phonon interaction is a Coulomb interaction and does not involve any spin operators. This gives the factor of 2 in Eq. (3.1). The photoluminescence rise time of the energy level (ℓ, n) is then given by

$$\tau_{\ell,n} = \frac{1}{R_{\ell,n}}. \tag{3.2}$$

We would like to stress here that the expression (3.1) cannot be inserted in a rate equation of the form in Eq. (2.10). If $\rho^s_{\ell,n,m}$ is the occupation

probability of a state (ℓ, n, m, s), the term that describes the capture process in the rate equation for $\rho^s_{\ell,n,m}$ can be written as

$$\frac{\partial \rho^s_{\ell,n,m}}{\partial t} = R^s_{\ell,n,m}(1 - \rho^s_{\ell,n,m}) + \dots \tag{3.3}$$

In the rate equation for the wetting-layer carrier density, n_{W}, the corresponding term is given by

$$\frac{\partial n_{\mathrm{W}}}{\partial t} = -2N_D \sum_{\ell,n,m} R_{\ell,n,m}(1 - \rho_{\ell,n,m}) + \dots, \tag{3.4}$$

where we have set $R_{\ell,n,m} = R^s_{\ell,n,m}$ with $s = \pm 1/2$. In the following sections we will calculate the photoluminescence rise time for single- and two-phonon-mediated capture processes and we will call it a capture time.

The rate of carrier capture into a quantum-dot state can be expressed as

$$R = \sum_{\mathbf{k}} w(\mathbf{k}) f(\epsilon_k), \tag{3.5}$$

where $\mathbf{k}$ is the carrier wavevector characterizing the carrier in the continuous spectrum and $w(\mathbf{k})$ is the probability per unit time that the transition will take place. We model the wave function of the continuum carrier by a plane wave,

$$\Psi_k(\mathbf{r}) = \frac{1}{\sqrt{\Omega}} e^{i\mathbf{k}\cdot\mathbf{r}}, \tag{3.6}$$

where Ω is the normalization volume. We assume that the continuum is thermalized and can therefore be described by a Fermi distribution,

$$f(\epsilon_k) = \left(\exp\left(\frac{\epsilon_k - \mu}{k_B T} \right) + 1 \right)^{-1}, \tag{3.7}$$

where ϵ_k is the energy of the incident carrier and μ is the chemical potential. The chemical potential is calculated with the Padé approximation, see e. g. Ref. [50].

3.1 Single-phonon capture

A single-phonon mediated capture process (with emission of one LO phonon) is illustrated schematically in Fig. 3.1. The probability that a carrier in state $|\mathbf{k}\rangle$ is captured into a quantum-dot state, $|d\rangle$, by emitting a phonon of wavevector $\mathbf{q}$ is expressed with Fermi's golden rule

$$w(\mathbf{k},\mathbf{q}) = \frac{2\pi}{\hbar} \sum_{\{n\},\{m\}} \left| \left\langle \{m\}, d \left| \hat{V}^{\mathrm{em}}(\mathbf{q}) \right| \mathbf{k}, \{n\} \right\rangle \right|^2 \prod_i P(n_i) \delta(E_f - E_i), \tag{3.8}$$

where $\mathbf{q}$ is a phonon wavevector and $E_i(E_f)$ is the energy of the initial (final) state. We average over initial phonon states, $|\{n\}\rangle$, and sum over final phonon states, $|\{m\}\rangle$. The initial and final phonon states are denoted as

$$|\{n\}\rangle = |n_1, n_2, \dots, n_i, \dots\rangle,$$
$$|\{m\}\rangle = |m_1, m_2, \dots, m_i, \dots\rangle.$$

A phonon state $|\{n\}\rangle$ has n_i phonons with momentum $\mathbf{q}_i$ $(i = 1, 2, \dots)$ and $P(n_i)$ is the probability of finding n_i phonons with momentum $\mathbf{q}_i$. Hence, the probability of finding n_i phonons with momentum $\mathbf{q}_i$ $(i = 1, 2, \dots)$ is $\prod_i P(n_i)$. $\hat{V}^{\mathrm{em}}_{\mathbf{q}_i}$ is the Fröhlich Hamiltonian for emission of a phonon with wavevector $\mathbf{q}_i$ [see Eq. (A.20)],

$$\hat{V}^{\mathrm{em}}_{\mathbf{q}_i} = \alpha(q_i) e^{-i\mathbf{q}_i\cdot\mathbf{r}} \hat{a}^\dagger_{\mathbf{q}_i}. \tag{3.9}$$

The matrix element $\left\langle \{m\}, d \left| \hat{V}^{\mathrm{em}}(\mathbf{q}_i) \right| \mathbf{k}, \{n\} \right\rangle$ is given by

$$\left\langle \{m\}, d \left| \hat{V}^{\mathrm{em}}(\mathbf{q}_i) \right| \mathbf{k}, \{n\} \right\rangle = \alpha(q_i) \left\langle d \left| e^{-i\mathbf{q}_i\cdot\mathbf{r}} \right| \mathbf{k} \right\rangle \sqrt{n_i + 1} \delta_{n_i+1,m_i} \prod_{j\neq i} \delta_{m_j,n_j}, \tag{3.10}$$

i. e. the matrix element is non-zero only if the number of phonons with wavevector $\mathbf{q}_i$ increases by 1 (phonon emission) *and* the number of phonons with wavevector $\mathbf{q}_j$ $(j \neq i)$ is unchanged. We thus obtain

$$w(\mathbf{k},\mathbf{q}) = \frac{2\pi}{\hbar} \sum_{n_i} |\alpha(q)|^2 \left| \left\langle d \left| e^{-i\mathbf{q}\cdot\mathbf{r}} \right| \mathbf{k} \right\rangle \right|^2 (n_i + 1) P(n_i) \delta(\epsilon_k - \hbar\omega_{\mathbf{q}} + \epsilon_d) \tag{3.11}$$

$$= \frac{2\pi}{\hbar} (\overline{n} + 1) |\alpha(q)|^2 \left| \left\langle d \left| e^{-i\mathbf{q}\cdot\mathbf{r}} \right| \mathbf{k} \right\rangle \right|^2 \delta(\epsilon_k - \hbar\omega_{\mathrm{LO}} + \epsilon_d), \tag{3.12}$$

where Eq. (3.12) is obtained by an average over n_i that yields the factor $(\overline{n}+1)$. The average phonon population is given by the Bose-Einstein factor,

$$\overline{n} = \left(\exp\left(\frac{\hbar\omega_{\mathrm{LO}}}{k_B T}\right) - 1\right)^{-1}. \tag{3.13}$$

We have assumed in the last expression that LO phonons are dispersionless and we have therefore replaced $\omega_{\mathbf{q}}$ by ω_{LO}. The energy conservation in Eq. (3.12) is expressed according to the capture process in Figure 3.1, where ϵ_d is the quantum-dot binding energy. The total transition probability is obtained by a sum over emitted phonon modes,

$$w(\mathbf{k}) = \sum_{\mathbf{q}} w(\mathbf{k},\mathbf{q}). \tag{3.14}$$

By Eq. (3.5), the capture rate is then given by

$$\begin{aligned} R &= \sum_{\mathbf{k}}\sum_{\mathbf{q}} w(\mathbf{k},\mathbf{q}) f(\epsilon_k) \\ &= \frac{2\pi}{\hbar}(\overline{n}+1)\sum_{\mathbf{k}}\sum_{\mathbf{q}} |\alpha(q)|^2 \left|\left\langle d\left|e^{-i\mathbf{q}\cdot\mathbf{r}}\right|\mathbf{k}\right\rangle\right|^2 f(\epsilon_k)\delta(\epsilon_k - \hbar\omega_{\mathrm{LO}} + \epsilon_d). \end{aligned} \tag{3.15}$$

The capture rate can furthermore be written in terms of the three-dimensional density of states, $g_{3\mathrm{D}}$,

$$R = \frac{2\pi}{\hbar}(\overline{n}+1)|\alpha_0|^2 g_{3\mathrm{D}}(\epsilon_{k0}^{1\mathrm{p}}) f(\epsilon_{k0}^{1\mathrm{p}}) \frac{\Omega}{8\pi} \sum_{\mathbf{q},\mathbf{k}_0} \frac{|\langle d|e^{-i\mathbf{q}\cdot\mathbf{r}}|\mathbf{k}_0\rangle|^2}{q^2}, \tag{3.16}$$

where $\epsilon_{k0}^{1\mathrm{p}} = \hbar\omega_{\mathrm{LO}} - \epsilon_d$ is the energy of the incident carrier, determined by the energy conservation expressed by the δ function in Eq. (3.15). $\mathbf{k}_0$ fulfills $\epsilon_{k0}^{1\mathrm{p}} = \hbar^2 k_0^2/(2m^*)$ and the summation over $\mathbf{k}_0$ denotes an integration over the directions of the vector $\mathbf{k}_0$. To obtain Eq. (3.16) we have integrated over $|\mathbf{k}_0|$ with help of the δ function. The coupling constant α_0 is defined in Eq. (A.19). The density of states is given by

$$g_{3\mathrm{D}}(\epsilon) = \begin{cases} \frac{m^*}{\pi^2\hbar^2}\sqrt{\frac{2m^*\epsilon}{\hbar^2}}, & \epsilon \geq 0, \\ 0, & \epsilon < 0. \end{cases} \tag{3.17}$$

A factor $1/(4\pi)$ in Eq. (3.16) comes about because we have not yet integrated over the directions of $\mathbf{k}_0$ and in the derivation of the density of states

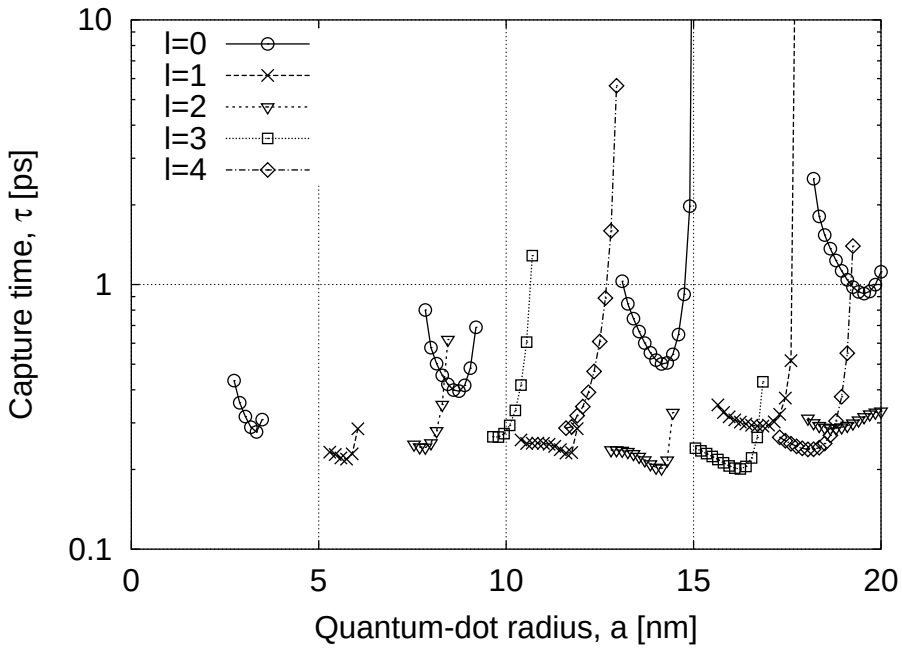

Figure 3.3: Single-phonon capture time of an electron as a function of quantum-dot radius. Carrier density is set to be $n_{3D} = 10^{17}$ cm^{-3} and the same dot parameters as in Figure 3.2 are used.

this integration is performed (due to the parabolic energy dependence of free carriers). We have also divided by a factor of 2 because the density of states includes spin degeneracy but the capture rate, R, involves carriers of *given* spin.

Dot-size dependence

The single-phonon capture time into the energy levels (ℓ, n), i. e. $\tau_{\ell,n}$, is shown in Fig. 3.3 as a function of quantum-dot radius. In the following we use the same dot parameters as in Figure 3.2 unless otherwise mentioned. The capture time was defined in Eqs. (3.1) and (3.2). The number n is not labeled explicitly. Due to the energy conservation requirement, capture to states of all ℓ within $\hbar\omega_{\mathrm{LO}}$ from the quantum-dot barrier is possible, results for $\ell \in [0, 4]$ are shown in Fig. 3.3. It is seen that there are intervals or

bands of dot radii where phonon-mediated capture is allowed, consistent with other results [21]. The bands are seen to nearly cover the dot size range apart from two narrow gaps on the lower radius side. The lower end of a radius band, $a = a_{\min}$, is defined by the appearance of a new level in the quantum dot to which capture may take place, see also Figure 3.2. The increase in τ at this end essentially follows the decrease in matrix elements, $|\langle d|e^{-i\mathbf{q}\cdot\mathbf{r}}|\mathbf{k}\rangle|^2$, as $a \to a_{\min}^+$. In this limit, the "volume" of the quantum-dot wave function tends to infinity due to the weaker binding to the dot and the value of matrix elements decreases. The rate approaches zero at the higher end of each radius band (τ approaches infinity) beyond which the binding energy of the level is larger than the phonon energy. The abrupt increase in τ at this end can be explained in terms of the decrease of $g_{3\mathrm{D}}$ of the incident carrier as $\epsilon_{k0}^{1\mathrm{p}} \to 0^+$ [see Eqs. (3.16) and (3.17)]. The capture times are typically on the order of 0.2–0.3 ps at the radius band minima.

We have also considered the dependence of the capture times on confinement energy. We decreased the confinement energy by a factor of 2; $V_0 = 100$ meV, and calculated the capture times for the first $\ell = 0$ band. The capture time minimum is found to be similar to the case of $V_0 = 200$ meV but the radius band is broader, 2.5 nm wide, while it is less than 1 nm wide for $V_0 = 200$ meV. This is because the slope of the binding energy is steeper for the larger confinement energy, so the radius bands decrease with increasing confinement energy. In fact, the confinement energy of self-assembled quantum dots, is not only determined by the band offset between the quantum-dot and barrier material due to the complex structure of the combined system and the large impact of strain. The value of $V_0 = 200$ meV that we have used here is from Ref. [51] in which the electronic structure of InAs/GaAs pyramidal quantum dots is calculated.

Temperature dependence

The temperature dependence of the capture rate occurs through the Fermi factor of the incident carrier and the phonon factor, $(\overline{n}+1)$, as

$$R_T \propto f(\epsilon_{k0}^{1\mathrm{p}})(\overline{n}+1). \tag{3.18}$$

In the left panel of Figure 3.4 we have plotted the Fermi factor for various energies of the incident carrier. Due to the energy conservation requirement we have that this energy fulfills $\epsilon_{k0}^{1\mathrm{p}} = \hbar\omega_{\mathrm{LO}} - \epsilon_d$ and decreases therefore

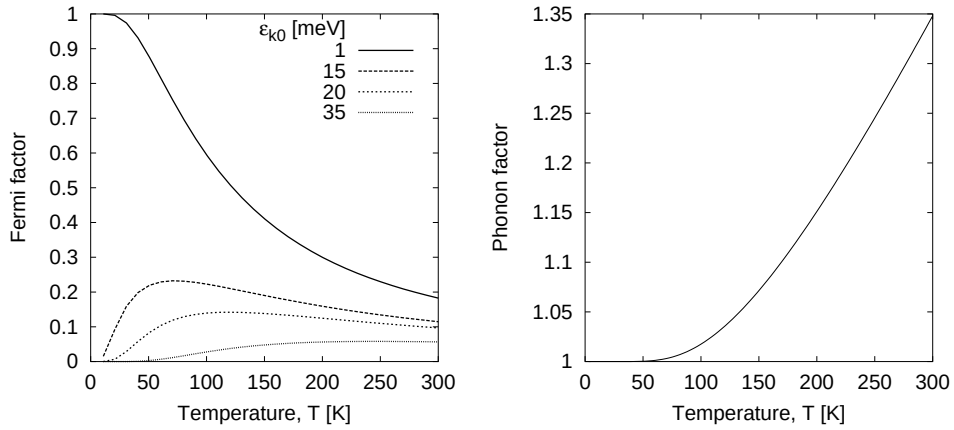

Figure 3.4: Temperature dependence of the Fermi factor, $f(\epsilon_{k0}^{1\mathrm{p}})$, is shown in the left panel for various $\epsilon_{k0}^{1\mathrm{p}}$ ranging from 1 to 35 meV. The phonon factor, $(\overline{n}+1)$, is shown in the right panel.

from $\hbar\omega_{\mathrm{LO}}$ to 0 because ϵ_d increases from 0 to $\hbar\omega_{\mathrm{LO}}$ within one radius band (with increasing radius). At $\epsilon_{k0}^{1\mathrm{p}} = 0$ the dot level becomes too deep for single-phonon capture. The right panel of Figure 3.4 shows the variation of the phonon factor with temperature. We see that it increases only about 35% as the temperature increases from 0 to 300 K. On the other hand the Fermi factor varies considerably with temperature *and* with the energy of the incident carrier. For instance we see that it decreases from 1 to 0.2 for $\epsilon_{k0}^{1\mathrm{p}} = 1$ meV. We show in Figure 3.5 the capture time into the second $\ell = 0$ band as a function of temperature for a given dot radius. At this radius ($a = 8.7$ nm), $\epsilon_{k0}^{1\mathrm{p}} = 15.1$ meV. A comparison of the capture time dependence with the reciprocal of the corresponding Fermi factor (Fig. 3.4) shows that the capture time dependence essentially follows the variations in the Fermi factor.

3.2 Two-phonon capture

Two-phonon-mediated capture processes can take place to states with binding energies ϵ_d that fulfill $0 < \epsilon_d \leq 2\hbar\omega_{\mathrm{LO}}$, whereas single-phonon capture can only take place to states with $0 < \epsilon_d \leq \hbar\omega_{\mathrm{LO}}$. The Hamiltonian for

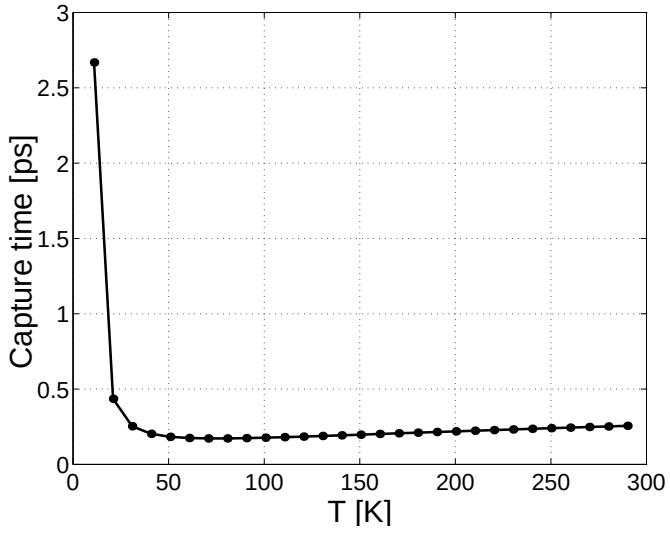

Figure 3.5: Temperature dependence of the single-phonon capture time for capture into $(0,2)$. $a = 8.7$ nm ($\epsilon_{k0}^{1\mathrm{p}} = 15.1$ meV) and $n_{3\mathrm{D}} = 10^{17}$ cm^{-3}.

emission of two phonons is given by

$$\hat{V}^{\mathrm{em}}(\mathbf{q}_1, \mathbf{q}_2) = \alpha(q_1) e^{-i\mathbf{q}_1\cdot\mathbf{r}} \hat{a}^\dagger_{\mathbf{q}_1} + \alpha(q_2) e^{-i\mathbf{q}_2\cdot\mathbf{r}} \hat{a}^\dagger_{\mathbf{q}_2}, \tag{3.19}$$

where $\mathbf{q}_1$ and $\mathbf{q}_2$ are the phonon wavevectors. For two-phonon capture, the transition probability is zero to first order because the Fröhlich Hamiltonian is linear in the creation operators and the phonon populations in the initial and final states differ by two. The transition probability, calculated with Fermi's golden rule within second-order perturbation theory [Eq. (B.25)], is given by

$$w(\mathbf{k}, \mathbf{q}_1, \mathbf{q}_2) = \frac{2\pi}{\hbar} \sum_{\{n\},\{m\}} \Big| \sum_{\nu} \frac{\hat{V}^{\mathrm{em}}_{\mathrm{f}\nu} \hat{V}^{\mathrm{em}}_{\nu\mathrm{i}}}{E_i - E_\nu} \Big|^2 \prod_i P(n_i) \delta(E_f - E_i), \tag{3.20}$$

where the phonon states $|\{n\}\rangle$ and $\{m\}\rangle$ are defined as in single-phonon capture and we average over the initial phonon states. The states $|\nu\rangle$ for which the matrix elements of $\hat{V}^{\mathrm{em}}$ are non-zero are referred to as *intermediate states*. E_i, E_ν and E_f are the energies of the initial, intermediate

and final state. This transition probability is calculated in Appendix B.2, where it is found to be

$$w(\mathbf{k},\mathbf{q}_1,\mathbf{q}_2) = \frac{2\pi}{\hbar}(\overline{n}+1)^2 \times \left|\alpha(q_1)\alpha(q_2)\sum_{\nu}\frac{M_{f\nu}^{q_2}M_{\nu i}^{q_1}+M_{f\nu}^{q_1}M_{\nu i}^{q_2}}{\epsilon_k-\epsilon_\nu-\hbar\omega_{\mathrm{LO}}}\right|^2 \delta(\epsilon_k-2\hbar\omega_{\mathrm{LO}}+\epsilon_d). \tag{3.21}$$

The matrix elements are given by

$$M_{f\nu}^{q} = \langle d|e^{-i\mathbf{q}\cdot\mathbf{r}}|\zeta_\nu\rangle, \tag{3.22}$$

$$M_{\nu i}^{q} = \langle \zeta_\nu|e^{-i\mathbf{q}\cdot\mathbf{r}}|\mathbf{k}\rangle, \tag{3.23}$$

where $|\zeta_\nu\rangle$ denotes an intermediate carrier state and ϵ_ν is its energy. The summation is over intermediate carrier states, that either belong to the continuous energy spectrum or the discrete quantum-dot spectrum. Figure 3.6 shows the two-phonon capture process, where capture via the different intermediate states is illustrated schematically. Intermediate states are depicted with dashed lines since carriers are not actually transferred to an intermediate state.

Equation (3.21) is only valid in the case where the denominator $\epsilon_k - \epsilon_\nu - \hbar\omega_{\mathrm{LO}}$ is not too close to zero. The condition $\epsilon_k - \epsilon_\nu = \hbar\omega_{\mathrm{LO}}$ corresponds in fact to a cascaded emission of LO phonons because the energy difference between the initial and the final state is necessarily $2\hbar\omega_{\mathrm{LO}}$ (energy conservation). Such a cascaded emission *cannot* be treated with our perturbative approach. We will therefore restrict ourselves here to calculate only two-phonon capture rates where the perturbative approach is valid. For energy of the incident carrier in the interval $0 \leq \epsilon_k < \hbar\omega_{\mathrm{LO}}$ there is no possibility for a cascaded emission process via an intermediate carrier state in the *continuous* energy spectrum. Due to energy conservation we have that $\epsilon_k = 2\hbar\omega_{\mathrm{LO}} - \epsilon_d$. Therefore, by choosing $0 \leq \epsilon_k < \hbar\omega_{\mathrm{LO}}$ we only calculate capture into states with $\hbar\omega_{\mathrm{LO}} < \epsilon_d \leq 2\hbar\omega_{\mathrm{LO}}$, i. e. the states that lie too deep to be attained in a single-phonon process. For these final states a cascaded process can nevertheless occur via intermediate *discrete* carrier states, if such a state is situated $\hbar\omega_{\mathrm{LO}}$ above the final carrier state. Such a situation takes place for specific values of confinement potential, dot size

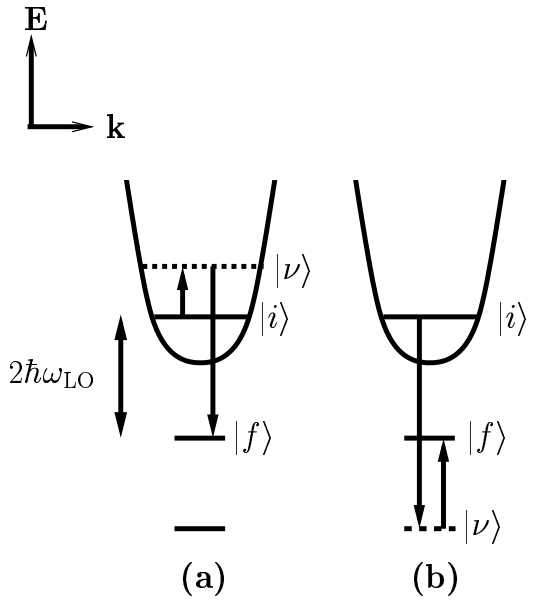

Figure 3.6: Energy diagram in **k**-space of the two-phonon capture process via different intermediate states. (a) A contribution to the capture from an intermediate continuous state. (b) A contribution to the capture from an intermediate discrete state. The dashed lines indicate that carriers are not actually transferred to an intermediate state. The initial and final states can also serve as intermediate states.

and particle mass and can therefore only be avoided by not calculating capture into these states. As we shall see later, this situation occurs for certain states for our choice of parameters and capture rates into these states will not be calculated.

The total transition probability is obtained by a summation over all the emitted phonon modes,

$$w(\mathbf{k}) = \sum_{\mathbf{q}_1,\mathbf{q}_2} w(\mathbf{k},\mathbf{q}_1,\mathbf{q}_2). \tag{3.24}$$

From Eqs. (3.21) and (3.24) we get

$$w(\mathbf{k}) = \frac{2\pi}{\hbar}(\overline{n}+1)^2 \times \sum_{\mathbf{q}_1,\mathbf{q}_2} \left| \alpha(q_1)\alpha(q_2) \sum_{\nu} \frac{M_{f\nu}^{q_2} M_{\nu i}^{q_1} + M_{f\nu}^{q_1} M_{\nu i}^{q_2}}{\epsilon_k - \epsilon_\nu - \hbar\omega_{\mathrm{LO}}} \right|^2 \delta(\epsilon_k - 2\hbar\omega_{\mathrm{LO}} + \epsilon_d). \tag{3.25}$$

Using Eq. (3.5) the capture rate is thus given by

$$R = \frac{2\pi}{\hbar}(\overline{n}+1)^2 |\alpha_0|^4 \times \sum_{\mathbf{k}} f(\epsilon_k)\delta(\epsilon_k - \epsilon_{k0}^{2\mathrm{p}}) \sum_{\mathbf{q}_1,\mathbf{q}_2} \frac{1}{q_1^2 q_2^2} \Big| \sum_{\nu} \frac{M_{f\nu}^{q_2} M_{\nu i}^{q_1} + M_{f\nu}^{q_1} M_{\nu i}^{q_2}}{\epsilon_k - \epsilon_\nu - \hbar\omega_{\mathrm{LO}}} \Big|^2, \tag{3.26}$$

where $\epsilon_{k0}^{2\mathrm{p}} = 2\hbar\omega_{\mathrm{LO}} - \epsilon_d$ is the energy of the incident carrier and we have inserted $|\alpha(q)|^2$ from Eqs. (A.18) and (A.19).
The capture rate can furthermore be written in terms of the density of states, $g_{3\mathrm{D}}$, that was defined in Eq. (3.17),

$$R = \frac{2\pi}{\hbar}(\overline{n}+1)^2 |\alpha_0|^4 f(\epsilon_{k0}^{2\mathrm{p}}) g_{3\mathrm{D}}(\epsilon_{k0}^{2\mathrm{p}}) \frac{\Omega}{8\pi} \times \sum_{\mathbf{q}_1,\mathbf{q}_2,\mathbf{k}_0} \frac{1}{q_1^2 q_2^2} \Big| \sum_{\nu} \frac{M_{f\nu}^{q_2} M_{\nu i}^{q_1} + M_{f\nu}^{q_1} M_{\nu i}^{q_2}}{\epsilon_{k_0}^{2\mathrm{p}} - \epsilon_\nu - \hbar\omega_{\mathrm{LO}}} \Big|^2. \tag{3.27}$$

For capture via intermediate *continuum* states, we have the selection rule

$$M_{\nu i}^{q} = \delta_{\mathbf{k}_0,\mathbf{k}_\nu+\mathbf{q}}, \tag{3.28}$$

because the incident carrier wave function is described by a plane wave. This implies crystal momentum conservation in the continuum. With this selection rule, the matrix elements in the sum involving continuum intermediate states are given by

$$M_{f\nu}^{q_2} M_{\nu i}^{q_1} = F(\mathbf{k}_0 - \mathbf{q}_1 - \mathbf{q}_2), \tag{3.29}$$

$$M_{f\nu}^{q_1} M_{\nu i}^{q_2} = M_{f\nu}^{q_2} M_{\nu i}^{q_1}, \tag{3.30}$$

where

$$F(\mathbf{k}_0 - \mathbf{q}_1 - \mathbf{q}_2) \equiv \frac{1}{\sqrt{\Omega}} \int d^3r \Psi_d^*(\mathbf{r}) e^{i(\mathbf{k}_0 - \mathbf{q}_1 - \mathbf{q}_2)\cdot\mathbf{r}}. \tag{3.31}$$

With this definition of F the capture rate becomes

$$R = \frac{2\pi}{\hbar}(\overline{n}+1)^2 \left|\alpha_0\right|^4 f(\epsilon_{k0}^{2\mathrm{p}}) g_{3\mathrm{D}}(\epsilon_{k0}^{2\mathrm{p}}) \frac{\Omega}{8\pi} \sum_{\mathbf{q}_1,\mathbf{q}_2,\mathbf{k}_0} \frac{1}{q_1^2 q_2^2} \times \left| \frac{F(\mathbf{k}_0-\mathbf{q}_1-\mathbf{q}_2)}{\epsilon_{k0}^{2\mathrm{p}} - \epsilon_{|\mathbf{k}_0-\mathbf{q}_1|} - \hbar\omega_{\mathrm{LO}}} + \frac{F(\mathbf{k}_0-\mathbf{q}_1-\mathbf{q}_2)}{\epsilon_{k0}^{2\mathrm{p}} - \epsilon_{|\mathbf{k}_0-\mathbf{q}_2|} - \hbar\omega_{\mathrm{LO}}} + \sum_{\ell_\nu,n_\nu,m_\nu} \frac{M_{f\nu}^{q_2} M_{\nu i}^{q_1} + M_{f\nu}^{q_1} M_{\nu i}^{q_2}}{\epsilon_{k0}^{2\mathrm{p}} - \epsilon_\nu - \hbar\omega_{\mathrm{LO}}} \right|^2, \tag{3.32}$$

where the last sum is performed over all intermediate quantum-dot states. We note here that the final dot state can also act as an intermediate state.

Dot-size dependence

In this section we will show the dot-size dependence of the two-phonon capture time, $\tau_{\ell,n}$, and we will discuss the influence of the different intermediate states on the total capture time. The capture time is shown in Figure 3.7 together with the single-phonon capture time from Figure 3.3 for comparison. Capture times for the first $\ell = 0$ and the first and second $\ell = 1$ bands are shown. The calculated two-phonon capture times into $(0,1)$ and $(1,1)$ are of the order of some picoseconds at $n = 10^{17}\mathrm{cm}^{-3}$. This is approximately an order of magnitude longer than the single-phonon capture times into these states. The two-phonon capture time into the $(1,2)$ energy level is close to one picosecond which is only slightly longer than the single-phonon capture time. We have limited the number of intermediate states to those with $\ell \in [0,5]$. The first $\ell = 6$ state becomes bound at $a = 15.4$ nm, so we have only calculated capture rates up to this radius.

We have investigated the influence of the different intermediate states on the total carrier capture rate by "turning off" contributions from other states. Figure 3.8 shows the capture time where only the contributions of continuum intermediate states have been included.

In the case of capture into the level $(0,1)$, a single energy level is present in the dot. For instance, at a binding energy $\epsilon_d \approx 2\hbar\omega_{\mathrm{LO}}$, the contribution from continuum intermediate states (neglecting spin degeneracy) gives a capture rate $R = 1.3 \times 10^{11}$ s^{-1} ($\tau \approx 8$ ps) and the corresponding contribution from the state itself gives $R = 4 \times 10^{11}$ s^{-1}. The total capture

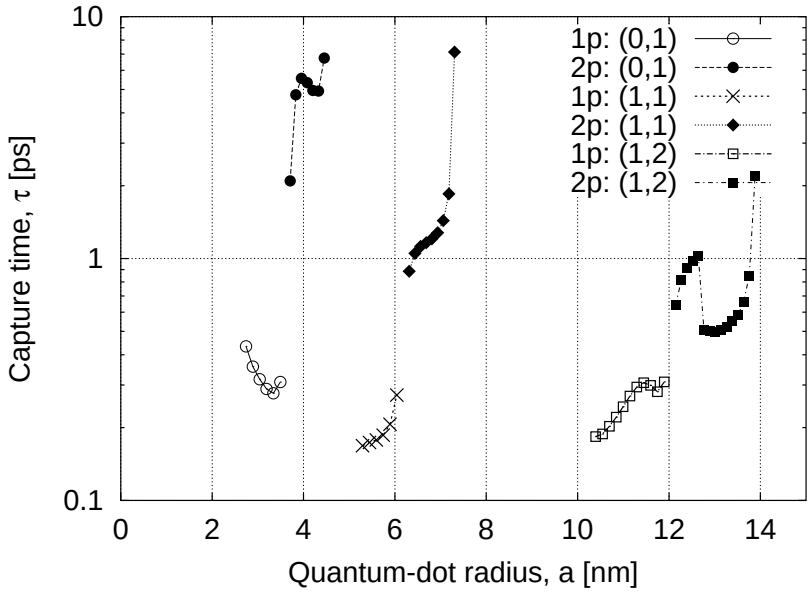

Figure 3.7: The two-phonon capture time ('2p') into the levels (0,1), (1,1) and (1,2) shown with the single-phonon capture time ('1p') for comparison. We use the same dot parameters as in Fig. 3.2 and $n_{3D} = 10^{17}$ cm^{-3}.

rate, with all contributions included, is however lower; $R = 8 \times 10^{10}$ s^{-1} ($\tau = 12.5$ ps). This suggests that destructive interference between the two contributions takes place. Mathematically, this can be explained by the difference in sign of the denominator in Eq. (3.21) corresponding to the different contributions. The denominator corresponding to continuum intermediate states is always negative. Denominators for discrete intermediate states can be either positive or negative depending on the relative level position, the crossing point from negative to positive is where an intermediate (discrete) state is $\hbar\omega_{\mathrm{LO}}$ above the state to be captured into.

A comparison of the capture times into $(1,1)$ in Figures 3.7 and 3.8 shows that the contribution of continuum states dominates. In this case two levels are bound to the dot, a strongly bound $l = 0$ state and the level itself. The matrix elements corresponding to different intermediate states are approximately of the same order. However, denominators corresponding to discrete intermediate states are equal to or larger than $\hbar\omega_{\mathrm{LO}}$ while the denominator for continuous states is small and negative. Therefore, con-

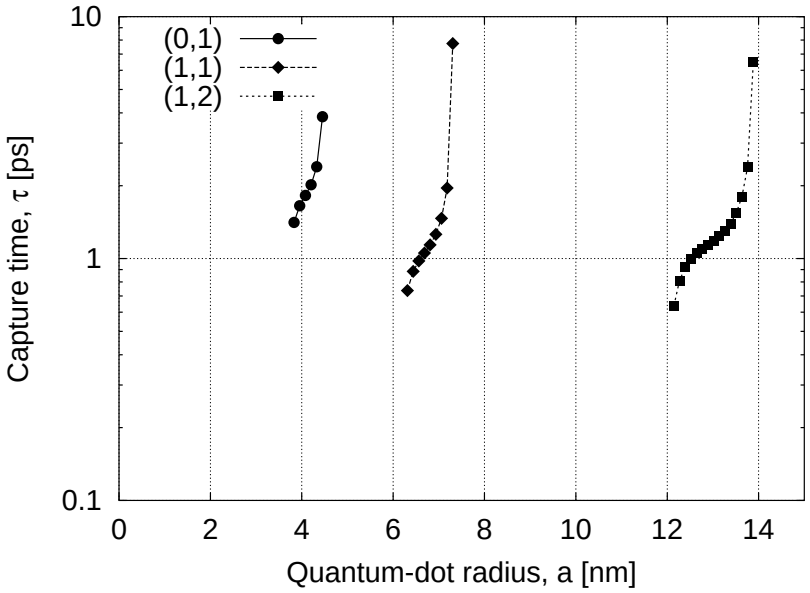

Figure 3.8: The two-phonon capture time where only the contribution via continuous intermediate states has been taken into account.

tribution from continuous intermediate states is dominant. Furthermore, in this particular case, interference between contributions from continuum and discrete states is negligible because the calculations show that they are $\pi/2$ out of phase. In general such an interference pattern is complex due to the fact that we sum over intermediate states *and* the calculation of the total capture rate includes sum over ℓ and m as well. The reader might ask him/herself at this point why we have not investigated the interference pattern for capture into a given (ℓ, m). The reason is the following: Due to the many integrations involved in calculations of R and long running times of programs, we have assumed that $\mathbf{k}_0 \| \hat{z}$ in the coordinate system of the quantum-dot wave functions and we have replaced the integral over the directions of $\mathbf{k}_0$ by 4π. We show in Appendix E that the *total* capture rate is independent of this choice of the direction of $\mathbf{k}_0$ *but* the capture rate into individual (ℓ, m) cannot be obtained with this approximation. This is shown in the case of single-phonon capture but the same conclusion holds for two-phonon capture.

In the case of capture into the $(0, 2)$ and $(0, 3)$ band results cannot be

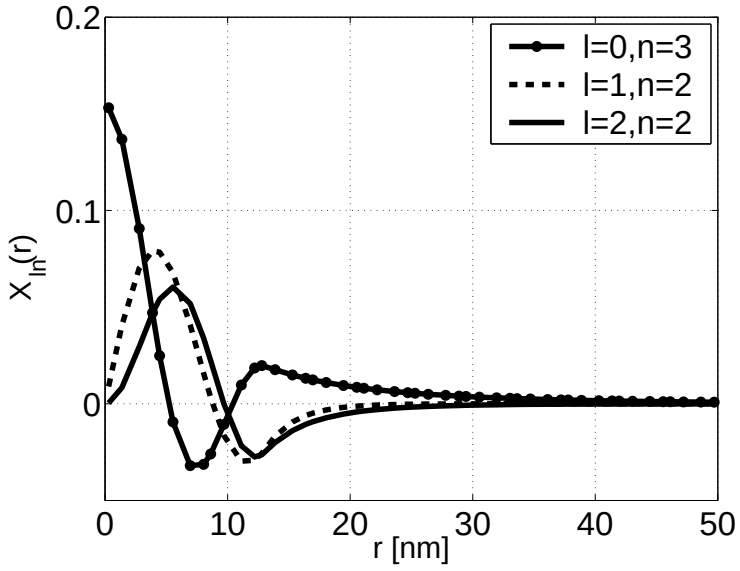

Figure 3.9: Radial wavefunctions, $\chi_{\ell n}(r)$, at $a = 13.1$ nm.

shown since, in this case, there exist discrete intermediate carrier states lying $\hbar\omega_{\mathrm{LO}}$ above the state to be captured into (see Figure 3.2). In this case the perturbative approach that we have chosen is no longer valid and a different approach is needed.

A comparison of Figures 3.7 and 3.8 shows that close to $a_{\min}$ in the $(1, 2)$ band, the curves are similar. This suggests that the contribution of continuum intermediate states dominates. At $a = 12.8$ nm, a local decrease is seen in the total capture time while the "partial" capture time, where only continuum intermediate states are taken into account, continues to increase. This decrease is found to be associated with the binding of the $(2, 2)$ level. No decrease is observed in the capture time with the binding of $(0, 3)$ at a slightly larger radius, $a = 13$ nm. This can be understood in terms of overlap of the different radial wave functions with the final state wave functions. The radial wave functions are shown in Figure 3.9 at $a = 13.1$ nm, where both $(2, 2)$ and $(0, 3)$ are bound. χ_{12} and χ_{22} have the same number of nodes and behave very similarly. Their overlap is therefore very good, and this gives the local increase in the capture rate. On the other hand χ_{03} is out of phase with those functions and therefore does not contribute

significantly to the capture rate. No step is observed in the capture rate into $(0,1)$ and $(1,1)$ as no new energy level becomes bound in the dot in these bands.

The discussion above shows clearly that the total capture rate depends on the interference between contributions from the different intermediate states. The character of the interference can to a large extent be identified by the sign of the denominators of the different terms that enter into the capture rate [see Eq. (3.32)]. An increase of possible intermediate states *does not* necessarily lead to a simple increase in the capture rate. Furthermore, the contribution of an intermediate state depends strongly on the overlap of its radial wave function with the radial wave function of the final state. This was shown in the case of carrier capture into the $(1,2)$ level.

Temperature dependence

The two-phonon capture rate depends on temperature via the Fermi and the phonon factor as

$$R_T^{2\mathrm{p}} \propto f(\epsilon_{k_0})(\overline{n}+1)^2. \tag{3.33}$$

The factor in Eq. (3.33) is shown in Figure 3.10. As in the case of single-phonon capture, $\epsilon_{k0}^{2\mathrm{p}}$ varies from $\hbar\omega_{\mathrm{LO}}$ to 0 within one radius band. At low temperatures, the phonon factor, $(\overline{n}+1)^2$, is very close to 1 and the behavior is similar to the case of single-phonon capture. At higher temperatures the average phonon population increases. This leads to the "flattening" of the capture rate dependence at these temperatures in comparison to the corresponding factor in single-phonon capture.

3.3 Carrier-density dependence in single- and two-phonon capture

Capture rates depend on carrier density through the Fermi factor,

$$R_N \propto f(\epsilon_{k_0}), \tag{3.34}$$

for both single- and two-phonon capture. At low and moderate carrier densities, the Fermi distribution approaches a Boltzmann distribution,

$$f_B(\epsilon_{k_0}) = \frac{n}{\overline{n}_{3D}} \exp\left(-\frac{\epsilon_{k_0}}{k_B T}\right), \tag{3.35}$$

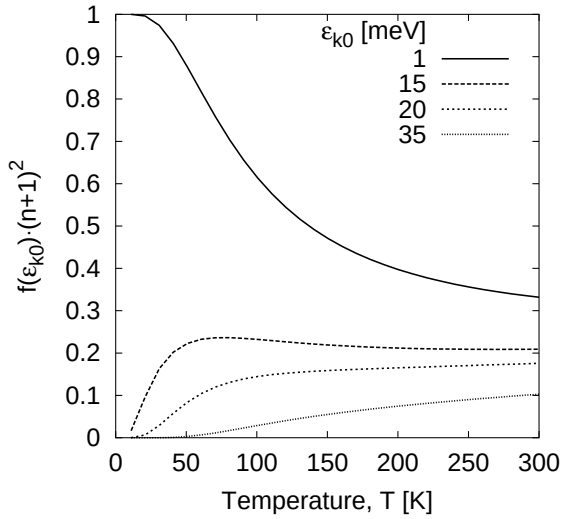

Figure 3.10: The factor $f(\epsilon_{k_0})(\overline{n}+1)^2$ plotted versud temperature for different energies of the incident carrier.

where $\overline{n}_{3D} = 2(m^* k_B T/(2\pi\hbar^2))^{3/2}$ [50] is a three-dimensional "density of states". At these densities, we can therefore define

$$R = An. \tag{3.36}$$

This was also discussed in section 2.4. The coefficients A can be determined from Figure 3.11, where the capture time, $\tau_{\ell,n}$, is plotted as a function of carrier density. The value for the single-phonon process is $A^{1\mathrm{p}} = 3.8 \times 10^{-5}$ cm^3/s and $A^{2\mathrm{p}} = 1.9 \times 10^{-6}$ cm^3/s for the two-phonon capture. The effective capture time can now be evaluated from Eq. (2.13) using the calculated values for the A-coefficients once the dot density, N_D, has been estimated. In quantum-dot based devices, several layers of dots are grown to increase their gain. To estimate a typical value of N_D, we assume that the interlayer distance is about 20 nm. For a typical areal dot density 5×10^{14} m^{-2}, the dot density is then $N_D = 2.5 \times 10^{16}$ cm^{-3}, and the effective capture times for single- and two-phonon processes become $\tau_c^{1\mathrm{p}} = 1.1$ ps and $\tau_c^{2\mathrm{p}} = 21$ ps.

We can also express the capture rate through the capture cross-section as

$$R = \sigma n v_T, \tag{3.37}$$

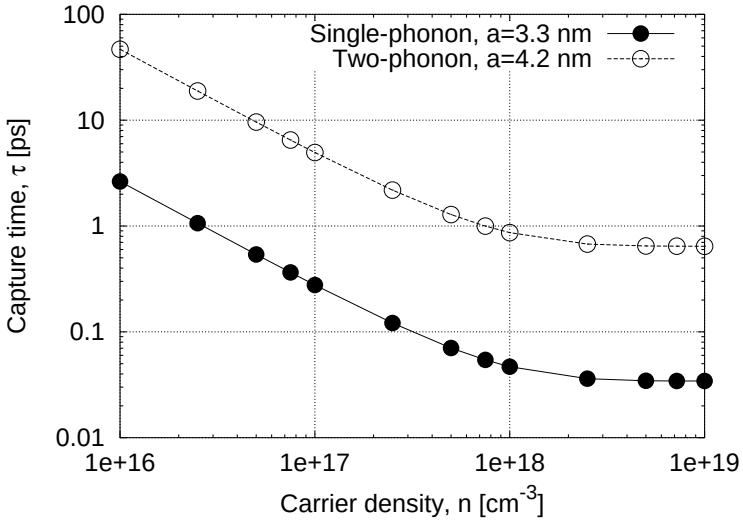

Figure 3.11: Carrier density of the one- and two-phonon capture times for two different dot sizes in the $(0, 1)$ band.

where v_T is the thermal velocity of the electron gas, given by $mv_T^2 = k_B T$. By comparing Eq. (3.37) with (3.36), we obtain that $\sigma^{1\mathrm{p}} = 1.5 \cdot 10^{-12}$ cm^2 and $\sigma^{2\mathrm{p}} = 7.5 \cdot 10^{-14}$ cm^2. The latter value is close to an estimate in a calculation of gain dynamics in quantum-dot lasers [52].

In this chapter, calculations of single- and two-phonon-mediated capture rates into quantum dots were presented. Two-phonon capture rates were calculated to be at most one order of magnitude lower than single-phonon capture rates. The capture rates were calculated as a function of dot size and, in the case of two-phonon capture, the influence of various intermediate states on the total capture rate was investigated. The sign of the denominator that enters the two-phonon capture rate in the sum over intermediate states was shown to play a crucial role. With increasing number of states in the dot, the interference pattern becomes more complex and depends strongly on the energy separation between the different dot levels. The capture-time dependence on temperature and carrier density was furthermore investigated.

Chapter 4

Phonon-mediated capture to a charged quantum dot

In the previous chapter, calculations of carrier capture rates into quantum dots by emission of one or two LO phonons were presented. In these calculations it was assumed that the quantum-dot state, to which the capture takes place, was empty initially. To date this has also been assumed in other calculations of carrier capture rates [21, 34, 36, 38]. For highly excited quantum-dot systems, such as lasers or optical amplifiers, it is important to understand how the carrier capture rate is altered if one or more carriers are already present in the dot. This question is addressed in this chapter. We will assume that either a hole or an electron occupies the first excited state and calculate the probability that a second carrier, either an electron or a hole, is captured to the first excited state. A schematic illustration of one such process is shown in Fig. 4.1, where an electron (or a hole) is captured into a quantum-dot state in which an electron (or a hole) is already present. Once the second carrier has been captured, an Auger process can take place; one carrier relaxes to the ground state while the other is excited to the wetting layer. This Auger process has been shown to be very fast [21].

4.1 Quantum-dot single-particle energy levels

The quantum dot is approximated by a cone floating on a wetting layer a few monolayer thick. Figure 4.2 illustrates the geometry of the dot and the

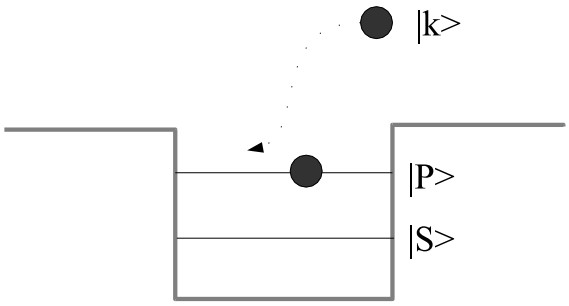

Figure 4.1: Capture into a charged quantum dot.

wetting layer. The Hamiltonian is rotationally invariant around the z-axis. The states can be labeled by an angular momentum quantum number, m, that describes rotation around the z-axis. They are also labeled by n, where $n-1$ is the number of radial nodes in the plane. The wave functions are given in Appendix D. Here we focus on $n = 1$. The states are labeled by $|1S\rangle$ ($m = 0$), $|1P_{\pm}\rangle$ ($m = \pm 1$) etc. (the "1" refers to $n = 1$). We note here that S and P do not refer to $\ell = 0$ and $\ell = 1$ as in the case of a spherically symmetric dot. All states, apart from the ground state, are two-fold degenerate (not counting spin) whereas in a dot of spherical symmetry, a state ℓ is $(2\ell + 1)$ times degenerate. The in-plane and z-dependent parts of the wave functions for $|1S\rangle$ and $|1P\rangle$ are shown in Fig. 4.3 for one specific dot geometry. The wetting-layer wave functions are approximated by the functions of a thin quantum well with the same confinement energy as the quantum dot. The solutions are given in Appendix D as well. Figs. 4.4 and 4.5 show the single-particle electron and hole energy levels for $|1S\rangle$ and $|1P\rangle$ for two dot geometries; a non-truncated cone with a small basis angle, $\alpha = 12^\circ$, and a truncated cone with $\alpha = 30^\circ$ and $h = 3$ nm. The value of confinement potentials is taken from Ref. [19], $V_e = 697$ meV and $V_h = 288$ meV for electrons and holes, respectively. We use electron and hole masses $m_e = 0.07m_0$ and $m_h = 0.34m_0$, where m_0 is the free-electron mass. For a typical dot radius $r_0 \sim 10$ nm the typical energy spacing,

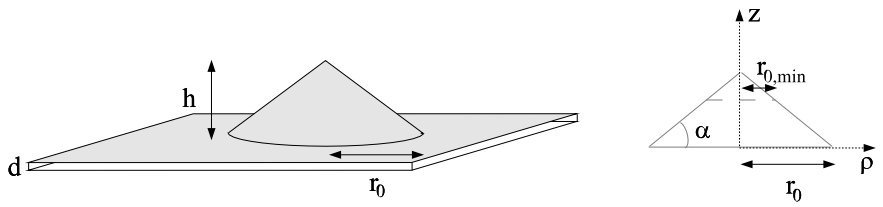

Figure 4.2: Cone-shaped quantum dot floating on a wetting layer of thickness d. h is the cone height, r_0 the in-plane radius and α is the base angle. The cone can also be truncated, shown in the right panel with a dashed line. The upper radius is labeled by $r_{0,\mathrm{min}}$ and the height is then determined by $h = \tan\alpha(r_0 - r_{0,\mathrm{min}})$.

$E_P - E_S$, is $\sim$ 100 meV for electrons and $\sim$ 60 meV for holes. At large radii the energy spacing diminishes for $\alpha = 30°$ for both electrons and holes whereas it remains approximately constant for $\alpha = 12°$. The model presented here is a single-band model and no strain or piezoelectric effects are included. It should be mentioned here that the present wave-function model has been compared quantitatively to the eight-band $\mathbf{k} \cdot \mathbf{p}$ model presented in Ref. [23]. For the same values of confinement potential and effective mass as in Ref. [23], $V_e = 413$ meV and $m_e = 0.067 m_0$, an excellent quantitative agreement between the two models has been obtained [53].

4.2 Carrier capture into a quantum-dot state occupied by a carrier of different type

In this section, we present calculations of carrier capture rates into a quantum dot that is already occupied by a carrier of a different type. We start by identifying the initial and final states. Carrier capture rates for the present wave-function model are derived and numerical results presented.

4.2.1 Initial and final carrier states

The two-particle state is treated with first-order perturbation theory. A priori we can neglect the Coulomb interaction in the initial state since one carrier is delocalized and the other localized while in the final state the carriers' mutual interaction is expected to be strong due to the localization of both carriers. The particles, one electron and one hole, are discernable

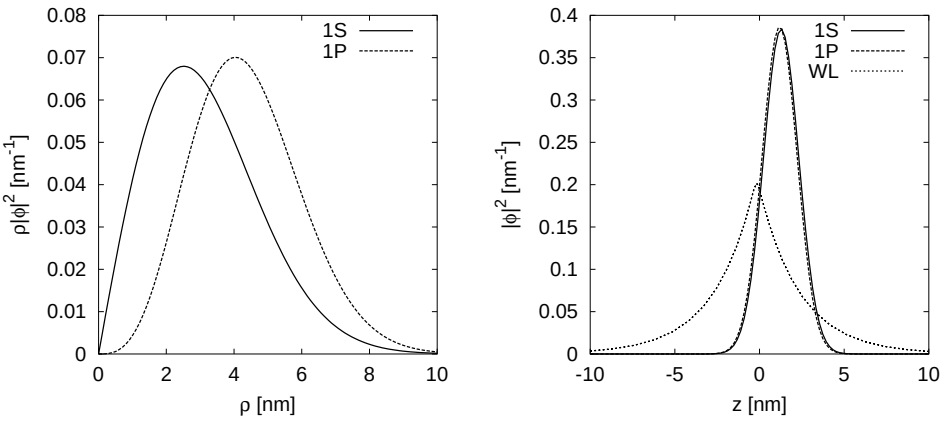

Figure 4.3: Wave functions for an electron in a dot with $r_0 = 10$ nm, $r_{0,\min} = 4.8$ nm, $h = 3$ nm, $\alpha = 30°$, $V_e = 697$ meV. The in-plane probability density $\rho|\Phi_\perp(\rho)|^2$ is shown in the left panel and $|\Phi_z(z)|^2$ is shown in the right panel together with the wetting-layer wave function $|\Phi_{\mathrm{WL}}|^2$.

and there is therefore no need for antisymmetrization of the two-particle state.

The initial state is expressed as

$$|\Psi_i\rangle = |\mathbf{k}_c\rangle|1P_d\rangle, \tag{4.1}$$

where the subscripts "c" and "d" denote the wetting-layer carrier that will be captured and the quantum-dot carrier, respectively. Since we neglect the Coulomb interaction of the carriers, the energy of this initial state is given by the single-particle energies of the two particles. The final state is expressed as

$$|\Psi_f\rangle = |1P_c\rangle|1P_d\rangle, \tag{4.2}$$

with energy

$$E = E^e_{1P} + E^h_{1P} + E_X, \tag{4.3}$$

where $E^{e,h}_{1P}$ is the single-particle energy for an electron or a hole. E_X is given by

$$E_X = \int d^3r_c d^3r_d \Psi^*_c(\mathbf{r}_c)\Psi^*_d(\mathbf{r}_d)V_c(|\mathbf{r}_c - \mathbf{r}_d|)\Psi_c(\mathbf{r}_c)\Psi_d(\mathbf{r}_d). \tag{4.4}$$

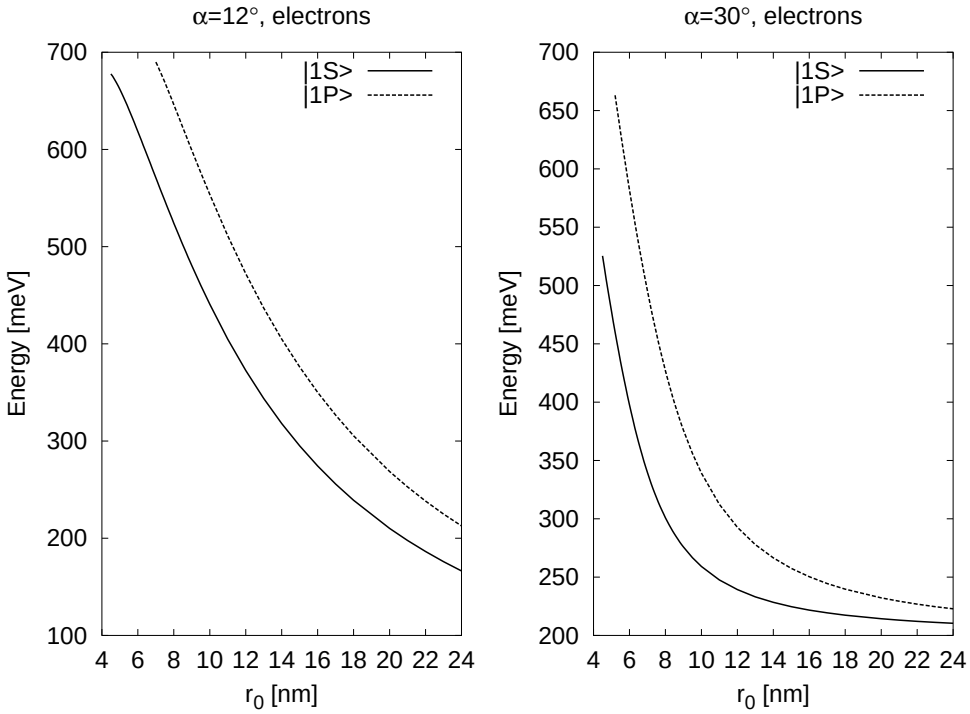

Figure 4.4: Single-particle energy levels $|1S\rangle$ and $|1P\rangle$ for electrons in two different dot geometries versus the in-plane radius. For $\alpha = 12°$ (left panel) the dot is non-truncated. The right panel represents a truncated cone with $\alpha = 30°$ and height $h = 3$ nm. $V_e = 697$ meV and $d = 0.33$ nm.

The Coulomb potential is given by

$$V_c(r) = -\frac{e^2}{4\pi\epsilon_r\epsilon_0 r}, \tag{4.5}$$

where ϵ_r is the dielectric constant and ϵ_0 is the permittivity constant. $\Psi_c(\mathbf{r}_c)$ and $\Psi_d(\mathbf{r}_d)$ are the quantum-dot wave functions of the captured carrier and the quantum-dot carrier, respectively. The Coulomb integral in Eq. (4.4) is shown in Figure 4.6 for two different quantum-dot geometries. Also shown in Fig. 4.6 are Coulomb integrals for two electrons and two holes. These will be discussed later in this chapter in connection with carrier capture where the two particles are identical.

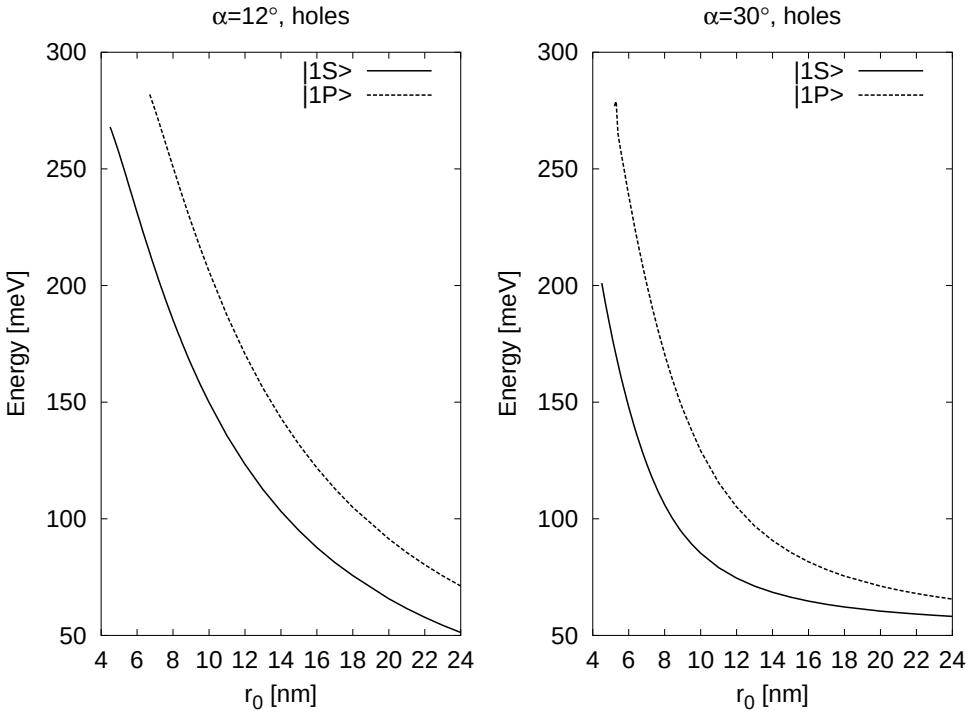

Figure 4.5: Single-particle energy levels $|1S\rangle$ and $|1P\rangle$ for holes in two different dot geometries versus the in-plane radius. For $\alpha = 12°$ (left panel) the dot is non-truncated. The right panel represents a truncated cone with $\alpha = 30°$ and height $h = 3$ nm. $V_h = 288$ meV and $d = 0.33$ nm.

4.2.2 Capture rate

In this section we derive expressions for the carrier capture rate. The derivation applies to the capture of an electron into a dot that is occupied by a hole or the capture of a hole into a dot occupied by an electron. For definiteness we assume that the carrier is captured into $|1P\rangle$ while the other carrier also occupies $|1P\rangle$. This choice is made because we expect Coulomb correlations to be larger for this configuration than for a dot carrier occupying for instance $|1S\rangle$.

The Fröhlich Hamiltonian for phonon emission is a two-particle Hamil-

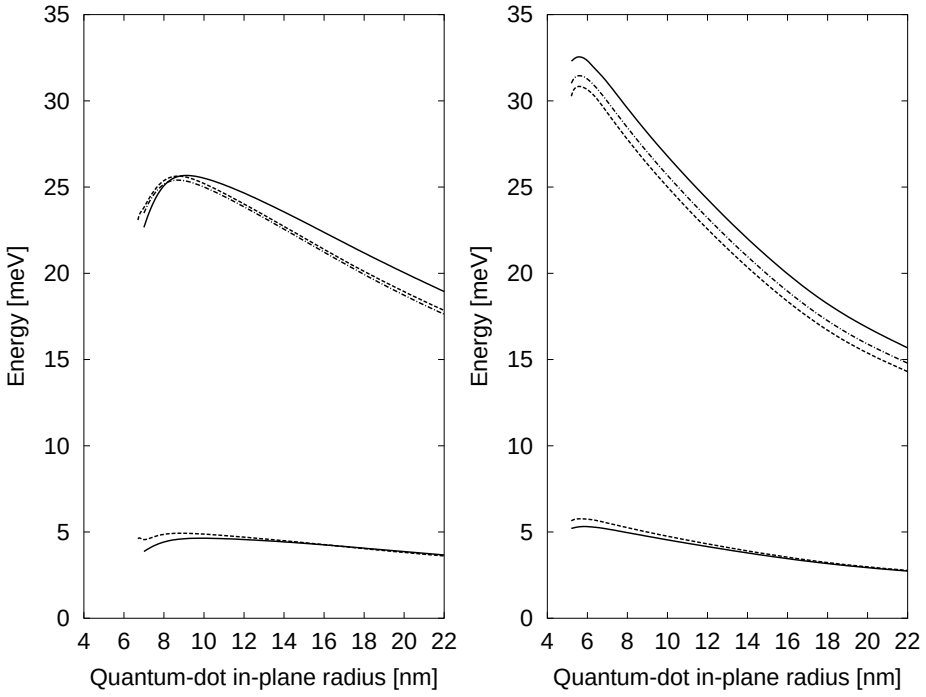

Figure 4.6: Direct and exchange Coulomb integrals as a function of in-plane dot radius, the left panel with quantum dot basis angle $\alpha = 12°$ and the right panel with $\alpha = 30°$. The direct integrals (higher energy) are shown for electrons (solid), holes (dashed) and one electron and one hole (dashed-dotted line; absolute value). The exchange integrals, corresponding two electrons (solid) or two holes (dashed) in the dot are the lowest two curves. The results in the left panel are also given in Ref. [21].

tonian because both particles interact with phonons. It is given by

$$\hat{V}_{\mathbf{q}}^{\mathrm{em}} = H_{\mathrm{c-ph}} + H_{\mathrm{d-ph}} \tag{4.6}$$

$$= \alpha(q)e^{-i\mathbf{q}\cdot\mathbf{r}_c}\hat{a}_{\mathbf{q}}^{\dagger} - \alpha(q)e^{-i\mathbf{q}\cdot\mathbf{r}_d}\hat{a}_{\mathbf{q}}^{\dagger}, \tag{4.7}$$

where $H_{\mathrm{c-ph}}$ and $H_{\mathrm{d-ph}}$ are the Hamiltonians for electrons and holes respectively. We recall that the Fröhlich interaction is a Coulomb interaction. Therefore, $H_{\mathrm{c-ph}}$ and $H_{\mathrm{d-ph}}$ are simply related as $H_{\text{c-ph}} = -H_{\text{d-ph}}$ due to the opposite charge of electrons and holes, hence the minus sign in

Eq. (4.7).[1] The capture rate of a carrier of given spin is given by

$$R = \frac{2\pi}{\hbar}(\overline{n}+1)\sum_{\mathbf{k}_c,\mathbf{q}} |\alpha(q)|^2 \left|\left\langle \Psi_{\mathrm{f}} \left| e^{-i\mathbf{q}\cdot\mathbf{r}_c} - e^{-i\mathbf{q}\cdot\mathbf{r}_d} \right| \Psi_{\mathrm{i}} \right\rangle\right|^2 \delta(E_f - E_i), \quad (4.8)$$

where E_i and E_f are the energies of the initial and final states. We have that $\left\langle \Psi_{\mathrm{f}}|e^{-i\mathbf{q}\cdot\mathbf{r}_d}|\Psi_{\mathrm{i}}\right\rangle = 0$. This can be seen from

$$\begin{aligned}
\left\langle \Psi_{\mathrm{f}}|e^{-i\mathbf{q}\cdot\mathbf{r}_d}|\Psi_{\mathrm{i}}\right\rangle &= \int d^3r_c d^3r_d \Psi_f^*(\mathbf{r}_c,\mathbf{r}_d) e^{-i\mathbf{q}\cdot\mathbf{r}_d}\Psi_i(\mathbf{r}_c,\mathbf{r}_d) \\
&= \int d^3r_c d^3r_d \Psi_{P_d}^*(\mathbf{r}_d)\Psi_{P_c}^*(\mathbf{r}_c) e^{-i\mathbf{q}\cdot\mathbf{r}_d}\Psi_{k_c}(\mathbf{r}_c)\Psi_{P_d}(\mathbf{r}_d) \\
&= \int d^3r_d \Psi_{P_d}^*(\mathbf{r}_d) e^{-i\mathbf{q}\cdot\mathbf{r}_d}\Psi_{P_d}(\mathbf{r}_d) \cdot \int d^3r_c \Psi_{P_c}^*(\mathbf{r}_c)\Psi_{k_c}(\mathbf{r}_c) \\
&= 0,
\end{aligned} \quad (4.9)$$

since the last overlap integral is zero. It is zero because quantum-dot and wetting-layer wave functions for the captured carrier are orthogonal. The matrix element $\left\langle \Psi_{\mathrm{f}}|e^{-i\mathbf{q}\cdot\mathbf{r}_c}|\Psi_{\mathrm{i}}\right\rangle$ is given by

$$\begin{aligned}
\left\langle \Psi_{\mathrm{f}}|e^{-i\mathbf{q}\cdot\mathbf{r}_c}|\Psi_{\mathrm{i}}\right\rangle &= \int d^3r_c d^3r_d \Psi_f^*(\mathbf{r}_c,\mathbf{r}_d) e^{-i\mathbf{q}\cdot\mathbf{r}_c}\Psi_i(\mathbf{r}_c,\mathbf{r}_d) \\
&= \int d^3r_c d^3r_d \Psi_{P_d}^*(\mathbf{r}_d)\Psi_{P_c}^*(\mathbf{r}_c) e^{-i\mathbf{q}\cdot\mathbf{r}_c}\Psi_{k_c}(\mathbf{r}_c)\Psi_{P_d}(\mathbf{r}_d) \\
&= \int d^3r_c \Psi_{P_c}^*(\mathbf{r}_c) e^{-i\mathbf{q}\cdot\mathbf{r}_c}\Psi_{k_c}(\mathbf{r}_c) \int d^3r_d \left|\Psi_{P_d}(\mathbf{r}_d)\right|^2 \\
&= \int d^3r_c \Psi_{P_c}^*(\mathbf{r}_c) e^{-i\mathbf{q}\cdot\mathbf{r}_c}\Psi_{k_c}(\mathbf{r}_c),
\end{aligned} \quad (4.10)$$

where the last equality is obtained because the quantum-dot wave function is assumed to be normalized. The expression for the capture rate becomes

$$R = \frac{2\pi}{\hbar}(\overline{n}+1)\sum_{\mathbf{k}}\sum_{\mathbf{q}} |\alpha(q)|^2 \left|\left\langle 1P \left| e^{-i\mathbf{q}\cdot\mathbf{r}} \right| \mathbf{k} \right\rangle\right|^2 f(\epsilon_k)\delta(E_f - E_i), \quad (4.11)$$

[1] Actually, the Hamiltonian in Eq. (4.7) is defined for capture of an electron while the quantum dot is charged by a hole due to the choice of sign (compare to the definition in Eqs. (A.18) and (A.19)). However it is the matrix element squared that enters the capture rate and the sign therefore does not matter. The physics of the process is retained as long as the two Hamiltonians are of opposite sign.

where we have labeled the states $|1P\rangle$ and $|\mathbf{k}\rangle$ instead of $|1P_c\rangle$ and $|\mathbf{k}_c\rangle$ and we have set $\mathbf{r}_c \to \mathbf{r}$. The quantum-dot and the wetting-layer wave functions for the captured carrier are approximated by a separation of in-plane and z variables,

$$\begin{aligned} \Psi_k(\mathbf{r}) &= \Phi_k(\boldsymbol{\rho})\Phi_{\mathrm{WL}}(z) \\ \Psi_d(\mathbf{r}) &= \Phi_\perp(\boldsymbol{\rho})\Phi_z(z), \end{aligned} \tag{4.12}$$

where "$\perp$" refers to the plane that is perpendicular to the growth axis (z). We insert these wave functions into the expression for the capture rate in Eq. (4.11). The sum over phonon wave vectors $\mathbf{q}$ is transformed into an integral over $\mathbf{q}$ by

$$\sum_{\mathbf{q}} \longrightarrow \frac{\Omega}{(2\pi)^3}\int d^3q. \tag{4.13}$$

We also use Eqs. (A.18) and (A.19) to express $\alpha(q)$. We get

$$\begin{aligned} R = {} & \frac{2\pi}{\hbar}(\overline{n}+1)\frac{\Omega|\alpha_0|^2}{(2\pi)^3} \\ & \times \sum_{\mathbf{k}} f(\epsilon_k)\int d^2q_\perp dq_z \frac{1}{q_z^2+q_\perp^2}\left|\left\langle\Phi_\perp|e^{-i\mathbf{q}_\perp\cdot\boldsymbol{\rho}}|\Phi_k\right\rangle_\perp\right|^2 \\ & \times \int_{-\infty}^{+\infty} dz \int_{-\infty}^{+\infty} dz' \Phi_z^*(z)\Phi_{\mathrm{WL}}^*(z')e^{-iq_z(z-z')}\Phi_{\mathrm{WL}}(z)\Phi_z(z')\delta(E_f-E_i). \end{aligned} \tag{4.14}$$

The in-plane scalar product $\langle\phi|\psi\rangle_\perp$ is defined by

$$\langle\phi|\psi\rangle_\perp \equiv \int d^2\rho\phi^*(\boldsymbol{\rho})\psi(\boldsymbol{\rho}). \tag{4.15}$$

With the aid of

$$\int_{-\infty}^{+\infty} dq_z \frac{e^{-iq_z(z-z')}}{q_z^2+q_\perp^2} = \frac{\pi}{q_\perp}e^{-q_\perp|z-z'|}, \tag{4.16}$$

we obtain for the capture rate

$$\begin{aligned} R = {} & \frac{2\pi}{\hbar}(\overline{n}+1)\frac{\Omega|\alpha_0|^2\pi}{(2\pi)^3} \\ & \times \sum_{\mathbf{k}} \int dq_\perp F(q_\perp)d\phi_q \left|\left\langle\Phi_\perp|e^{-i\mathbf{q}_\perp\cdot\boldsymbol{\rho}}|\Phi_k\right\rangle_\perp\right|^2 f(\epsilon_k)\delta(E_f-E_i). \end{aligned} \tag{4.17}$$

We have defined the form factor

$$F(q_\perp) = \int_{-\infty}^{+\infty} dz \int_{-\infty}^{+\infty} dz' \Phi_z(z)\Phi_z(z')\Phi_{\mathrm{WL}}(z)\Phi_{\mathrm{WL}}(z')e^{-q_\perp|z-z'|} \quad (4.18)$$

that depends only upon the z-parts of the wetting-layer and quantum-dot wave functions. The in-plane scalar product is essentially a Fourier transform of the in-plane quantum-dot wave function because the in-plane part of the wetting-layer wave function is a plane wave [Eq. (D.11)]. The Fourier transform, Φ_P, is given in Eq. (D.9),

$$\left|\left\langle \Phi_\perp | e^{-i\mathbf{q}_\perp\cdot\boldsymbol{\rho}} | \Phi_k \right\rangle_\perp\right|^2 = \frac{|\Phi_P(\mathbf{k}-\mathbf{q}_\perp)|^2}{S}. \quad (4.19)$$

The energy conservation expressed by the δ function in Eq. (4.17) is given by

$$E_c + E_X + \hbar\omega_{\mathrm{LO}} = E^c_{\mathrm{WL}} + \hbar^2k^2/(2m_c), \quad (4.20)$$

where E_c is the energy of the captured quantum-dot carrier. Note here that E_d does not appear in the equation, i. e. the energy of the quantum-dot carrier that is already present in the dot. Thus for $E_X = 0$ the energy conservation is the one for phonon capture into an empty quantum dot and in fact the capture rate in Eq. (4.17) is then the capture rate into an empty dot!
We transform the sum over $\mathbf{k}$ into an integral over $\mathbf{k}$ by

$$\sum_{\mathbf{k}} \longrightarrow \frac{S}{(2\pi)^2}\int dk k d\phi_k = \frac{S}{2\pi}\int dk k, \quad (4.21)$$

where the last equality arises because there is no explicit dependence on ϕ_k in the integral in Eq. (4.17). Angular dependence occurs through the angle between $\mathbf{k}$ and $\mathbf{q}_\perp$ from the Fourier transform $\Phi_P(\mathbf{k}-\mathbf{q}_\perp)$. We label this angle by ϕ. With these considerations, the capture rate is expressed by

$$\begin{aligned} R = {} & \frac{\overline{n}+1}{4\pi\hbar}\Omega|\alpha_0|^2\frac{1}{2\pi}\int dk k f(\epsilon_k)\int dq_\perp F(q_\perp)\int d\phi|\Phi_P(\mathbf{k}-\mathbf{q}_\perp)|^2 \\ & \times\delta\left[E^c_{\mathrm{WL}} + \hbar^2k^2/(2m_c) - (E_c + E_X + \hbar\omega_{\mathrm{LO}})\right]. \end{aligned} \quad (4.22)$$

The δ function can be rewritten in terms of k [54],

$$\delta(E_k - E_{k_0}) = \frac{m_c}{\hbar^2 k}(\delta(k-k_0) + \delta(k+k_0)), \quad (4.23)$$

where

$$E_{k_0} = \frac{\hbar^2 k_0^2}{2m_c} = E_c + E_X + \hbar\omega_{\mathrm{LO}} - E_{\mathrm{WL}}^c. \tag{4.24}$$

This gives the capture rate

$$R = \frac{\overline{n}+1}{4\pi\hbar}\Omega|\alpha_0|^2 \frac{m_c}{2\pi\hbar^2} f(E_{k_0}) \int dq_\perp F(q_\perp) \int d\phi |\Phi_P(\mathbf{k}-\mathbf{q}_\perp)|^2. \tag{4.25}$$

The rate can also be expressed in terms of the two-dimensional density of states, $g_{2\mathrm{D}}$, given by

$$g_{2\mathrm{D}}(E) = \begin{cases} \frac{m_c}{2\pi\hbar^2} & E > 0 \\ 0 & E < 0. \end{cases} \tag{4.26}$$

The capture rate becomes

$$R = \frac{\overline{n}+1}{4\pi\hbar}\Omega|\alpha_0|^2 g_{2\mathrm{D}}(E_{k_0}) f(E_{k_0}) \int dq_\perp F(q_\perp) \int d\phi |\Phi_P(\mathbf{k}-\mathbf{q}_\perp)|^2. \tag{4.27}$$

The chemical potential in the Fermi distribution, $f(E_{k_0})$ [Eq. (3.7)], can be determined analytically for a two-dimensional electron gas. It is given by [50]

$$\frac{\mu}{k_B T} = \ln\left[\exp\left(\frac{\hbar^2\pi n_{2\mathrm{D}}}{m_c k_B T}\right) - 1\right]. \tag{4.28}$$

For $E_{k_0} - \mu >> k_B T$, the Fermi distribution can be approximated by

$$\begin{aligned} f(E_{k_0}) &\approx \exp\left(\frac{\mu - E_{k_0}}{k_B T}\right) \\ &\approx \frac{\hbar^2\pi n_{2\mathrm{D}}}{k_B T m_c} \exp\left(-\frac{E_{k_0}}{k_B T}\right), \end{aligned} \tag{4.29}$$

if $\hbar^2\pi n_{2\mathrm{D}}/(k_B T m_c) << 1$. This is the *Boltzmann approximation*. In the case where the Boltzmann approximation is valid, the carrier capture rate can be written as

$$R = A n_{2\mathrm{D}}. \tag{4.30}$$

Figure 4.7 shows the capture rate of electrons (left panel) and holes (right panel) as a function of the quantum dot in-plane radius, r_0. These are plotted with and without the Coulomb shift, E_X. The curves without

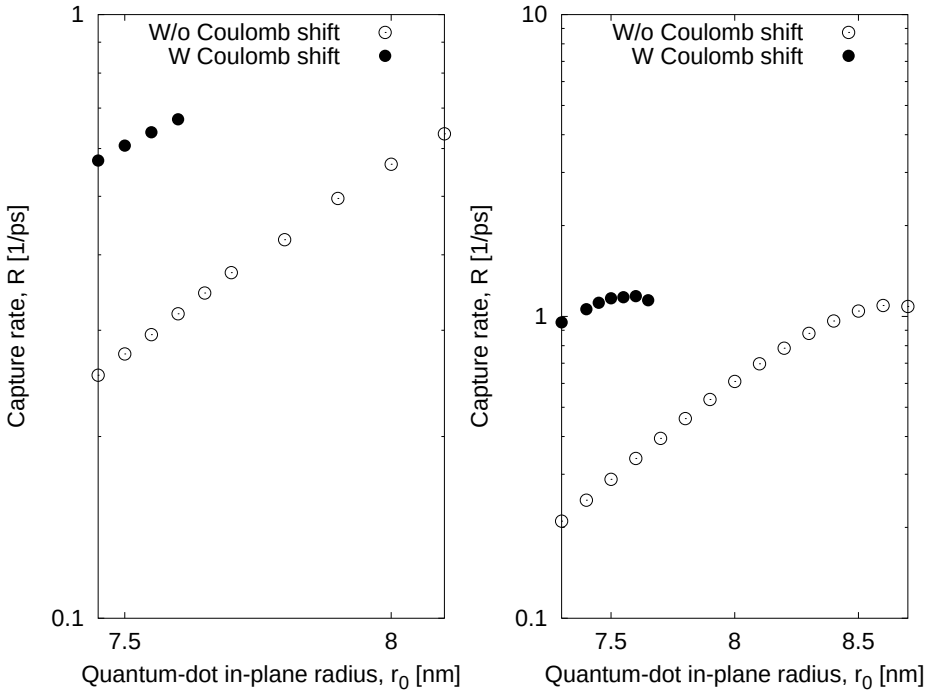

Figure 4.7: Capture rate as a function of the quantum-dot in-plane radius for capture of electrons (left panel) and holes (right panel). The curves labeled "w/o Coulomb shift" are for capture into an empty dot, i. e. for which $E_X = 0$. $n_{2D} = 10^{15}\mathrm{m}^{-2}$, $\alpha = 12°$, $d = 0.33$ nm.

the Coulomb shift ($E_X = 0$) correspond to capture into an empty dot and the results are the same as in Ref. [21]. For $E_X \neq 0$ the capture rate is the rate into a charged dot. The increasing rate with increasing r_0 arises due to the fact that at the same time the Fermi factor of the impinging carrier increases (the energy of the incident carrier approaches the wetting-layer band edge). The minimal in-plane radius is defined by the radius where E_c becomes bound to the dot ($E_c < E^c_{\mathrm{WL}}$). The *minimal* radius is the same in both cases, $E_X = 0$ and $E_X < 0$, because it is always required that E_c is bound. However, for $E_X < 0$, the *maximal* radius is smaller. This is because the capture rate is the same as capture into an empty dot only the bound level can be imagined to be lower in energy by $|E_X|$. The radius interval in this case becomes much smaller as $|E_X|$ (≈ 25 meV) is

an appreciable fraction of the LO phonon energy.

The radius interval for $\alpha = 30°$, either truncated or non-truncated is very small for both capture of electrons and holes. The radius band for electron capture into a charged dot is zero but for capture into an empty dot it is about 0.2 nm. For hole capture it is somewhat broader due to the slower decrease in single-particle energy with radius, 0.7 nm for non-charged dot and 0.2 nm for a charged dot. In any case the band is very narrow.

For an electron-hole pair that occupies $|1P\rangle$ it has been shown [39, 21] that intra-dot Auger relaxation in which an electron relaxes to $|1S\rangle$ and the hole is ejected into the wetting layer can be very fast, i. e. on a sub-picosecond and picosecond scale. In other words the non-radiative lifetime of the quantum-dot levels can be short due to the Coulomb interaction of the electron and hole. We include this effect phenomenologically by replacing the δ function in the expression for R with a linewidth broadening function. We write the linewidth function as a Lorentz function

$$L(E_f - E_i) = \frac{\hbar\Gamma}{\pi} \frac{1}{(E_f - E_i)^2 + (\hbar\Gamma)^2}, \tag{4.31}$$

where the factor $\hbar\Gamma/\pi$ ensures that L is normalized. The Auger scattering time is given by $\tau = 2/\Gamma$. We plot in Figure 4.8 the capture rate for different Auger scattering times from 0.5 ps to 10 ps. The inclusion of a Lorentz broadening function corresponds to relaxing the energy conservation condition that was expressed by the δ function before. The smaller the scattering time the broader the Lorentz function and the energy conservation is more relaxed. Therefore for the shortest scattering time the radius band is largest and for the longest scattering time it approaches the radius band without broadening. Within the radius band for capture without broadening ($r_0 \leq 7.6$ nm) the rates with broadening are somewhat diminished but not significantly. However, outside this radius band the rates with broadening decrease very fast. Even though we "gain" some radii where the capture is possible by taking the finite lifetime of the electron-hole pair into account this capture rate is not appreciable apart from a small radius interval above the radius band without broadening.

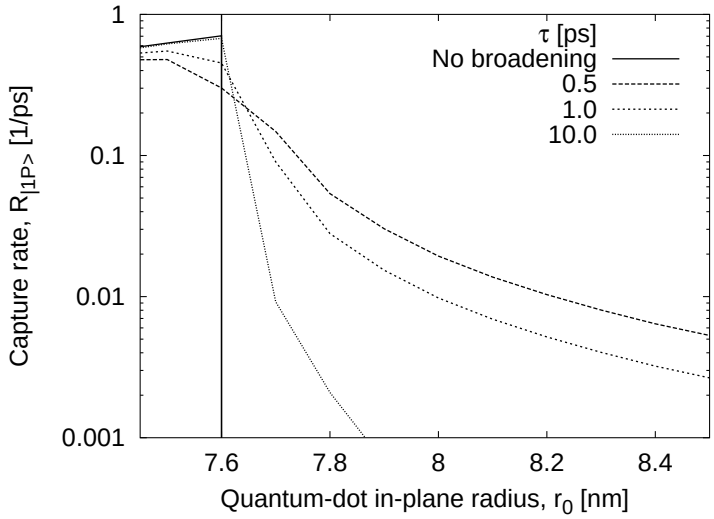

Figure 4.8: Capture rate into $|1P\rangle$ for different carrier-carrier scattering times. The vertical line indicates the largest radius within the radius band without broadening. $\alpha = 12°$ and $n_{2D} = 10^{15}\mathrm{m}^{-2}$.

4.3 Capture of an electron (hole) into a quantum dot occupied by an electron (hole)

In the previous section we focused on the case where the two carriers are of a different type, i. e. one electron and one hole. In this section we will investigate the case where the two particles are identical, two electrons or two holes. In this case the particles are indiscernable and it becomes necessary to antisymmetrize the two-particle state since the two particles are fermions.

4.3.1 Initial state

The possible initial states are given in Table 4.1. Depending on whether the two carriers have aligned or opposite spins, the spin and orbital states are listed. The total wave function needs to be antisymmetric. Therefore, if the spin state is antisymmetric, the orbital state is necessarily symmetric and vice versa.

The wave functions in Table 4.1 for the states $|P_{\pm}(j)\rangle$, $(j = 1, 2)$ are

	Spin state	Orbital state
Opposite spins	$\frac{\|\uparrow\downarrow\rangle \pm \|\downarrow\uparrow\rangle}{\sqrt{2}}$	$\frac{\|\mathbf{k}(1)P_\pm(2)\rangle \mp \|P_\pm(1)\mathbf{k}(2)\rangle}{\sqrt{2}}$
Aligned spins	$\|\uparrow\uparrow\rangle, \|\downarrow\downarrow\rangle$	$\frac{\|\mathbf{k}(1)P_\pm(2)\rangle - \|P_\pm(1)\mathbf{k}(2)\rangle}{\sqrt{2}}$

Table 4.1: The possible initial states with one wetting-layer carrier, labeled $|\mathbf{k}\rangle$ and one quantum-dot carrier in $|1P_\pm\rangle$. The table is to be read in the following way: In the initial state there is one wetting-layer carrier and the quantum-dot carrier state is either $|1P_+\rangle$ or $|1P_-\rangle$. Depending on whether the wetting-layer and quantum-dot carrier have opposite or aligned spins the possible two-particle states are listed.

denoted by

$$\Psi_P(\mathbf{r}_j) = P(j)e^{\pm i\phi_j}, \tag{4.32}$$

where $P(j)$ is the part of the wave function that depends on both z_j and the in-plane radius coordinate ρ_j. $P(j)$ is real which can be seen by a comparison of Eq. (4.32) with Eqs. (D.1) and (D.2). We recall here that the Fröhlich interaction is a Coulomb interaction and it therefore does not change the spin state of the two-particle state during the capture process. The orbital states that couple in the capture process can thus easily be determined.

4.3.2 Final state

The possible configurations for the two particles in the final state are shown in Table 4.2. In the following we will determine the energy levels of the different final states. Due to the cylindrical symmetry, the states can be classified according to the $z-$component of the total angular momentum.

$J_z = \pm 1$

For angular momentum $J_z = \pm 1$ the spins are aligned, either both up or both down. The orbital state is thus necessarily antisymmetric, given by

$$\left(|P_+(1)\rangle|P_-(2)\rangle - |P_-(1)\rangle|P_+(2)\rangle\right)/\sqrt{2}. \tag{4.33}$$

The energy of the states, to first order in V_c, is given by

$$\begin{aligned} E_{\pm 1} &= 2E_{1\mathrm{P}} + \langle \Psi_{\pm 1}|V_c|\Psi_{\pm 1}\rangle \\ &= 2E_{1\mathrm{P}} + \frac{1}{2}\Big[\langle P_-(2)| \langle P_+(1)|V_c|P_+(1)\rangle |P_-(2)\rangle \\ &+ \langle P_+(2)| \langle P_-(1)|V_c|P_-(1)\rangle |P_+(2)\rangle \\ &- \langle P_-(2)| \langle P_+(1)|V_c|P_-(1)\rangle |P_+(2)\rangle \\ &- \langle P_+(2)| \langle P_-(1)|V_c|P_+(1)\rangle |P_-(2)\rangle \Big]. \end{aligned} \tag{4.34}$$

The first two matrix elements in the square brackets are direct Coulomb integrals. They are equal due to the fact that the angular dependence cancels out,

$$\begin{aligned} &\langle P_-(2)| \langle P_+(1)|V_c|P_+(1)\rangle |P_-(2)\rangle \\ &= \iint d^3r_1 d^3r_2 P(1)P(2)V_c(|\mathbf{r}_1 - \mathbf{r}_2|)P(1)P(2), \\ &\langle P_+(2)| \langle P_-(1)|V_c|P_-(1)\rangle |P_+(2)\rangle \\ &= \iint d^3r_1 d^3r_2 P(1)P(2)V_c(|\mathbf{r}_1 - \mathbf{r}_2|)P(1)P(2). \end{aligned} \tag{4.35}$$

The last two matrix elements are exchange Coulomb integrals,

$$\begin{aligned} &\langle P_-(2)| \langle P_+(1)|V_c|P_-(1)\rangle |P_+(2)\rangle \\ &= \int\int d^3r_1 d^3r_2 P(1)e^{-i\phi_1}P(2)e^{i\phi_2}V_c(\mathbf{r}_1, \mathbf{r}_2)P(1)e^{-i\phi_1}P(2)e^{i\phi_2} \\ &= \frac{e^2}{4\pi\epsilon_r\epsilon_0}\int\int d\rho_1 d\rho_2 \rho_1\rho_2 dz_1 dz_2 (P(1)P(2))^2 \\ &\cdot \int_0^{2\pi}\int_0^{2\pi} d\phi_1 d\phi_2 \frac{e^{2i(\phi_2-\phi_1)}}{\sqrt{\rho_1^2+\rho_2^2-2\rho_1\rho_2\cos(\phi_1-\phi_2)+(z_1-z_2)^2}} \\ &= \frac{e^2}{4\pi\epsilon_r\epsilon_0}\int\int d\rho_1 d\rho_2 \rho_1\rho_2 dz_1 dz_2 (P(1)P(2))^2 \\ &\cdot 2\pi \int_0^{2\pi} du \frac{\cos(2u)+i\sin(2u)}{\sqrt{\rho_1^2+\rho_2^2-2\rho_1\rho_2\cos u+(z_1-z_2)^2}} \end{aligned} \tag{4.36}$$

$\|P_+\rangle$	$\|P_-\rangle$	σ_z	L_z	J_z
$\downarrow$	$\uparrow$	0	0	0
$\uparrow$	$\downarrow$	0	0	0
$\downarrow$	$\downarrow$	-1	0	-1
$\uparrow$	$\uparrow$	1	0	1
$\uparrow\downarrow$		0	2	2
	$\uparrow\downarrow$	0	-2	-2

Table 4.2: Possible configurations for the final state, i. e. two particles in $|1P\rangle$. $|P_+\rangle$ and $|P_-\rangle$ are the states with angular momentum quantum numbers $m = +1$ and $m = -1$, respectively.

The function in the denominator is even in u around $u = \pi$ but $\sin(2u)$ is odd around $u = \pi$. Therefore, the latter term does not contribute to the integral and $\langle P_-(2)| \langle P_+(1)|V_c|P_-(1)\rangle |P_+(2)\rangle \in \mathbf{R}$. It can easily be shown that the last term in Eq. (4.34) is the same as the term in Eq. (4.36). We label direct Coulomb integrals by J and exchange integrals by K. We thus obtain

$$E_{\pm 1} = 2E_{1\mathrm{P}} + J - K. \tag{4.37}$$

The program code that calculates the direct and exchange Coulomb integrals, J and K, is kindly provided by Robson Ferreira. Figure 4.6 shows J and K for two carriers in the quantum dot; two electrons, two holes or one electron and one hole. These are shown for two basis angles; $\alpha = 12°$ and $\alpha = 30°$. The direct and exchange integrals are very similar for the different particle types. At the smallest radius for each curve, the energy level(s) in question become(s) bound to the dot. As r_0 increases the extension, so to say, of the in-plane wave function, β_P, decreases leading to an increase in the Coulomb integrals. As r_0 increases further, β_P increases with a corresponding decrease in the Coulomb integrals. This behavior is also observed in quantum wells and quantum wires. Decrease of exciton binding energy with dot size has also been found in Refs. [55, 23, 24].

$\mathbf{J_z = \pm 2}$

For angular momentum $J_z = \pm 2$ it is seen from Table 4.2 that the two particles are in the same orbital state. Their orbital state is therefore symmetric and the spin state antisymmetric. The orbital state is $|P_\pm(1)\rangle|P_\pm(2)\rangle$ and

the energy is given by

$$\begin{aligned} E_{\pm 2} &= 2E_{1\mathrm{P}} + \langle P_{\pm}(2)P_{\pm}(1)\,|V_c|\,P_{\pm}(1)P_{\pm}(2)\rangle \\ &= 2E_{1\mathrm{P}} + J. \end{aligned} \tag{4.38}$$

$\mathbf{J_z = 0}$

There are two degenerate states with $J_z = 0$. The energies are therefore determined by the diagonalization of the subspace $J_z = 0$. The orbital state is spanned by the basis states $|P_+(1)P_-(2)\rangle$ and $|P_-(1)P_+(2)\rangle$,

$$|\Phi_0\rangle = a|P_+(1)P_-(2)\rangle + b|P_-(1)P_+(2)\rangle. \tag{4.39}$$

The matrix equation within this subspace can be written

$$\begin{pmatrix} 2E_{1\mathrm{P}} + J - E & K \\ K & 2E_{1\mathrm{P}} + J - E \end{pmatrix} \begin{pmatrix} a \\ b \end{pmatrix} = \begin{pmatrix} 0 \\ 0 \end{pmatrix}. \tag{4.40}$$

Eq. (4.40) was obtained by projecting onto the basis states $|P_+(1)P_-(2)\rangle$ and $|P_-(1)P_+(2)\rangle$. The energies are obtained by setting the determinant of the matrix in Eq. (4.40) equal to zero, giving

$$E = \begin{cases} 2E_{1\mathrm{P}} + J - K \\ 2E_{1\mathrm{P}} + J + K, \end{cases} \tag{4.41}$$

where the state associated with $E = 2E_{1\mathrm{P}} + J - K$ is given by

$$|\Phi_0^{(-)}\rangle = \frac{|P_+(1)P_-(2)\rangle - |P_-(1)P_+(2)\rangle}{\sqrt{2}}, \tag{4.42}$$

i. e. an orbital *antisymmetric* state. The state associated with $E = 2E_{1\mathrm{P}} + J + K$ is given by

$$|\Phi_0^{(+)}\rangle = \frac{|P_+(1)P_-(2)\rangle + |P_-(1)P_+(2)\rangle}{\sqrt{2}}, \tag{4.43}$$

i. e. an orbital *symmetric* wave function. The total states, where we also include the spin state, need to be antisymmetric. We therefore obtain

$$\begin{aligned} |\Psi_0^{(+)}\rangle &= \left(\frac{|P_+(1)P_-(2)\rangle - |P_+(2)P_-(1)\rangle}{\sqrt{2}}\right)\left(\frac{|\uparrow\downarrow\rangle + |\downarrow\uparrow\rangle}{\sqrt{2}}\right), \\ |\Psi_0^{(-)}\rangle &= \left(\frac{|P_+(1)P_-(2)\rangle + |P_+(2)P_-(1)\rangle}{\sqrt{2}}\right)\left(\frac{|\uparrow\downarrow\rangle - |\downarrow\uparrow\rangle}{\sqrt{2}}\right), \end{aligned} \tag{4.44}$$

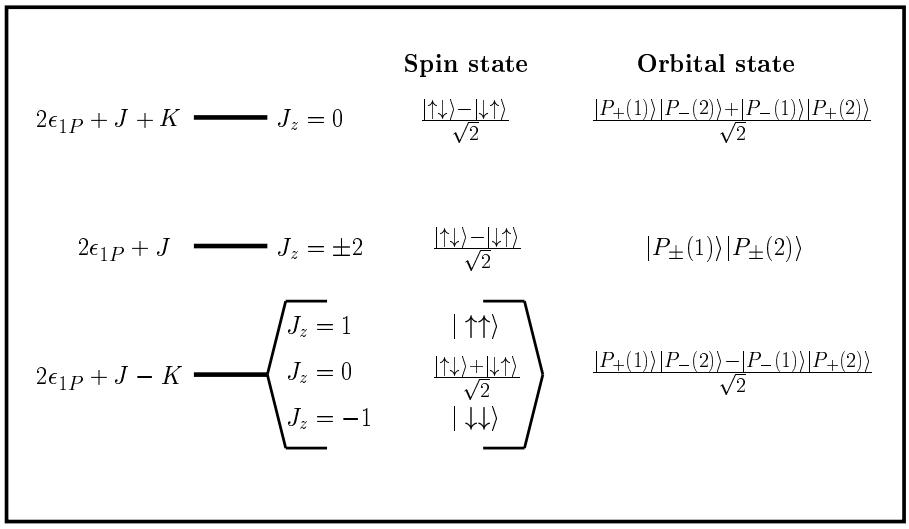

Figure 4.9: Energy levels and two-electron (hole) final states.

where the energy of states $|\Psi_0^{\pm}\rangle$ is given by $E = 2E_{1\mathrm{P}} + J \pm K$. The results obtained in this section are summarized in Fig. 4.9, where the total angular momentum J_z, the spin states and the orbital states are shown. The states with $J_z = 0$ are split in energy by $2K$, where K is the exchange Coulomb integral. The state with the higher energy $(E_{1\mathrm{P}} + J + K)$ is a singlet state but the state with the lower energy $(E_{1\mathrm{P}} + J - K)$ is a part of a triplet state, where the other two states have angular momentum $J_z = \pm 1$. The states $J_z = \pm 2$ both correspond to a singlet spin state.

4.3.3 General properties of matrix elements

The Fröhlich Hamiltonian for phonon emission is given by

$$\hat{V}_{\mathbf{q}}^{\mathrm{em}} = H_{\mathrm{c-ph}} + H_{\mathrm{d-ph}} \tag{4.45}$$

$$= \alpha(q) e^{-i\mathbf{q}\cdot\mathbf{r}_1} \hat{a}_{\mathbf{q}}^{\dagger} + \alpha(q) e^{-i\mathbf{q}\cdot\mathbf{r}_2} \hat{a}_{\mathbf{q}}^{\dagger}. \tag{4.46}$$

The matrix element that enters the capture rate is then given by

$$M = \left\langle \Psi_f | e^{-i\mathbf{q}\cdot\mathbf{r}_1} | \Psi_i \right\rangle + \left\langle \Psi_f | e^{-i\mathbf{q}\cdot\mathbf{r}_2} | \Psi_i \right\rangle . \tag{4.47}$$

Note the plus sign in Eq. (4.47) and compare it to Eq. (4.7). We have a plus sign because the two particles are identical. We would like to show

that these matrix elements are equal. For this purpose, we exchange $\mathbf{r}_1$ and $\mathbf{r}_2$ in the latter matrix element,

$$\begin{aligned}\left\langle \Psi_f|e^{-i\mathbf{q}\cdot\mathbf{r}_2}|\Psi_i\right\rangle &= \int\int d^3r_1 d^3r_2 \Psi_f^*(\mathbf{r}_1,\mathbf{r}_2)e^{-i\mathbf{q}\cdot\mathbf{r}_2}\Psi_i(\mathbf{r}_1,\mathbf{r}_2)\\ &= \int\int d^3r_1 d^3r_2 \Psi_f^*(\mathbf{r}_2,\mathbf{r}_1)e^{-i\mathbf{q}\cdot\mathbf{r}_1}\Psi_i(\mathbf{r}_2,\mathbf{r}_1)\\ &= \int\int d^3r_1 d^3r_2 \Psi_f^*(\mathbf{r}_1,\mathbf{r}_2)e^{-i\mathbf{q}\cdot\mathbf{r}_1}\Psi_i(\mathbf{r}_1,\mathbf{r}_2).\end{aligned} \tag{4.48}$$

In the last expression, we have used that the final and initial orbital state are *either* both symmetric *or* both antisymmetric because the spin state does not change in the capture process. The symmetry of the orbital state does therefore not change either. We have thus shown that

$$\left\langle \Psi_f|e^{-i\mathbf{q}\cdot\mathbf{r}_2}|\Psi_i\right\rangle = \left\langle \Psi_f|e^{-i\mathbf{q}\cdot\mathbf{r}_1}|\Psi_i\right\rangle \tag{4.49}$$

and thus

$$M = 2\left\langle \Psi_f|e^{-i\mathbf{q}\cdot\mathbf{r}_1}|\Psi_i\right\rangle. \tag{4.50}$$

4.3.4 Capture into the energy level $2E_{1\mathrm{P}} + J - K$

The energy level $E = E_{1\mathrm{P}} + J - K$ is a triplet state with the symmetric spin states $|\uparrow\uparrow\rangle$, $\frac{|\uparrow\downarrow\rangle+|\downarrow\uparrow\rangle}{\sqrt{2}}$ and $|\downarrow\downarrow\rangle$. The corresponding orbital state is the antisymmetric state

$$|A^{(f)}\rangle = \frac{|P_+(1)\rangle|P_-(2)\rangle - |P_-(1)\rangle|P_+(2)\rangle}{\sqrt{2}}. \tag{4.51}$$

This is the final state in the capture process.

The initial state (see Table 4.1) is given by

$$|A_\pm^{(i)}\rangle = \frac{|\mathbf{k}_1\rangle|P_\pm(2)\rangle - |\mathbf{k}_2\rangle|P_\pm(1)\rangle}{\sqrt{2}}. \tag{4.52}$$

We determine the matrix element according to Eq. (4.50),

$$\begin{aligned}M_A^\pm =& 2\left\langle A^{(f)}\left|e^{-i\mathbf{q}\cdot\mathbf{r}_1}\right|A_\pm^{(i)}\right\rangle\\ =& \langle P_-(2)|P_\pm(2)\rangle\left\langle P_+(1)|e^{-i\mathbf{q}\cdot\mathbf{r}_1}|\mathbf{k}_1\right\rangle\\ &- \langle P_+(2)|P_\pm(2)\rangle\left\langle P_-(1)|e^{-i\mathbf{q}\cdot\mathbf{r}_1}|\mathbf{k}_1\right\rangle\\ &- \langle P_-(2)|\mathbf{k}_2\rangle\left\langle P_+(1)|e^{-i\mathbf{q}\cdot\mathbf{r}_1}|P_\pm(1)\right\rangle\\ &+ \langle P_+(2)|\mathbf{k}_2\rangle\left\langle P_-(1)|e^{-i\mathbf{q}\cdot\mathbf{r}_1}|P_\pm(1)\right\rangle.\end{aligned} \tag{4.53}$$

The overlaps $\langle P_-(2)|\mathbf{k}_2\rangle$ and $\langle P_+(2)|\mathbf{k}_2\rangle$ are zero because the quantum-dot and wetting-layer states are orthogonal. Thus, the latter two terms are zero. Furthermore, we either have that $\langle P_-(2)|P_\pm(2)\rangle = 0$ and $\langle P_+(2)|P_\pm(2)\rangle = 1$ *or* vice versa. We can summarize these considerations with the following

$$M_A^\pm = \mp \left\langle P_\mp(1)|e^{-i\mathbf{q}\cdot\mathbf{r}_1}|\mathbf{k}_1\right\rangle. \tag{4.54}$$

4.3.5 Capture into the energy level $2E_{1\mathrm{P}} + J$

For capture into the energy level $2E_{1\mathrm{P}} + J$, the final orbital states are given by

$$\begin{cases} |S_1^{(f)}\rangle = |P_+(1)\rangle|P_+(2)\rangle, \\ |S_2^{(f)}\rangle = |P_-(1)\rangle|P_-(2)\rangle, \end{cases} \tag{4.55}$$

for which the spin state is the antisymmetric state $(|\uparrow\downarrow\rangle - |\downarrow\uparrow\rangle)/\sqrt{2}$.

The initial state is given by

$$|S_\pm^{(i)}\rangle = \frac{|\mathbf{k}_1\rangle|P_\pm(2)\rangle + |P_\pm(1)\rangle|\mathbf{k}_2\rangle}{\sqrt{2}}. \tag{4.56}$$

Due to orthogonality of $|P_+\rangle$ and $|P_-\rangle$ the state $|P_+(1)\rangle|P_+(2)\rangle$ only couples to $|S_+^{(i)}\rangle$ and $|P_-(1)\rangle|P_-(2)\rangle$ only couples to $|S_-^{(i)}\rangle$. The corresponding matrix elements are given by

$$\begin{aligned} M_S^{(1)} =& 2\left\langle S_1^{(f)}\left|e^{-i\mathbf{q}\cdot\mathbf{r}_1}\right|S_+^{(i)}\right\rangle \\ =& \sqrt{2}\langle P_+(1)|e^{-i\mathbf{q}\cdot\mathbf{r}_1}|\mathbf{k}_1\rangle, \end{aligned} \tag{4.57}$$

and, similarly,

$$\begin{aligned} M_S^{(2)} =& 2\left\langle S_2^{(f)}\left|e^{-i\mathbf{q}\cdot\mathbf{r}_1}\right|S_-^{(i)}\right\rangle \\ =& \sqrt{2}\langle P_-(1)|e^{-i\mathbf{q}\cdot\mathbf{r}_1}|\mathbf{k}_1\rangle. \end{aligned} \tag{4.58}$$

4.3.6 Capture into the energy level $2E_{1\mathrm{P}} + J + K$

For capture into the level $2E_{1\mathrm{P}} + J + K$, the final orbital state is given by

$$|S_3^{(f)}\rangle = \frac{|P_+(1)\rangle|P_-(2)\rangle + |P_-(1)\rangle|P_+(2)\rangle}{\sqrt{2}} \tag{4.59}$$

Quantum-dot energy level	$\lvert M\rvert^2 = 4\left\lvert\left\langle \Psi_f \middle\lvert e^{-i\mathbf{q}\cdot\mathbf{r}_1} \middle\rvert \Psi_i \right\rangle\right\rvert^2$
$2E_{1\mathrm{P}} + J - K$	$\lvert\langle P\lvert e^{-i\mathbf{q}\cdot\mathbf{r}}\rvert\mathbf{k}\rangle\rvert^2$
$2E_{1\mathrm{P}} + J$	$2\lvert\langle P\lvert e^{-i\mathbf{q}\cdot\mathbf{r}}\rvert\mathbf{k}\rangle\rvert^2$
$2E_{1\mathrm{P}} + J + K$	$\lvert\langle P\lvert e^{-i\mathbf{q}\cdot\mathbf{r}}\rvert\mathbf{k}\rangle\rvert^2$

Table 4.3: The matrix elements that enter the capture rate into the different two-particle energy levels.

and the spin state is the antisymmetric state $(|\uparrow\downarrow\rangle - |\downarrow\uparrow\rangle)/\sqrt{2}$.

The initial state is the same as for capture into $2E_{1\mathrm{P}} + J$, Eq. (4.56). The matrix element is very similar to the matrix element M_A (eq. (4.53)),

$$\begin{aligned} M_S^{(3)} =& 2\left\langle S_3^{(f)}|e^{-i\mathbf{q}\cdot\mathbf{r}_1}|S_\pm^{(i)}\right\rangle \\ =&\Big(\langle P_-(2)|P_\pm(2)\rangle \left\langle P_+(1)|e^{-i\mathbf{q}\cdot\mathbf{r}_1}|\mathbf{k}_1\right\rangle \\ &+ \langle P_+(2)|P_\pm(2)\rangle \left\langle P_-(1)|e^{-i\mathbf{q}\cdot\mathbf{r}_1}|\mathbf{k}_1\right\rangle \\ &+ \langle P_-(2)|\mathbf{k}_2\rangle \left\langle P_+(1)|e^{-i\mathbf{q}\cdot\mathbf{r}_1}|P_\pm(1)\right\rangle \\ &+ \langle P_+(2)|\mathbf{k}_2\rangle \left\langle P_-(1)|e^{-i\mathbf{q}\cdot\mathbf{r}_1}|P_\pm(1)\right\rangle .\Big) \end{aligned} \tag{4.60}$$

As before, the two latter terms are zero due to the orthogonality of quantum-dot and wetting-layer states. The result can be summarized as follows,

$$M_S^{(3)} = \left\langle P_\mp(1)|e^{-i\mathbf{q}\cdot\mathbf{r}_1}|\mathbf{k}_1\right\rangle . \tag{4.61}$$

The matrix element, M, from Eq. (4.50), calculated in sections 4.3.4 to 4.3.6 for the three possible final states, is listed in Table 4.3. It involves single-particle states, so that the carrier capture rate can be calculated by slight modification to the rate of carrier capture into an empty dot state. Numerical results are shown in the next section.

4.3.7 Capture rates

Figure 4.10 (a) shows the capture rate of an electron into $|1P\rangle$ that is already occupied by another electron. The radius bands for capture into the three two-particle energy levels, listed in Figure 4.9, are slightly shifted

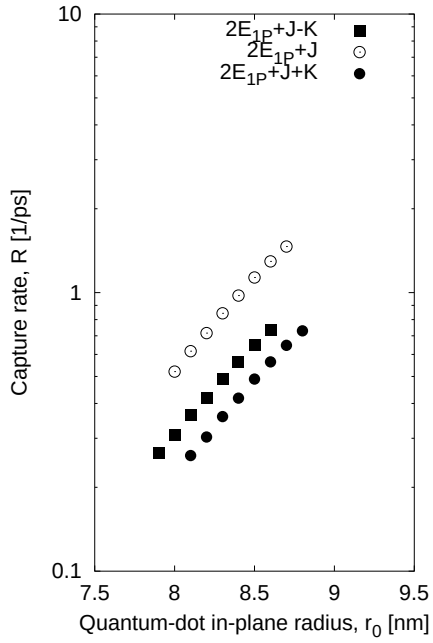

(a) Capture rate, $n_{2D} = 10^{15}\mathrm{m}^{-2}$.

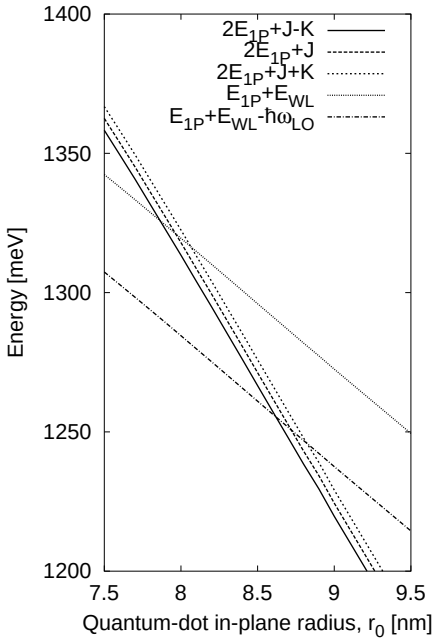

(b) Two-electron quantum-dot energy levels.

Figure 4.10: (a) Capture rate of an electron into $|1P\rangle$ that is occupied by an electron. (b) Two-electron energy levels. The lines $E_{1\mathrm{P}} + E_{\mathrm{WL}}$ and $E_{1\mathrm{P}} + E_{\mathrm{WL}} - \hbar\omega_{\mathrm{LO}}$ indicate the upper and lower limit of two-particle energies for which the capture process is energetically allowed. The intercept of the lines with energy levels gives the minimal and maximal radius of the radius band for each energy level. We have set $V_e = 697$ meV, $m_e = 0.07m_0$ and $\alpha = 12°$.

with respect to each other due to the non-negligible shift in energy that arises from their mutual Coulomb interaction. The radius band for the lowest energy level, $2E_{1\mathrm{P}} + J - K$, starts at the lowest radius and ends at a lower radius than bands for capture into the two higher lying levels. We will in the following show how the lower and upper limit for each radius band is determined. The lower limit is determined by the requirement that the two-particle complex is bound to the dot. We say that it is bound when it is energetically more favorable for two carriers to be in the dot than for one of the carriers to be in the continuum while the other carrier is in the dot. We denote the Coulomb shift by C. The total energy of the two-particle

state is then $2E_{1\mathrm{P}} + C$. The requirement for a bound state reads

$$2E_{1\mathrm{P}} + C < E_{1\mathrm{P}} + E_{\mathrm{WL}}. \tag{4.62}$$

The line $E_{1\mathrm{P}} + E_{\mathrm{WL}}$ is plotted in Figure 4.10 (b). The intercept of this line with the energy $2E_{1\mathrm{P}} + C$ gives the lower limit for the radius band in question. From the energy conservation requirement we get the upper limit for each radius band. We have that

$$E_{1\mathrm{P}} + C + \hbar\omega_{\mathrm{LO}} = E_{\mathrm{WL}} + \frac{\hbar^2 k^2}{2m_c}. \tag{4.63}$$

Hence,

$$2E_{1\mathrm{P}} + C \geq E_{1\mathrm{P}} + E_{\mathrm{WL}} - \hbar\omega_{\mathrm{LO}}. \tag{4.64}$$

The line $E_{1\mathrm{P}} + E_{\mathrm{WL}} - \hbar\omega_{\mathrm{LO}}$ is plotted in Figure 4.10 (b). The intercept of this line with energy level $2E_{1\mathrm{P}} + C$ gives the upper limit of each radius band. Figure 4.11 shows the same as Figure 4.10 but for holes. In general the capture rate is similar as for capture of electrons. The radius bands are somewhat larger due to the slower decrease of single-particle energy levels with r_0.

In this chapter we have calculated phonon-mediated carrier capture rates into quantum-dot states in which a carrier is already present. We have both investigated the effect where the incident carrier is different from the dot carrier and the cases where both carriers are identical. In the latter case the two-particle wave function is antisymmetric because the particles are indiscernable. The capture rates are very similar to rates into an empty dot. In the case of particles of the same type the radius intervals, for which single-phonon-mediated capture is allowed, are shifted due to Coulomb shifts but the radius bands are equally large as for capture into an empty dot state. In the case where the two particles are different the radius interval decreases when Coulomb interaction is taken into account. This is due to the strong attractive Coulomb force between two oppositely charged particles that are confined in space. The carrier capture rate is the same as if the carrier is captured into an empty dot except the energy level of the captured carrier looks as if it is shifted to lower energy due to the Coulomb interaction.

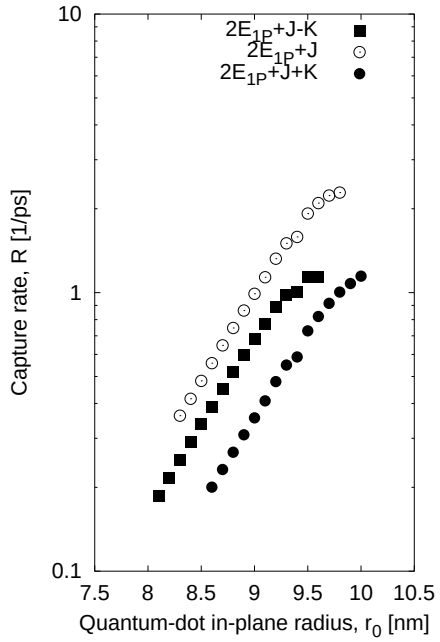

(a) Capture rate, $n_{2D} = 10^{15}\mathrm{m}^{-2}$.

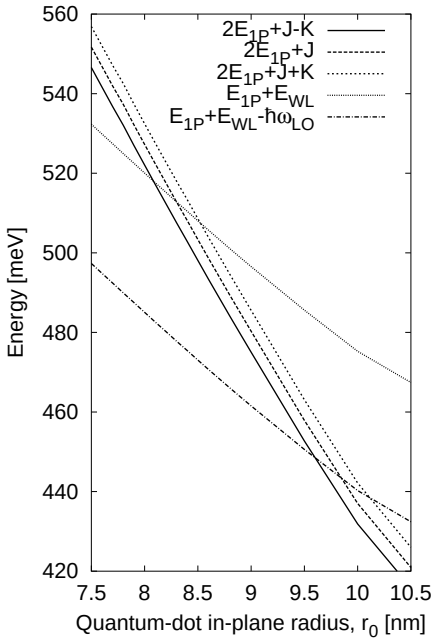

(b) Two-hole quantum-dot energy levels.

Figure 4.11: (a) Capture rate of a hole into $|1P\rangle$ that is occupied by a hole. The small decrease in the capture rate at $r_0 = 9.4$ nm arises from small uncertainties in the in-plane variational parameter β_P. (b) Two-hole energy levels. The lines $E_{1\mathrm{P}}+E_{\mathrm{WL}}$ and $E_{1\mathrm{P}}+E_{\mathrm{WL}}-\hbar\omega_{\mathrm{LO}}$ indicate the upper and lower limit of two-particle energies for which the capture process is energetically allowed. The intercept of the lines with energy levels gives the minimal and maximal radius of the radius band for each energy level. We have set $V_h = 288$ meV, $m_h = 0.34m_0$ and $\alpha = 12°$.

Chapter 5

Carrier-LO phonon interaction in quantum-dot states

In the preceding chapters we have investigated phonon-mediated carrier capture processes into quantum dots. To this end we have used a perturbative approach - Fermi's golden rule - to calculate the carrier capture rates. Early on in the investigation of carrier relaxation in quantum dots LO phonon-mediated relaxation processes were investigated by a direct extension of perturbative methods developed for bulk and quantum-well structures [31, 32, 33]. This lead to the conclusion that the relaxation was impossible unless the energy level separation was equal to the LO phonon energy [31, 32]. The so-called "phonon-bottleneck" was often mentioned in this context. Recently it has been shown both theoretically and experimentally [56, 57] that carriers in discrete quantum-dot states couple strongly to LO phonons and form polarons. This implies that the coupling of bound quantum-dot carriers to LO phonons cannot be treated in the frame of Fermi's golden rule and that the energy relaxation in quantum dots does not correspond to irreversible one-phonon processes. This arises due to the discretization of the electronic energy spectrum and the strong carrier-LO phonon interaction. The strong coupling regime is quite analogous to the coupled exciton-photon system - the polariton - in semiconductor microcavities [58] in which energy is periodically exchanged between exciton and photon modes, i. e. Rabi oscillations take place. An everlast-

ing Rabi oscillation takes place if both entities that form the particle in question - polaron or polariton - are stable. The quantum-dot polaron decays due to the finite lifetime of phonons, arising from phonon-phonon interactions [59, 60, 61, 62, 63]. Thus, the relaxation mechanism is not associated with carrier relaxation due to carrier-LO phonon coupling as in bulk and quantum well materials but rather with polaron relaxation due to phonon-phonon coupling. In calculations of phonon-mediated carrier capture rates the continuum wave functions have been considered to be plane waves (Refs. [21, 49] and chapters 3 and 4). Hence the influence of waves that are scattered by the quantum dot have been neglected. For certain quantum-dot sizes and wavelengths of the incident carrier the quantum dot can act as a Fabry-Perot mirror, in which the carrier can be imagined to "bounce" back and forth within the region of the quantum dot, giving rise to a long-lived carrier state of finite linewidth in the electronic continuum. An intriguing question arises as to whether carriers in such a *quasi-bound* state[1] interact with LO phonons within the strong or the weak-coupling regime. This is the question that we address in section 5.2. Before we go on to that the strong coupling of carriers in discrete quantum-dot states with LO phonons will be discussed.

5.1 Carriers in discrete quantum-dot states

In this section we discuss the influence of the Fröhlich interaction on carriers in bound quantum-dot states. The Hamiltonian for carriers and LO phonons is written as

$$H = H_e + H_{\rm ph} + V, \tag{5.1}$$

where H_e is the electronic Hamiltonian, $H_{\rm ph}$ the phonon Hamiltonian and V is the Fröhlich Hamiltonian for carrier-LO phonon coupling. $H_{\rm ph}$ and V are given by

$$\begin{aligned} H_{\rm ph} &= \sum_{\mathbf{q}} \hbar\omega_{\mathbf{q}} \hat{a}^{\dagger}_{\mathbf{q}} \hat{a}_{\mathbf{q}}, \\ V &= \sum_{\mathbf{q}} \left[\alpha(q) e^{-i\mathbf{q}\cdot\mathbf{r}} \hat{a}^{\dagger}_{\mathbf{q}} + \alpha^*(q) e^{i\mathbf{q}\cdot\mathbf{r}} \hat{a}_{\mathbf{q}} \right], \end{aligned} \tag{5.2}$$

[1] A state in the electronic energy continuum but with a finite linewidth unlike the discrete quantum-dot states.

where $\hbar\omega_{\mathbf{q}}$ is the phonon energy, $\hat{a}^{\dagger}_{\mathbf{q}}(\hat{a}_{\mathbf{q}})$ is the creation (annihilation) operator and the Fröhlich term, $\alpha(q)$, is defined in Eqs. (A.18) and (A.19). We restrict the discussion to $|S\rangle$ and $|P\rangle$, the lowest lying electronic states.[2] The dot is approximated by a cone as in chapter 4. We refer to $|S\rangle$ as the state with $m = 0$ and $|P\rangle$ is the state with $m = \pm 1$. We also limit ourselves to the lowest lying polaron states so only phonon states with *at most* one phonon per mode are taken into account. These phonon states are denoted as $|0_{\mathrm{ph}}\rangle$ and $|1_{\mathbf{q}}\rangle$. We limit our basis for the polaron states to the product states $|P, 0_{\mathrm{ph}}\rangle$ and $|S, 1_{\mathbf{q}}\rangle$, i. e. the zero-phonon P-level and one-phonon sideband of the S-level. These product states will be denoted as $|P, 0\rangle$ and $|S, 1_{\mathbf{q}}\rangle$ in the following. The polaron wave function is written as

$$|\Psi\rangle = a|P, 0\rangle + \sum_{\mathbf{q}} \beta_{\mathbf{q}}|S, 1_{\mathbf{q}}\rangle. \tag{5.3}$$

The diagonalization of H in the above basis leads to coupled eigenvalue equations

$$\begin{aligned} (E_P - E)a + \sum_{\mathbf{q}} \beta_{\mathbf{q}} v_{\mathbf{q}} &= 0 \\ (E_S + \hbar\omega_{\mathbf{q}} - E)\beta_{\mathbf{q}} + a v^{*}_{\mathbf{q}} &= 0, \end{aligned} \tag{5.4}$$

where we have defined $v_{\mathbf{q}} \equiv \langle 0, P\,|V|\,S, 1_{\mathbf{q}}\rangle$. In obtaining Eqs. (5.4) we have used that V fulfills

$$\langle 0, P|V|P, 0\rangle = 0 \qquad \langle 1_{\mathbf{q}}, S|V|S, 1_{\mathbf{q}'}\rangle = 0, \tag{5.5}$$

which is a consequence of the fact that V is linear in $\hat{a}_{\mathbf{q}}$ and $\hat{a}^{\dagger}_{\mathbf{q}}$. We approximate $\hbar\omega_{\mathbf{q}} \approx \hbar\omega_{\mathrm{LO}}$ which is a very good approximation as only phonons with the lowest $\mathbf{q}$ "participate" in the polaron [64] and the dispersion at the Γ-point is very flat. The LO-phonon dispersion is hence neglected. The solution $a = 0$ corresponds to continuum states that are uncoupled from the discrete state. The solution to the eigenvalue equations in (5.4) for non-zero a and $\beta_{\mathbf{q}}$ is given by

$$E_{\pm} = \frac{E_P + E_S + \hbar\omega_{\mathrm{LO}}}{2} \pm \sqrt{\left(\frac{E_P - (E_S + \hbar\omega_{\mathrm{LO}})}{2}\right)^2 + \sum_{\mathbf{q}} |v_{\mathbf{q}}|^2}. \tag{5.6}$$

[2] So far these states have been labeled $|1S\rangle$ and $|1P\rangle$ but we will abbreviate them as $|S\rangle$ and $|P\rangle$ for a less cumbersome notation.

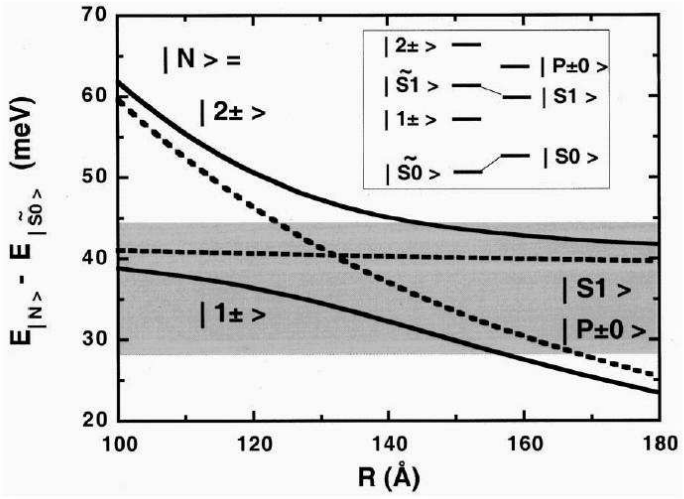

Figure 5.1: Polaron levels $|1_\pm\rangle$ and $|2_\pm\rangle$ versus quantum-dot in-plane radius. The dashed lines indicate the energy levels without the carrier-phonon coupling. These show the zero-phonon P state, $|P0\rangle$, and the one-phonon sideband of the S state, $|S1\rangle$. At the crossing of these levels the energy level separation is equal to the LO phonon energy and, due to the strong carrier-LO phonon coupling, the crossing is replaced by a large anticrossing. Here the height to radius ratio is held constant, $h/R = 12/80$ and the same quantum-dot model used as presented in section 4.1. Note that $|1\rangle$ and $|2\rangle$ are doubly degenerate due to the double degeneracy of $|P\rangle$, hence the "±" in the notation (these energy states are discussed in Appendix D). The shaded region is the energy interval where polarons can relax by disintegration of an LO phonon into two less energetic phonons. See discussion in text and in section 5.2. The inset of the figure shows the energy levels without the Fröhlich coupling (right) and with Fröhlich coupling (left). From Ref. [61].

$E_\pm - E_S$ is plotted in Fig. 5.1 as a function of the dot size.[3] Please note the different notation here from the rest of the thesis. R is here the in-plane dot radius, but we use R throughout this thesis as a rate (capture, relaxation, ...) with units s^{-1}. The dot in-plane radius (of a cone) is everywhere else denoted with r_0. At $E_P - (E_S + \hbar\omega_{\mathrm{LO}}) = 0$ ($R \approx 13.2$ nm) the levels $|P, 0\rangle$ and $|S, 1_{\mathbf{q}}\rangle$ cross. Due to the carrier-LO phonon coupling this crossing

[3]Please note that $E_\pm$ refers to polaron levels $|1\rangle$ (E_-) and $|2\rangle$ (E_+) in Fig. 5.1. The "±" here therefore *does not* refer to degeneracy of polaron levels, $|1_\pm\rangle$ and $|2_\pm\rangle$, as in Fig. 5.1.

is replaced by a large anticrossing with splitting $2\sqrt{\sum_{\mathbf{q}} |v_{\mathbf{q}}|^2} \approx 13$ meV. As R increases or decreases from this value, $E_{\pm}$ approach the uncoupled solutions. This is a case of a strong coupling regime; for an interval of dot sizes, there exist two solutions to Eqs. (5.4) for which $a \neq 0$. A similar conclusion as the one presented in Figure 5.1 is reached in Ref. [56]. By assuming LO phonons to be dispersionless corresponds to a coupling of a discrete state with continuum of zero width. For the interested reader a treatment of the weak and strong coupling regime for coupling between a discrete state and a continuum of finite and infinite extent can be found in [65] and [66] respectively.

We mentioned above that the polaron is not a stable entity due to the instability of phonons resulting from phonon-phonon interactions (anharmonicity of the crystal). The phonons are known to disintegrate into two less energetic phonons, in bulk into a less energetic LO phonon and a TA phonon. The phonon decay rate has been measured in bulk structures to be $\Gamma_{\mathrm{ph}} = 0.1$ ps^{-1} at low temperatures and 0.5 ps^{-1} at room temperature [67]. Lifetime of LO phonons in quantum dots has not been measured but it has been calculated to be very similar, $\sim$7 ps at low temperatures and $\sim$2.5 ps at room temperature [59]. A semiclassical approach is used by Li *et al.* in Ref. [60] to calculate the survival probability of the upper electronic level that is assumed to be populated at $t = 0$. A Wigner-Weisskopf coupled-mode-equation formalism is used, writing the total wave function as

$$|\Psi(t)\rangle = a(t)e^{-iE_e t}|\Psi_e; \{n_k\}\rangle + \sum_k b_k(t)e^{-iE_g t}|\Psi_g; \{(n+1)_k\}\rangle, \qquad (5.7)$$

and the initial condition $a(0) = 1$ and $b_k(0) = 0$ is imposed. Ψ_g and Ψ_e are the wave functions for the carrier ground and excited state, respectively. Figure 5.2, from Ref. [60], shows the resulting survival probability, $P(t) \equiv |a(t)|^2$, of the upper level as a function of time. The LO-phonon lifetime is assumed to be constant, $\tau_{\mathrm{LO}} = 2.5$ ps. $P(t)$ is shown for two different detunings $\Delta \equiv E_e - E_g - \hbar\omega_{\mathrm{LO}}$, E_g (E_e) being the energy of the ground (excited) electronic state. For zero detuning (Fig. 5.2 (a)) the relaxation time is just a few ps while at detuning "far" from zero ($\Delta = 8.23$ meV in Fig. 5.2 (b)) the relaxation time is somewhat longer. This result contradicts the relaxation time dictated by Fermi's golden rule. Relaxation would be impossible at non-zero detuning and the above results demonstrate once and again that the use of Fermi's golden rule to describe the

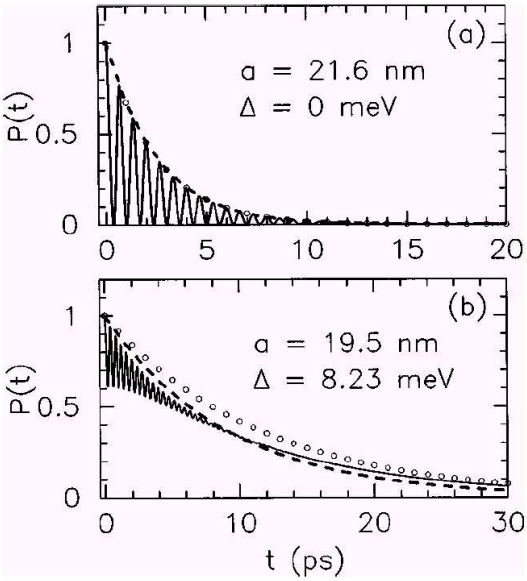

Figure 5.2: The survival probability $P(t) = |a(t)|^2$ (see text) for two different detunings, Δ. (a) $\Delta = 0$ and (b) $\Delta = 8.23$ meV. From Ref. [60].

carrier-LO phonon coupling for carriers in bound quantum-dot states is not correct. Polaron relaxation times are also investigated in Ref. [61], where a rate-equation model for polaron states is developed, Ref. [62] and polaron lifetimes are measured in Ref. [63]. The relaxation time measured in Ref. [63] is relatively long, ~ 40 ps at room temperature. This long relaxation time arises probably from a relatively large polaron level separation ~ 60 meV whereas the polaron level separation at zero detuning would probably be in the range 10-15 meV.

5.2 Carriers in quasi-bound quantum-dot states

The results presented in this section have also been outlined in Ref. [68]: I. Magnusdottir, A. V. Uskov, R. Ferreira, G. Bastard, J. Mørk, and B. Tromborg, *Influence of quasi-bound states on the carrier capture in quantum dots*, Appl. Phys. Lett. **81**, 4318 (2002).

For the case of carrier capture into quantum dots the electronic spec-

trum of the incident carrier is a relatively large continuum and in that case there is no way that bound states between delocalized carriers and delocalized phonons can be formed. We saw in the previous section that carriers in bound quantum-dot states couple strongly to LO phonons, leading to the formation of entities that are constituted of both carriers and phonons. The formation of polarons arises from the discretization of the electronic spectrum. As mentioned in the beginning of this chapter, for some combinations of quantum-dot size and wavelength of the incident carrier, the quantum dot can act as a Fabry-Perot mirror leading to the formation of a *quasi-bound* state in the continuum but with a finite width resembling in many ways the bound quantum-dot states. Quasi-bound quantum-well states have been investigated theoretically [69] and observed experimentally [70]. The influence of quasi-bound states on carrier capture rates into quantum wells has revealed strong oscillations versus the quantum-well thickness [26].

The question that we address in this section is whether polarons *can* be formed for carriers in quasi-bound quantum-dot states because if that is the case we cannot use Fermi's golden rule to calculate phonon-mediated carrier capture rates into the quantum dot. We shall see that polarons are indeed formed for level separation of the quasi-bound state from a quantum-dot state close to the LO phonon energy. In section 5.1 we investigated the coupling of a discrete $|P\rangle$ state with a continuum of phonons. Here we shall investigate the coupling of a "P-like" quasi-bound state with the phonon continuum. It is P-like in the sense that if the quantum dot gets larger, this quasi-bound state will become a bound $|P\rangle$ state. We hence assume that one level is bound to the dot, i. e. $|S\rangle$. In this section we approximate the quantum dot by a *sphere* with finite confinement potential walls in the effective-mass approximation (Appendix C). With this approximation, the quasi-bound states are relatively easy to calculate (see Appendix G.1).

We limit our basis here to the product states $|\nu, 0_{\mathrm{ph}}\rangle$ and $|S, 1_{\mathbf{q}}\rangle$, i. e. the zero-phonon P-like level and one-phonon sideband of the S-level. The ground state $|S, 0\rangle$ is not taken into account in the calculation, because the Fröhlich interaction merely results in a small shift of the S level [61]. The electronic continuum, $|\nu\rangle$, is characterized by the quantum numbers k, ℓ, m, i. e. the wavenumber, the angular momentum quantum number and the projection onto the quantization axis, respectively. We shall set $\ell = 1$ later but the following derivation is independent of that. The total

wavefunction is now written as

$$|\Psi\rangle = \sum_{\nu} a_{\nu}|\nu, 0\rangle + \sum_{\mathbf{q}} \beta_{\mathbf{q}}|S, 1_{\mathbf{q}}\rangle. \tag{5.8}$$

By comparing Eq. (5.8) with Eq. (5.3) it is seen that in the case of quasi-bound quantum-dot states $|\Psi\rangle$ includes a sum over the electronic continuum, represented by a sum over ν, reflecting the fact that the quasi-bound state is a state of finite width while the bound quantum-dot state is assumed to have zero width (no additional broadening mechanisms are taken into consideration). As before we have that

$$\langle 1_{\mathbf{q}'}, S|V|S, 1_{\mathbf{q}}\rangle = 0 \qquad\qquad \langle 0, \nu|V|\nu', 0\rangle = 0. \tag{5.9}$$

The diagonalization of H in the basis $\{|\nu, 0\rangle\}$, $\{|S, 1_{\mathbf{q}}\rangle\}$ leads to a set of coupled eigenvalue equations,

$$\begin{aligned} a_{\nu}(E_{\nu} - E) + \sum_{\mathbf{q}} \beta_{\mathbf{q}} u_{\nu\mathbf{q}} &= 0 \\ \beta_{\mathbf{q}}(E_S + \hbar\omega_{\mathbf{q}} - E) + \sum_{\nu} a_{\nu} u_{\mathbf{q}\nu} &= 0, \end{aligned} \tag{5.10}$$

where

$$\begin{aligned} u_{\mathbf{q}\nu} &\equiv \langle 1_{\mathbf{q}}, S\,|V|\,\nu, 0\rangle \\ &= \alpha(q)\langle S\,\left|e^{-i\mathbf{q}\cdot\mathbf{r}}\right|\,\nu\rangle. \end{aligned} \tag{5.11}$$

The electronic continuum is discretized by enclosing the quantum dot in a large sphere of radius R_b. The practical aspects of the discretization of electron and phonon modes and the diagonalization procedure are outlined in Appendix G. The position in energy of a quasi-bound state can be traced by a local increase in the probability that the carrier is present within the quantum-dot volume, given by

$$\begin{aligned} P_a &= \int_{r\le a} d^3r|\Psi_{\nu}(\mathbf{r})|^2 \\ &= \int_0^a dr r^2 |R_{\ell}(r)|^2. \end{aligned} \tag{5.12}$$

This is the probability of presence *before* the carrier-phonon interaction is taken into account. The continuum wave function, R_{ℓ}, is given in Appendix G.1. This probability is shown in Figure 5.3 (a) for an electron with

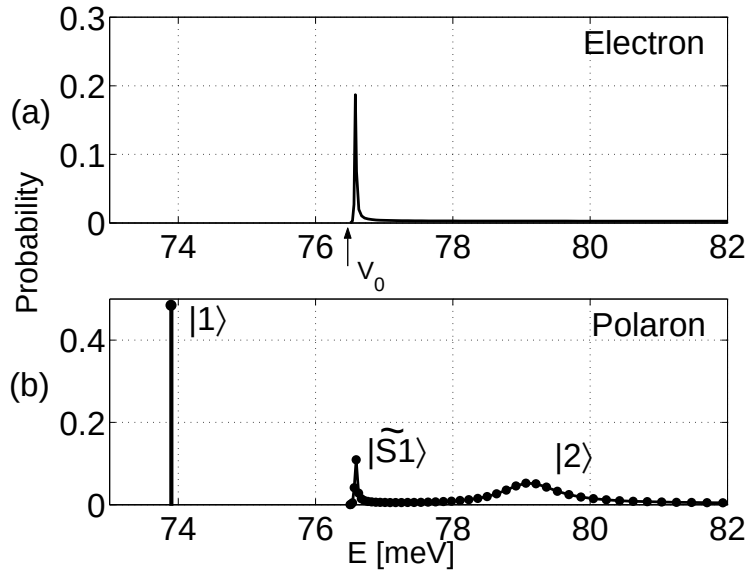

Figure 5.3: (a) The probability that an electron state with $\ell = 1$ in the continuous part of the energy spectrum is present within the volume of the quantum dot, neglecting the carrier-LO phonon interaction. A quasi-bound state is situated at $E_1 = 76.58$ meV with a FWHM $\hbar\Gamma_e = 0.025$ meV. The discrete $\ell = 0$ state (not shown) is situated at $E = 41.59$ meV, $\hbar\omega_{\rm LO}$ below the quasi-bound state. (b) Taking carrier-LO phonon interaction into account, two polaron states ($|1\rangle$, $|2\rangle$) appear. One, $|1\rangle$, is discrete and at $E_0 = 73.9$ meV. $|2\rangle$ is a broader level centered at $E = 79.1$ meV and the Rabi splitting is $E_{\rm Rabi} = 5.2$ meV. We use $a = 8.55$ nm, the carrier mass $m^* = 0.067m_0$, $V_0 = 76.49$ meV and $R_b = 1500$ nm.

$\ell = 1$. $E = 0$ is set at the bottom of the quantum-dot potential well. V_0 and a are chosen such that a narrow resonance appears at $E_1 = 76.58$ meV, one LO phonon energy, $\hbar\omega_{\rm LO}(= 35$ meV), above the discrete quantum-dot state. The diagonalization of the total Hamiltonian couples a few of the phonon modes to the electron states leaving a large amount of the phonon bath "intact". The coupled electron-phonon states form the polaron states. Figure 5.3 (b) shows the probability of presence within the quantum-dot

volume for the polarons. This probability is given by

$$\begin{aligned} P_a^{\mathrm{pol}} &= \int_{r\leq a} d^3r |\langle\Psi|\Psi\rangle|^2 \\ &= \sum_\nu |a_\nu|^2 P_a + \sum_{\mathbf{q}} |\beta_{\mathbf{q}}|^2 P_S, \end{aligned} \tag{5.13}$$

where $P_S = \int_0^a dr r^2 |R_0(r)|^2$ is the probability for the bound $|S\rangle$ state. To obtain P_a^{pol} we integrate over phonon modes in all space to be able to compare with Eq. (5.12). We do not show pure phonon modes in Figure 5.3 (b), we only show modes with nonzero projection onto the states $|\nu, 0_{\mathrm{ph}}\rangle$. The energy levels of the total Hamiltonian, that are plotted in Figure 5.3 (b), are determined in the diagonalization that is outlined in Appendix G.2. These are different from the energy levels that allowed us to plot Figure 5.3 (a). The energies in Figure 5.3 (a) are in fact given by $E_\nu = \hbar^2\kappa_\nu^2/(2m^*)$, where κ_ν is the wavenumber of the carrier inside the quantum-dot region. Figure 5.3 (b) shows that two polaron states are formed when the carrier-LO phonon interaction is taken into account. These are labeled $|1\rangle$ and $|2\rangle$ as in Ref. [61]. The Rabi splitting between $|1\rangle$ and $|2\rangle$ is given by $E_{\mathrm{Rabi}} = 5.2$ meV, giving a measure of the Fröhlich coupling strength. The lifetime of both the constituents of the polaron, i. e. electrons and phonons, must be much larger than half the Rabi oscillation period. Otherwise, the Rabi oscillation is destroyed, and there is no chance for the polaron to be formed. Equivalently, we require that $E_{\mathrm{Rabi}} >> \hbar\Gamma_{\mathrm{ph}}, \hbar\Gamma_e$, where $\hbar\Gamma_{\mathrm{ph}}, \hbar\Gamma_e$ are the phonon and electron linewidths, respectively. The electron linewidth is $\hbar\Gamma_e = 0.025$ meV and the phonon linewidth is not larger than about 0.3 meV (taking the room temperature phonon dephasing rate, i. e. $\Gamma_{\mathrm{ph}} = 0.5$ ps^{-1}), so the condition is fulfilled here. As an important result, we find that $|1\rangle$ corresponds to a discrete state confined to the quantum dot with a probability close to 50%, while the probability for the electronic state $|S\rangle$ is about 80%.

A reminescence of the quasi-bound state is seen between $|1\rangle$ and $|2\rangle$, labeled $|\widetilde{S1}\rangle$, recognised by a finite linewidth and the same shape as the electronic quasi-bound state. The results in Figure 5.3 can be shown to be independent of the azimuthal quantum number, m, so the polaron states are triply degenerate due to the $(2\ell+1)$-degeneracy of the carrier quasi-bound state. This is shown in Appendix G.2.

Figure 5.4 (a) shows the probability for a hole quasi-bound state that is about a 100 times broader than the electron resonance. Figure 5.4 (b) shows

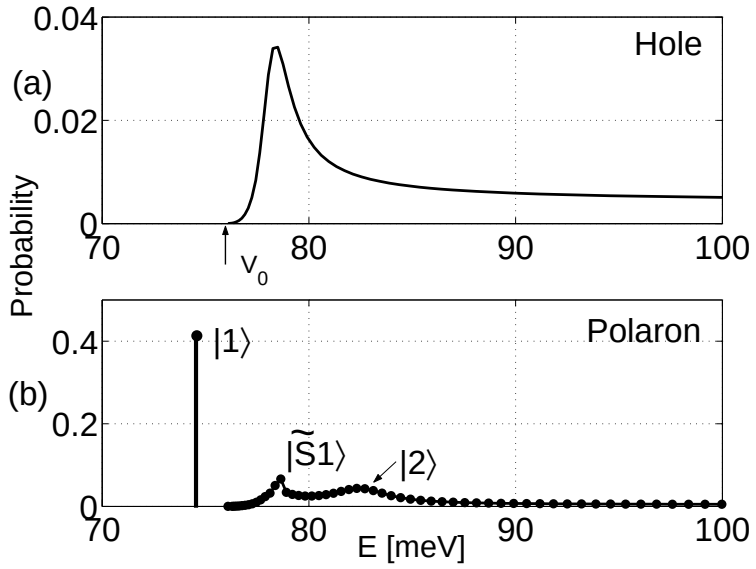

Figure 5.4: As Figure 5.3 but for holes. The quasi-bound state seen in (a) when carrier-LO phonon interaction is neglected is broad compared to the case for electrons. It is situated at $E_1 = 78.34$ meV with $\hbar\Gamma_h = 2.1$ meV. The discrete $\ell = 0$ state (not shown) is situated at $E_0 = 43.5$ meV, $\hbar\omega_{\rm LO}$ below the quasi-bound state. The polaron states appearing when the interaction is taken into account (b) contain a discrete level, $|1\rangle$, at $E = 74.6$ meV. The state $|2\rangle$ is centered at $E = 82.3$ meV, so the Rabi splitting is $E_{\rm Rabi} = 7.7$ meV. The quantum-dot radius is $a = 3.662$ nm, the carrier mass $m^* = 0.34m_0$, $V_0 = 76.0$ meV and $R_b = 400$ nm.

the probability when the Fröhlich interaction has been taken into account. Here, polarons are also formed. We obtain a Rabi splitting $E_{\rm Rabi} = 7.7$ meV which fulfills again $E_{\rm Rabi} >> \hbar\Gamma_h, \hbar\Gamma_{\rm ph}$.

We stress here that within the strong coupling regime, it is no longer possible to use the notion of phonon absorption/emission. The relaxation of a polaron as a whole can nevertheless take place, due to an anharmonic decay of its phonon part. It is known in bulk structures that LO phonons disintegrate into two less energetic phonons. The decay frequency has been measured in a GaAs bulk structure to be $\Gamma_{\rm ph} = 0.1$ ps^{-1} at low temperatures and 0.5 ps^{-1} at room temperature [67]. The phonon decay has not been measured in quantum dots but the lifetime of confined LO phonons in quantum dots has been calculated to be of the same order [59]. In a

relaxation process from $|1\rangle$ to $|S0\rangle$ we have that

$$E_{|1\rangle} - E_{|S0\rangle} = E_{\mathrm{LO}} + E_{\mathrm{TA}}, \tag{5.14}$$

if the relaxation arises from disintegration into an LO and a transverse acoustic (TA) phonon. This relaxation path is measured to be dominant in bulk structures [67].[4] This relaxation process *does not* require the electronic levels to be separated by one LO phonon, since it concerns relaxation of the polaron as a whole, due to phonon-phonon interaction on polaron states. We note here that due to the translational symmetry breaking in quantum-dot structures, there are no specific crystal momentum conservation requirements. Hence, the wavevectors of the LO and TA phonons are not restricted to specific values. Note also that the dispersion of LO phonons needs to be considered in order to fulfill the energy conservation requirement in Eq. (5.14). $(E_{|1\rangle} - E_{|S0\rangle})$ is just below $\hbar\omega_{\mathrm{LO}}$ (at the Γ point), so if $\hbar\omega_{\mathrm{LO}}$ is constant, there is no way that the energy conservation can be fulfilled. The LO phonon energy decreases from about 36 meV at the Γ point to about 28 meV at the border of the Brillouin zone, while the TA phonon energy increases from 0 to 8 meV. The energy conservation requirement can therefore be fulfilled by taking the phonon dispersion into account.

We will in the following estimate the relaxation rate for polaron level $|1\rangle$. The relaxation rate of a $|1\rangle$ state can be calculated by weighting Γ_{ph} by the phonon part of the total probability $\langle\Psi|\Psi\rangle$,

$$R_{|1\rangle} = \Gamma_{\mathrm{ph}} \sum_{\mathbf{q}} |\beta_{\mathbf{q}}|^2 \tag{5.15}$$

This yields relaxation times for both electron and hole polarons of about 4 ps at $T = 300$ K (20 ps at low temperatures).

Finally, we investigate the dot size dependence of the polaron formation. The left panel of Figure 5.5 shows the radius dependence of polaron levels $|1\rangle$ and $|2\rangle$ for an electron as in Figure 5.3. The polaron levels $|1\rangle$ and $|2\rangle$ are seen down to $a = 7.7$ nm but for a smaller radius the polaron levels are too broad to be distinguished. This arises because the quasi-bound state

[4] It is mentioned in Ref. [62] that relaxation through disintegration of an LO phonon into an LO and an LA phonon might be enhanced in comparison to the LO-TA channel but the LO-LA channel is measured to be negligible in bulk structures [67].

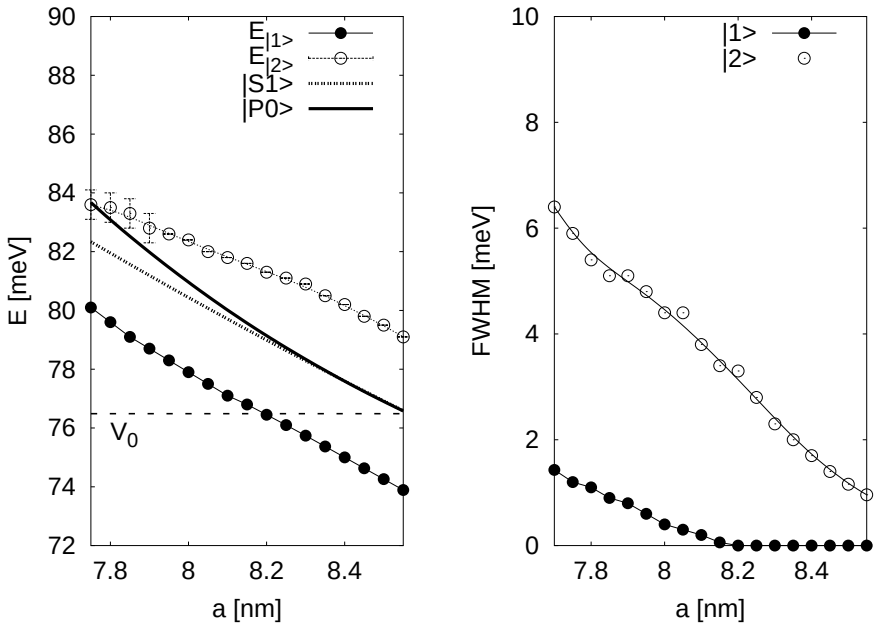

Figure 5.5: The left panel shows the energy position of the polaron states $|1\rangle$ and $|2\rangle$ as a function of quantum-dot radius along with the zero-phonon quasi-bound level peak ($|P0\rangle$) and the one-phonon sideband of the S level ($|S0\rangle$). The horizontal line shows the onset of the continuum (i. e. the barrier position). The parameters are the same as in Figure 5.3. The polaron levels $|1\rangle$ and $|2\rangle$ are observable down to $a = 7.7$ nm. The quasi-bound state broadens as its energy increases (the dot size decreases) and hence, the polaron levels also broaden. The linewidth (FWHM) of levels $|1\rangle$ and $|2\rangle$ is shown in the right panel for the same radius interval.

broadens as its energy increases (the dot size decreases), since at higher energies, the incident carrier "feels" less the presence of the confinement potential. Hence, the polaron levels broaden as well. This is shown in the right panel of Figure 5.5, where the linewidth (FWHM) is given for the same radius interval. At $a = 8.6$ nm, the quasi-bound level becomes a bound quantum-dot $|P\rangle$ state as discussed earlier in this chapter. At $a = 8.2$ nm, the polaron level $|1\rangle$ becomes bound. This is shown by the zero linewidth of polaron level $|1\rangle$ in the right panel beyond 8.2 nm.

In all calculations presented in this section, we have neglected the influ-

ence of carrier-carrier interaction on linewidths of quasi-bound states. For instance, under optical excitation, a large amount of carriers exist in the vicinity of the dots and charge fluctuations might increase the linewidth. Furthermore, effects of thermal broadening have not been taken into account. Dephasing times of excited states have been measured in self-assembled quantum dots in a four-wave mixing experiment to be around 60 ps at 5 K, compared to a ground-state dephasing time of 372 ps [71]. Nothing has been reported so far on dephasing times of quasi-bound states.

5.3 Summary

In this chapter we have investigated the strong-coupling regime of carriers and LO phonons. The strong carrier-phonon coupling was reviewed for carriers in bound quantum-dot states in section 5.1 where polaron formation and relaxation was discussed. The discussion was extended to include carriers in quasi-bound states in section 5.2. It was shown that carriers in quasi-bound states *can* enter a strong-coupling regime if the quasi-bound level is separated $\approx \hbar\omega_{\mathrm{LO}}$ from the bound S-level. Carriers in quasi-bound states are expected to couple strongly with phonons whenever the level is separated by $\approx \hbar\omega_{\mathrm{LO}}$ from a bound energy level, not only the S-level. The polaron levels broaden very quickly as the energy separation increases by a few meV from $\hbar\omega_{\mathrm{LO}}$. When the energy separation decreases the quasi-bound level becomes bound to the dot. The fast broadening of polaron levels with increasing energy separation indicates that except for isolated cases a standard perturbative approach - Fermi's golden rule - can be used to calculate phonon-mediated capture rates into quantum dots.

In this chapter and the preceding ones (chapters 3 and 4), we have investigated scattering mechanisms by interaction of carriers with LO phonons. Carrier-carrier scattering will be the focus of the next chapter, where carrier capture and a transport mechanism will be investigated.

Chapter 6

Auger processes

In an Auger process two carriers interact by Coulomb interaction leading to the relaxation of one of the carriers and excitation of the other. In semiconductor lasers, such non-radiative processes can lead to the dissipation of energy as heat instead of useful photons, and should thus be minimized if possible [10]. Carrier capture in nanostructures, such as quantum wells [28, 29] and quantum dots [34, 38], can also be mediated by Auger processes. For instance, it has been shown that Auger and phonon-mediated capture processes into quantum wells are equally important [72]. A pioneering paper by U. Bockelmann and T. Egeler suggested that the so-called "phonon-bottleneck" in quantum dots could be overcome by means of Auger relaxation processes [34]. Since then, capture and relaxation processes have been studied extensively, both experimentally [73, 74, 75, 76, 77, 48] and theoretically [21, 36, 38, 39, 78]. In this chapter we will investigate the geometry dependence of Auger capture rates. This is the first detailed analysis of the geometry dependence. It was initiated by A. V. Uskov who presented with his co-workers a simple model of Auger capture in Ref. [38]. We will also investigate a transport process, mediated by carrier-carrier scattering.

6.1 Auger capture

There are a number of possible Auger process that can lead to carrier capture into quantum dots. Fig. 6.1 illustrates schematically an Auger capture process in which two wetting-layer carriers interact leading to the capture of one of the carriers while the other carrier is promoted higher up in energy in the wetting layer. Fig. 6.1 shows two examples of such processes. On the

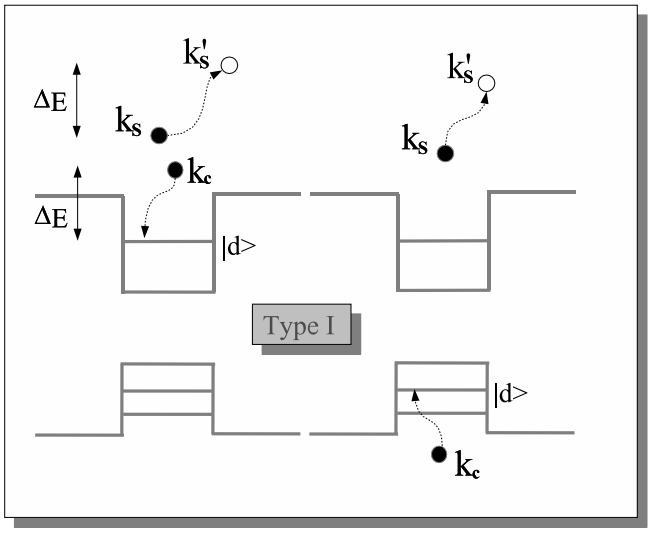

Figure 6.1: Auger capture process of type I. Two wetting-layer carriers, characterized by the wavevectors $\mathbf{k}_c$ and $\mathbf{k}_s$, interact. Carrier "c" is captured by the dot into the level $|d\rangle$ and carrier "s" is promoted to a higher energy in the wetting layer.

left hand side scattering of two electrons is shown and on the right hand side scattering of an electron and a hole leads to capture of the hole. This type of process will hereafter be referred to as a "type I" process. Fig. 6.2 illustrates a different kind of process where a carrier is captured by the dot while a previously captured carrier is either excited to a higher lying dot state or out of the dot into the wetting layer. These processes are referred to as "type II" processes. On the left hand side of Fig. 6.2, an electron is captured while exciting a hole in the ground state to the first excited hole state. On the right hand side, a hole is captured while a previously captured electron is excited out of the dot to the wetting layer. This latter process has been investigated in Ref [38], where capture times close to 1 ps were calculated for carrier sheet density in the wetting layer of $n_{2\mathrm{D}} = 10^{15}$ m^{-2}, but only for a small interval of dot sizes. Note that this last process

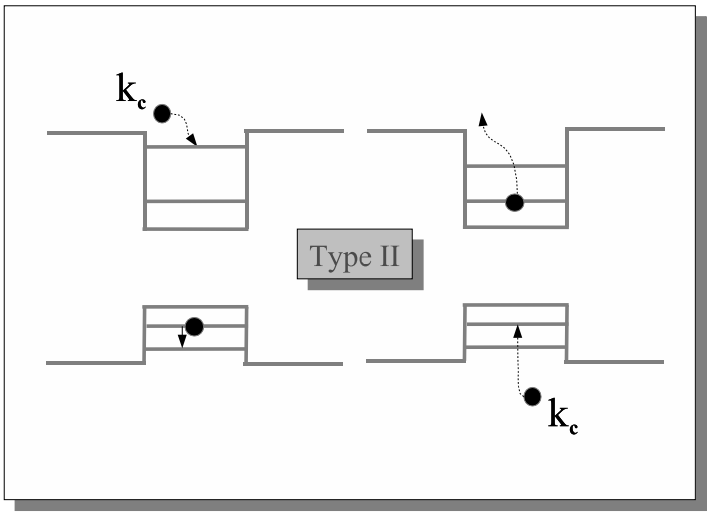

Figure 6.2: Auger capture processes of type II. The left hand side shows capture of an electron while promoting a previously captured hole from the ground state to an excited hole state. In the right hand side a hole is captured while a previously captured electron is excited from the dot into the wetting layer.

is a combination of capture and escape. In all these processes, the total energy should be conserved. This is illustrated in the left hand side of Fig. 6.1; the energy that the captured carrier "loses", ΔE, is transferred to the scattered carrier "s".

In this section we will focus on capture processes of type I. The carrier capture rate, i. e., the rate of carriers making a transition from the wetting layer to the quantum-dot bound state, is determined by Fermi's golden rule,

$$R = \frac{2\pi}{\hbar} \sum_{\substack{\text{spin} \\ \text{config}}} \sum_{\mathbf{k}_s} \sum_{\mathbf{k}'_s} \sum_{\mathbf{k}_c} |\langle f\,|V_c|\,i\rangle|^2 f(\epsilon_{k_s}) f(\epsilon_{k_c})(1 - f(\epsilon_{k'_s}))\delta(E_f - E_i), \tag{6.1}$$

where $\mathbf{k}_s$ and $\mathbf{k}_c$ are wavevectors characterizing the scattered and captured carrier initial states, respectively, and $\mathbf{k}'_s$ denotes the final state of the scattered carrier. $|i\rangle$ and $|f\rangle$ are the initial and final two-particle states, respec-

tively, E_i and E_f are the corresponding energies. We write the Coulomb interaction potential as a statically screened potential

$$V_c(r) = \frac{e^2 \exp(-\kappa_s r)}{4\pi\epsilon_r\epsilon_0 r}, \tag{6.2}$$

where ϵ_r is the dielectric constant, ϵ_0 is the permittivity constant and κ_s is the screening wavenumber or inverse *screening length*. The screening wavenumber can be determined in the random phase approximation, which is a mean-field approximation for the carrier density. In the Debye-Hückel model, where the distribution function is expressed by the Boltzmann approximation, it is given by [50]

$$\kappa_s = \sqrt{\frac{4\pi e^2 n}{\epsilon_0 k_B T}}, \tag{6.3}$$

where n is the three-dimensional carrier density.

We will express the Coulomb interaction by a two-dimensional Fourier transform because, as we shall see, it will yield Coulomb matrix elements that are separable in z- and in-plane coordinates. This is because we use the variational wave functions for a cone (Appendix D) that are approximated by separable functions in in-plane and z variables. We start out by calculating the three-dimensional Fourier transform of the screened Coulomb interaction. It will allow us to write the Coulomb interaction in terms of the inverse Fourier transform and from there, the two-dimensional Fourier transform can be expressed. The three-dimensional Fourier transform of $V_c(r)$ is given by

$$\begin{aligned} V_c(\boldsymbol{\beta}) &= \frac{e^2}{4\pi\epsilon_r\epsilon_0}\int d^3r \frac{e^{i\boldsymbol{\beta}\cdot\mathbf{r}}}{r} e^{-\kappa_s r} \\ &= \frac{e^2}{4\pi\epsilon_r\epsilon_0}\int_0^{+\infty} dr r e^{-\kappa_s r}\int_0^{2\pi} d\phi \int_0^{\pi} d\theta \sin\theta e^{i\beta r\cos\theta} \\ &= \frac{e^2}{4\pi\epsilon_r\epsilon_0}\frac{2\pi}{i\beta}\int_0^{+\infty} dr e^{-\kappa_s r}(e^{i\beta r} - e^{-i\beta r}) \\ &= \frac{e^2}{\epsilon_r\epsilon_0}\frac{1}{\beta^2+\kappa_s^2}. \end{aligned} \tag{6.4}$$

The Coulomb interaction can therefore be expressed in terms of the inverse

Fourier transform of $V_c(\boldsymbol{\beta})$,

$$\begin{aligned} V_c(r) &= \frac{1}{(2\pi)^3}\int d^3\beta e^{-i\boldsymbol{\beta}\cdot\mathbf{r}} V_c(\boldsymbol{\beta}) \\ &= \frac{e^2}{\epsilon_r\epsilon_0}\frac{1}{(2\pi)^3}\int d^3\beta \frac{e^{-i\boldsymbol{\beta}\cdot\mathbf{r}}}{\beta^2+\kappa_s^2}. \end{aligned} \tag{6.5}$$

We write $\boldsymbol{\beta}$ in terms of its in-plane and z component as $\boldsymbol{\beta} = (\boldsymbol{\beta}_\perp, \beta_z)$ and write furthermore $\mathbf{r} = (\boldsymbol{\rho}, z)$. We then integrate over β_z [given in Eq. (4.16)],

$$\begin{aligned} V_c(r) &= \frac{e^2}{\epsilon_r\epsilon_0}\frac{1}{(2\pi)^3}\int d^2\beta_\perp e^{-i\boldsymbol{\beta}_\perp\cdot\boldsymbol{\rho}}\int_{-\infty}^{+\infty} d\beta_z \frac{e^{-i\beta_z z}}{\beta_z^2+\beta_\perp^2+\kappa_s^2} \\ &= \frac{e^2}{\epsilon_r\epsilon_0}\frac{1}{(2\pi)^3}\pi\int d^2\beta_\perp \frac{e^{-i\boldsymbol{\beta}_\perp\cdot\boldsymbol{\rho}}}{\sqrt{\beta_\perp^2+\kappa_s^2}} e^{-\sqrt{\beta_\perp^2+\kappa_s^2}z} \\ &= \frac{e^2}{2\epsilon_r\epsilon_0}\frac{1}{S}\sum_{\boldsymbol{\beta}_\perp}\frac{e^{-i\boldsymbol{\beta}_\perp\cdot\boldsymbol{\rho}}}{\sqrt{\beta_\perp^2+\kappa_s^2}} e^{-\sqrt{\beta_\perp^2+\kappa_s^2}|z|}. \end{aligned} \tag{6.6}$$

In the last step, we have transformed the integral over $\boldsymbol{\beta}_\perp$ into a sum by

$$\int d^2\beta_\perp \longrightarrow \frac{(2\pi)^2}{S}\sum_{\boldsymbol{\beta}_\perp}, \tag{6.7}$$

where S is a (macroscopic) surface of the wetting layer to which the wetting-layer wave functions are normalized. The transformation from an integral to a sum is only for convenience sake, that will come clear later in this section.

In general, screening of Coulomb interactions in quantum-dot structures is a complicated issue. A test charge induces a change in the carrier-density distribution, which then influences the test charge and the surroundings. Therefore such interactions "bite in their tail" so to speak. Furthermore, the wetting-layer is very thin, and it is therefore not certain whether to use 3D or 2D screening or something in between. As a very first approximation, we have decided not to include any screening in the following calculations, i. e., we set $\kappa_s = 0$. This is partly motivated by the results obtained by Bockelmann and Egeler [34], where intra-dot relaxation rates

Spin state	Initial orbital state	Final orbital state
$\frac{\lvert\uparrow\downarrow\rangle - \lvert\downarrow\uparrow\rangle}{\sqrt{2}}$	$\frac{\lvert\mathbf{k}_c(1)\rangle\lvert\mathbf{k}_s(2)\rangle + \lvert\mathbf{k}_s(1)\rangle\lvert\mathbf{k}_c(2)\rangle}{\sqrt{2}}$	$\frac{\lvert\mathbf{k}'_s(1)\rangle\lvert d(2)\rangle + \lvert d(1)\rangle\lvert\mathbf{k}'_s(2)\rangle}{\sqrt{2}}$
$\frac{\lvert\uparrow\downarrow\rangle + \lvert\downarrow\uparrow\rangle}{\sqrt{2}}$, $\lvert\uparrow\uparrow\rangle$, $\lvert\downarrow\downarrow\rangle$	$\frac{\lvert\mathbf{k}_c(1)\rangle\lvert\mathbf{k}_s(2)\rangle - \lvert\mathbf{k}_s(1)\rangle\lvert\mathbf{k}_c(2)\rangle}{\sqrt{2}}$	$\frac{\lvert\mathbf{k}'_s(1)\rangle\lvert d(2)\rangle - \lvert d(1)\rangle\lvert\mathbf{k}'_s(2)\rangle}{\sqrt{2}}$

Table 6.1: The possible two-particle initial and final states for the capture process of type I. The spin states are a singlet (upper) and triplet (lower). The spin state does not change in the transition.

for smaller dots (base length < 40 nm) are the same whether one uses the unscreened interaction or a dynamical screening of the two-dimensional electron gas. Inclusion of screening should be the subject of future investigations of Coulomb-mediated capture processes.

In the case of $\kappa_s = 0$ the Coulomb interaction can be written as

$$V_c(r) = \frac{e^2}{2\epsilon_r\epsilon_0}\frac{1}{S}\sum_{\boldsymbol{\beta}_\perp}\frac{e^{-i\boldsymbol{\beta}_\perp\cdot\boldsymbol{\rho}}}{\beta_\perp}e^{-\beta_\perp|z|}, \tag{6.8}$$

i. e., a two-dimensional Fourier transform. In the case where the two particles are identical (two electrons or two holes) the wave function needs to be antisymmetric. Similar to the results in Table 4.1 we have two states where the spins are aligned and other two where the spins have opposite directions. We have a singlet state with total spin $S = 0$ for which the orbital state is symmetric. The triplet state ($S = -1, 0, 1$) has an antisymmetric orbital state. The possible initial and final spin and orbital states are listed in Table 6.1. The spin state does not change in the transition because the interaction potential is a Coulomb potential. We can therefore determine the Coulomb matrix element, $\langle f|V_c|i\rangle$.

For the triplet state we have that

$$\begin{aligned}\langle f|V_c|i\rangle = \frac{1}{2}\Big[&\langle \mathbf{k}_s'(1)|\langle d(2)|V_c|\mathbf{k}_c(1)\rangle|\mathbf{k}_s(2)\rangle \\ &-\langle d(1)|\langle \mathbf{k}_s'(2)|V_c|\mathbf{k}_c(1)\rangle|\mathbf{k}_s(2)\rangle \\ &-\langle \mathbf{k}_s'(1)|\langle d(2)|V_c|\mathbf{k}_s(1)\rangle|\mathbf{k}_c(2)\rangle \\ &+\langle d(1)|\langle \mathbf{k}_s'(2)|V_c|\mathbf{k}_s(1)\rangle|\mathbf{k}_c(2)\rangle\Big] \\ = K-J,&\end{aligned} \tag{6.9}$$

where we have defined the direct (J) and exchange (K) Coulomb integrals,

$$\begin{aligned}J &= \langle d(1)|\langle \mathbf{k}_s'(2)|V_c|\mathbf{k}_c(1)\rangle|\mathbf{k}_s(2)\rangle, \\ K &= \langle \mathbf{k}_s'(1)|\langle d(2)|V_c|\mathbf{k}_c(1)\rangle|\mathbf{k}_s(2)\rangle.\end{aligned} \tag{6.10}$$

Note here that the notation $\mathbf{k}_c$ and $\mathbf{k}_s$ for the captured and scattered carrier, respectively, does not apply to the exchange Coulomb integral because of the interchange of variables. In reality one cannot identify the carrier that is captured or the carrier that is scattered due to the indiscernability of the particles. However, in the following we will show that the capture rate can be expressed in terms of the direct Coulomb integral only. In the direct Coulomb integral, it is possible to label the carriers as 'captured' or 'scattered'. We will therefore continue to do so in the following.

For the singlet state we get

$$\langle f|V_c|i\rangle = J + K. \tag{6.11}$$

Inserted into Fermi's golden rule the sum over possible spin configurations occurs. This corresponds to the sum

$$3|K-J|^2 + |K+J|^2 = 4(|J|^2 + |K|^2 - \Re(J^*K)).$$

It can be shown that the contribution from $|J|^2$ and $|K|^2$ gives the same contribution to the capture rate. The difference between the two terms is that $\mathbf{k}_c$ and $\mathbf{k}_s$ are interchanged and the sums over $\mathbf{k}_c$ and $\mathbf{k}_s$ in Eq. (6.1) are equivalent. Hence, a simple interchange of $\mathbf{k}_c$ and $\mathbf{k}_s$ in one of the sums shows that the two sums are equivalent. We neglect the interference term $\Re(J^*K)$. In proton-proton scattering, the interference term has been calculated to be much smaller than the first two terms [79], and we find it

therefore plausible to neglect. In the case of two identical particles we thus obtain

$$R = \frac{2\pi}{\hbar} \sum_{\mathbf{k}_s} \sum_{\mathbf{k}'_s} \sum_{\mathbf{k}_c} 8|J|^2 f(\epsilon_{k_s}) f(\epsilon_{k_c})(1 - f(\epsilon_{k'_s}))\delta(E_f - E_i). \tag{6.12}$$

If the Auger process occurs by interaction of an electron and a hole, there is no need to antisymmetrize the wave function because we are then dealing with non-identical particles. The sum over spin configurations is then easily evaluated and the resulting capture rate is

$$R = \frac{2\pi}{\hbar} \sum_{\mathbf{k}_s} \sum_{\mathbf{k}'_s} \sum_{\mathbf{k}_c} 4|J|^2 f(\epsilon_{k_s}) f(\epsilon_{k_c})(1 - f(\epsilon_{k'_s}))\delta(E_f - E_i). \tag{6.13}$$

We define the sum

$$R_J = \frac{2\pi}{\hbar} \sum_{\mathbf{k}_s} \sum_{\mathbf{k}'_s} \sum_{\mathbf{k}_c} |J|^2 f(\epsilon_{k_s}) f(\epsilon_{k_c})(1 - f(\epsilon_{k'_s}))\delta(E_f - E_i). \tag{6.14}$$

With this abbreviation the capture rate in the case of identical and non-identical particles is given by

$$R = \begin{cases} 8R_J & \text{identical particles,} \\ 4R_J & \text{non-identical particles.} \end{cases} \tag{6.15}$$

In the following, we evaluate the direct Coulomb matrix element, J. The wetting-layer and quantum-dot wave functions are approximated by a separation of in-plane and z variables,

$$\begin{aligned} \Psi_k(\mathbf{r}) &= \Phi_k(\boldsymbol{\rho})\Phi_{\mathrm{WL}}(z) \\ \Psi_d(\mathbf{r}) &= \Phi_\perp(\boldsymbol{\rho})\Phi_z(z). \end{aligned} \tag{6.16}$$

This yields

$$\begin{aligned} J &= \left\langle d, \mathbf{k}'_s \left| V_c \right| \mathbf{k}_c, \mathbf{k}_s \right\rangle \\ &= \frac{e^2}{2\epsilon_r \epsilon_0} \frac{1}{S} \sum_{\boldsymbol{\beta}_\perp} \frac{1}{\beta_\perp} H(\beta_\perp) \\ &\times \int d^2\rho_s d^2\rho_c e^{i\boldsymbol{\beta}_\perp \cdot (\boldsymbol{\rho}_c - \boldsymbol{\rho}_s)} \Phi^*_{k'_s}(\boldsymbol{\rho}_s) \Phi^*_\perp(\boldsymbol{\rho}_c) \Phi_{k_s}(\boldsymbol{\rho}_s) \Phi_{k_c}(\boldsymbol{\rho}_c), \end{aligned} \tag{6.17}$$

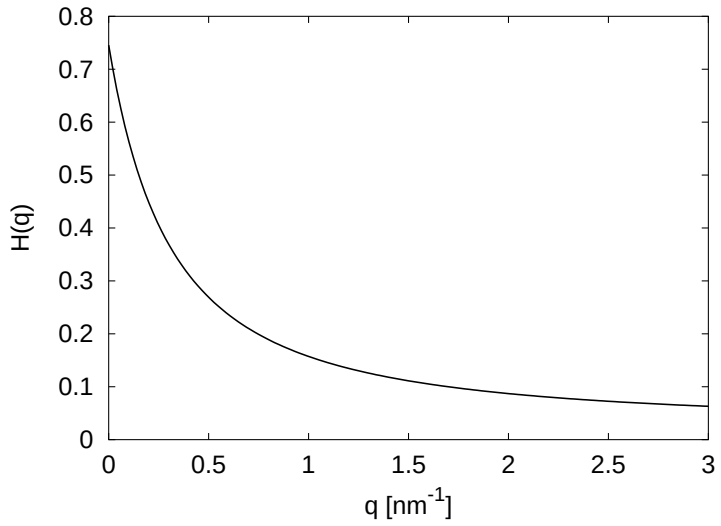

Figure 6.3: The form factor H(q), plotted for a quantum-dot $|1S\rangle$ electron, where the wetting-layer wave function is also for an electron. $V_e = 697$ meV, $r_0 = 10$ nm, $h = 5$ nm, $m^* = 0.07\mathrm{m}_0$, $\sigma_S = 1.72$ nm, $z_{0S} = 1.80$ nm and $d = 0.33$ nm.

where $H(\beta_\perp)$ is the form factor [80] in which the z-part of the wave functions is contained,

$$H(\beta_\perp) = \iint dz_s dz_c |\Phi_{\mathrm{WL}}(z_s)|^2 e^{-\beta_\perp |z_s - z_c|} \Phi_{\mathrm{WL}}(z_c) \Phi_z^*(z_c). \tag{6.18}$$

The form factor is plotted in Fig. 6.3, shown for a $|1S\rangle$ electronic quantum-dot state. The form factor depends on the z-part of the wave functions only. In fact the form factor of $|1P\rangle$ is very similar. Due to the small height of the quantum dots compared to the quantum-dot in-plane radius, the variational parameters that represent the quantization in the z-direction are very similar for $|1S\rangle$ and $|1P\rangle$. This simply reflects the fact that these states are within the same z-subband. Furthermore, the form factor for a hole quantum-dot state is similar to the form factor in Fig. 6.3.

The in-plane wetting-layer wave function, $\Phi_k(\boldsymbol{\rho})$, is approximated by a plane wave,

$$\Phi_k(\boldsymbol{\rho}) = \frac{1}{\sqrt{S}} e^{i\mathbf{k}\cdot\boldsymbol{\rho}}. \tag{6.19}$$

The integral over $\boldsymbol{\rho}_s$ in Eq. (6.17) then describes conservation of in-plane

crystal momentum,

$$\begin{aligned}\int d^2\rho_s e^{-i\boldsymbol{\beta}_\perp\cdot\boldsymbol{\rho}_s}\Phi^*_{k'_s}(\boldsymbol{\rho}_s)\Phi_{k_s}(\boldsymbol{\rho}_s) &= \frac{1}{S}\int d^2\rho_s e^{i(-\boldsymbol{\beta}_\perp+\mathbf{k}_s-\mathbf{k}'_s)\cdot\boldsymbol{\rho}_s} \\ &= \delta_{\boldsymbol{\beta}_\perp,\mathbf{k}_s-\mathbf{k}'_s}.\end{aligned} \tag{6.20}$$

With this selection rule, the Coulomb matrix element is written as

$$\left\langle d,\mathbf{k}'_s\left|V_c\right|\mathbf{k}_c,\mathbf{k}_s\right\rangle = \frac{e^2}{2\epsilon_r\epsilon_0}\frac{1}{S}\frac{H(|\mathbf{k}_s-\mathbf{k}'_s|)}{|\mathbf{k}_s-\mathbf{k}'_s|}\left\langle\Phi_\perp\left|e^{i(\mathbf{k}_s-\mathbf{k}'_s)\cdot\boldsymbol{\rho}_c}\right|\Phi_{k_c}\right\rangle_\perp, \tag{6.21}$$

where we define an in-plane scalar product as in Eq. (4.15) by

$$\langle\phi|\psi\rangle_\perp = \int_S d^2\rho\phi^*(\boldsymbol{\rho})\psi(\boldsymbol{\rho}). \tag{6.22}$$

Because we approximate Φ_{k_c} by a plane wave [Eq. (6.19)], the in-plane scalar product is essentially a Fourier transform of the in-plane quantum-dot wave function with respect to $(\mathbf{k}_s-\mathbf{k}'_s+\mathbf{k}_c)$. The matrix element inserted into Fermi's golden rule now gives the following

$$\begin{aligned}R_J = \frac{\pi}{2\hbar}\left(\frac{e^2}{\epsilon_r\epsilon_0}\right)^2\frac{1}{S^2}\sum_{\mathbf{k}_s}\sum_{\mathbf{k}'_s}\sum_{\mathbf{k}_c}\frac{|H(|\mathbf{k}_s-\mathbf{k}'_s|)|^2}{|\mathbf{k}_s-\mathbf{k}'_s|^2}\left|\left\langle\Phi_\perp\left|e^{i(\mathbf{k}_s-\mathbf{k}'_s)\cdot\boldsymbol{\rho}_c}\right|\Phi_{k_c}\right\rangle_\perp\right|^2 \\ \times f(\epsilon_{k_s})f(\epsilon_{k_c})(1-f(\epsilon_{k'_s}))\delta\left(\frac{\hbar^2k'^2_s}{2m_s}-\frac{\hbar^2k_s^2}{2m_s}-\left(E^c_{\mathrm{WL}}+\frac{\hbar^2k_c^2}{2m_c}-E_{\mathrm{d}}\right)\right),\end{aligned} \tag{6.23}$$

where E_d is the energy of the quantum-dot level to which the capture takes place. The sums R_J for capture into $|1S\rangle$ and $|1P\rangle$ are calculated in Appendix H.

For capture into $|1S\rangle$ it is found that

$$\begin{aligned}R_J^{|1S\rangle} = \frac{1}{8\pi^2\hbar}\left(\frac{e^2}{\epsilon_r\epsilon_0}\right)^2\beta_S^2\frac{m_c}{\hbar^2}\int dk_s k_s f(\epsilon_{k_s})\int dk'_s k'_s f(\epsilon_{k_{c0}}) \\ \times\int_0^{2\pi}d\theta\frac{|H(|\mathbf{k}_s-\mathbf{k}'_s|)|^2}{|\mathbf{k}_s-\mathbf{k}'_s|^2}\exp\left(-(|\mathbf{k}_s-\mathbf{k}'_s|^2+k_{c0}^2)\beta_S^2\right) \\ \times I_0(2\beta_S^2|\mathbf{k}_s-\mathbf{k}'_s|k_{c0}),\end{aligned} \tag{6.24}$$

where I_0 is a Bessel function of the second kind and θ is the angle between $\mathbf{k}_s$ and $\mathbf{k}'_s$.

For capture into $|1P\rangle$ we find

$$\begin{aligned} R_J^{|1P\rangle} = & \frac{1}{8\pi^2\hbar}\left(\frac{e^2}{\epsilon_r\epsilon_0}\right)^2 \beta_P^4 \frac{m_c}{\hbar^2} \int dk_s k_s f(\epsilon_{k_s}) \int dk'_s k'_s f(\epsilon_{k_{c0}}) \\ & \times \int_0^{2\pi} d\theta \frac{|H(|\mathbf{k}_s - \mathbf{k}'_s|)|^2}{|\mathbf{k}_s - \mathbf{k}'_s|^2} \exp\left(-\beta_P^2(|\mathbf{k}_s - \mathbf{k}'_s|^2 + k_{c0}^2)\right) \\ & \times [(|\mathbf{k}_s - \mathbf{k}'_s|^2 + k_{c0}^2) I_0(2\beta_P^2 |\mathbf{k}_s - \mathbf{k}'_s| k_{c0}) \\ & - 2|\mathbf{k}_s - \mathbf{k}'_s| k_{c0} I_1(2\beta_P^2 |\mathbf{k}_s - \mathbf{k}'_s| k_{c0})], \end{aligned} \tag{6.25}$$

where I_0 and I_1 are Bessel functions of the second kind.

Carrier-density dependence and Auger coefficients

In sections 3.3 and 4.2.2 it was shown that the phonon capture rate is proportional to the carrier density in the continuum from which the carrier is captured, if the density is not too high. In this regime the Fermi factor can be approximated by a Boltzmann factor, which, in turn, is proportional to the carrier density. This can be understood intuitively by the fact that only one continuum carrier is involved in the capture. In the case of Auger capture, two continuum carriers are involved in each capture process and it is therefore natural to consider the capture rate as being proportional to n^2, where n is the carrier density. Again, this occurs at low to moderate n, where the Fermi factor is approximated by a Boltzmann factor and this can be seen directly from Eq. (6.1) (for $[1 - f(\epsilon_{k'_s})] \approx 1$). This is confirmed in Fig. 6.4 where the dependence of the capture rate on carrier density is shown for capture into $|1S\rangle$ and $|1P\rangle$. The curves are seen to be very well fitted with $R = Cn_{2\mathrm{D}}^2$ up to $n_{2\mathrm{D}} \sim 5 \times 10^{16}$ m^{-2}. The proportionality constant will hereafter be called the "Auger coefficient" [38]. It will be labeled C_{cs}, where c = e, h and s = e, h. The indices therefore indicate the type of the captured and scattered carrier, respectively.

Dot-size dependence

Figures 6.5 and 6.6 show the Auger coefficients as a function of in-plane quantum-dot radius for carrier capture into $|1S\rangle$ and $|1P\rangle$, respectively.

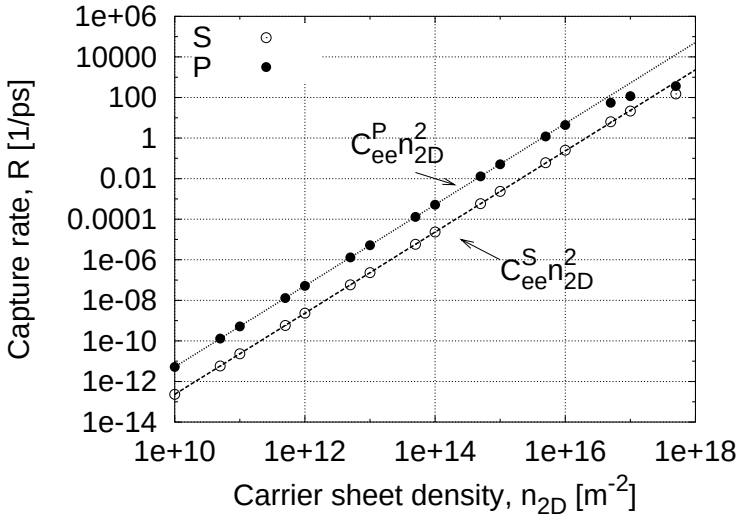

Figure 6.4: The carrier capture rate of electrons into $|1S\rangle$ and $|1P\rangle$ by scattering of electrons is shown versus sheet carrier density $n_{2\mathrm{D}}$. The carrier capture rate scales with carrier density as $R \propto n_{2\mathrm{D}}^2$, with proportionality constants, $C_{\mathrm{ee}}^S = 2.3 \times 10^{-21}$ m^4/s and $C_{\mathrm{ee}}^P = 5.2 \times 10^{-20}$ m^4/s. The dot is a truncated cone with $r_0 = 5.4$ nm, $h = 3$ nm, $\alpha = 30^\circ$ and the electron mass is taken to be $m^* = 0.07 m_0$.

These are shown for two different quantum-dot geometries. The results in Figures 6.5 and 6.6 show that for capture of a carrier of given type, scattering by electrons is in general more effective than scattering by holes. The same trends are seen if the coefficients are plotted as a function of ΔE, the energy spacing between the wetting-layer band edge and the quantum-dot energy level that the carrier is captured into. Figures 6.7 and 6.8 show the results of the right hand side panels of Figures 6.5 and 6.6 but plotted versus ΔE. Figure 6.7 shows capture of electrons and Figure 6.8 shows capture of holes, both graphs show capture into both $|1S\rangle$ and $|1P\rangle$.

The more efficient scattering by electrons can be explained by considering some given ΔE. For an incident carrier of given energy, ϵ_{k_c}, the energy that is transferred to the scattered carrier, that is either an electron or hole, is the same due to the energy conservation requirement. However, due to the smaller curvature in the energy dispersion for the holes the mean 'momentum transfer' so to say, $\langle|\mathbf{k}_s - \mathbf{k}'_s|\rangle$, is in general larger for holes. The Coulomb matrix element decreases with increasing $|\mathbf{k}_s - \mathbf{k}'_s|$ mainly

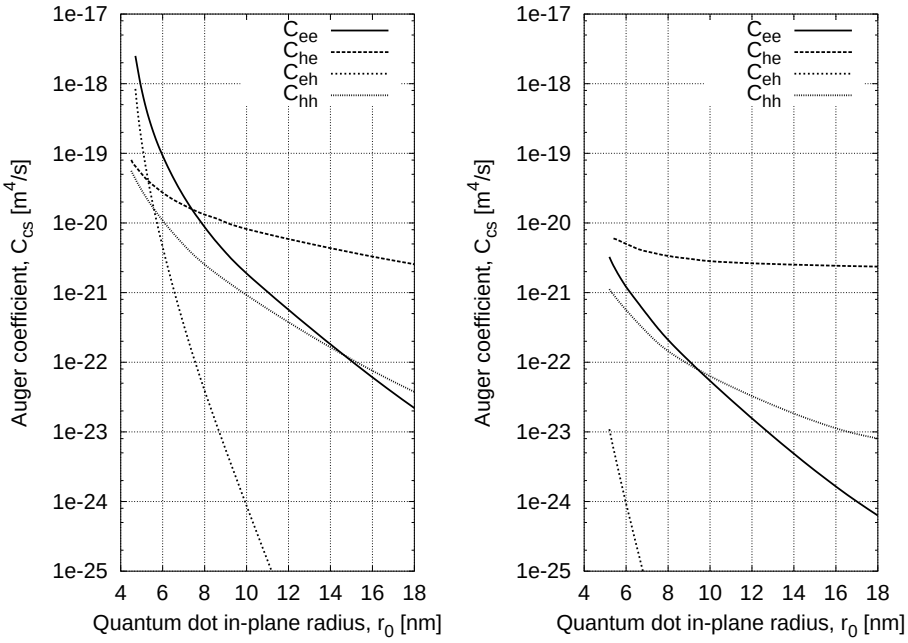

Figure 6.5: The Auger capture coefficients C_{ee}, C_{he}, C_{eh}, C_{hh} as a function of quantum dot in-plane radius for carrier capture into the state $|1S\rangle$. In the left panel the cone is non-truncated. The base angle is $\alpha = 12°$ and the height varies with r_0. In the right panel the cone is truncated. The height is constant, $h = 3$ nm, and we have set the base angle to be $\alpha = 30°$. The wetting-layer thickness is $d = 0.33$ nm in both cases, $V_e = 697$ meV and $V_h = 288$ meV.

because the $1/|\mathbf{r}_s - \mathbf{r}_c|$ dependence translates into a $1/|\mathbf{k}_s - \mathbf{k}'_s|$ in k-space but also because the form factor H decreases exponentially with increasing $|\mathbf{k}_s - \mathbf{k}'_s|$. Hence scattering by holes is in general less efficient than scattering by electrons. Furthermore it is clear from these graphs that for a given process the capture rate depends merely on this energy separation. This can be understood in terms of the wave functions, i. e. for a given ΔE the characteristic decay constants are similar and hence the wave-function overlaps that enter the capture rate are similar.

We can compare capture processes where the scattered carrier is of the same type but the captured ones are different. If we look at C_{ee} and C_{he} in the right panel of Figure 6.6 for capture into $|1P\rangle$ we see that C_{he}

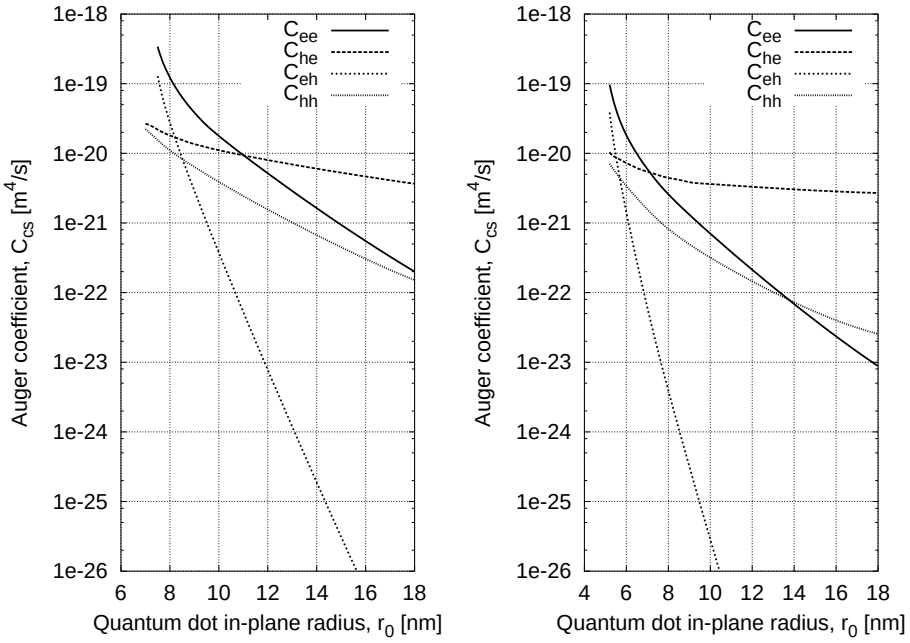

Figure 6.6: The Auger capture coefficients $C_{\rm ee}$, $C_{\rm he}$, $C_{\rm eh}$, $C_{\rm hh}$ as a function of quantum dot in-plane radius for carrier capture into the state $|1P\rangle$. In the left panel the cone is non-truncated. The base angle is $\alpha = 12°$ and the height varies with r_0. In the right panel the cone is truncated. The height is constant, $h = 3$ nm, and we have set the base angle to be $\alpha = 30°$. The wetting-layer thickness is $d = 0.33$ nm in both cases.

crosses $C_{\rm ee}$ at $r_0 \approx 7.1$ nm ($C_{\rm he} = C_{\rm ee} \approx 5.3 \times 10^{-21}{\rm m}^4/{\rm s}$) and is larger than $C_{\rm ee}$ beyond this radius. The slower decrease of $C_{\rm he}$ compared to $C_{\rm ee}$ in Figure 6.6 reflects the fact that the energy separation increases more slowly with r_0 for the hole levels than for the electron levels, see for instance Figs. 4.4 and 4.5.

Base-angle dependence

Finally, we investigate the dependence of the Auger coefficient on base angle α, shown in Fig. 6.9 for capture into $|1P\rangle$ of a non-truncated cone of in-plane radius $r_0 = 7.5$ nm. All the coefficients decrease with increasing α. This is because the dot becomes larger and the state becomes more

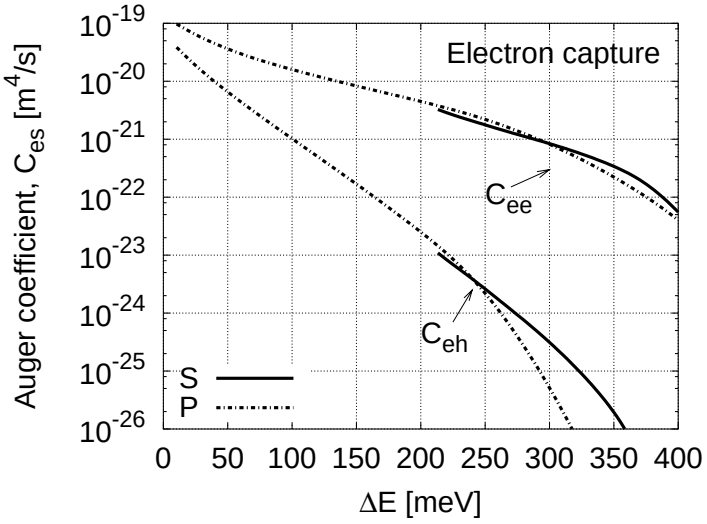

Figure 6.7: The Auger capture coefficients $C_{\rm ee}$ and $C_{\rm eh}$ for electron capture into $|1S\rangle$ and $|1P\rangle$ plotted versus ΔE, the energy difference between the wetting-layer band edge and $E_{|1S\rangle}$ or $E_{|1P\rangle}$, labeled as E_d. $h = 3$ nm and $\alpha = 30°$.

deeply bound. The coefficients $C_{\rm ee}$ and $C_{\rm he}$ are also shown for capture into a non-truncated cone of the same in-plane radius. These are lower than the corresponding coefficients for a truncated cone at the larger base angles. This is because the dot becomes taller as α increases. Therefore, the z-part of the quantum-dot wave function is centered farther away from the wetting layer (z_{0P} increases), and they overlap therefore less.

6.2 A simplified model of the Auger coefficient

The starting point of the calculations presented in section 6.1 was the ongoing collaboration with Prof. Alexander Uskov at the Lebedev Institute in Moscow. He had at the time developed a simplified model of the Auger coefficients, presented in Ref. [38], based on several approximations and assumptions. The idea was to perform similar calculations but with improved wave functions and without the approximations made in Ref. [38] and compare the two models. The Auger coefficient from Ref. [38] is given

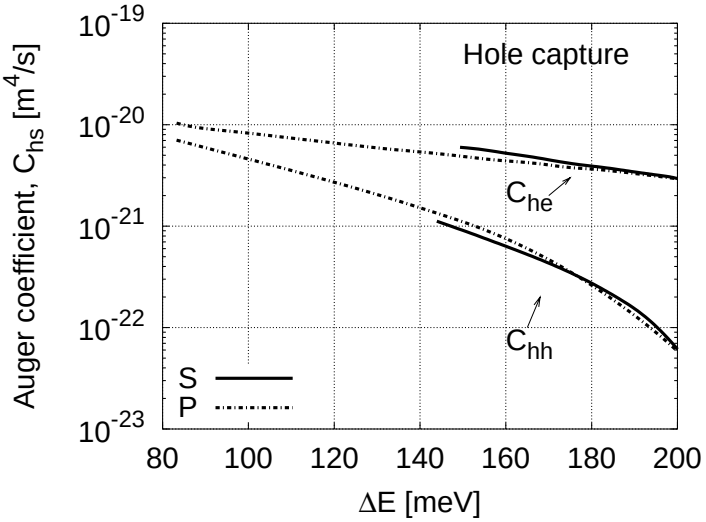

Figure 6.8: The Auger capture coefficients $C_{\rm he}$ and $C_{\rm hh}$ for hole capture into $|1S\rangle$ and $|1P\rangle$ plotted versus ΔE, the energy difference between the wetting-layer band edge and $E_{|1S\rangle}$ or $E_{|1P\rangle}$, labeled as E_d. $h = 3$ nm and $\alpha = 30°$.

by

$$\begin{aligned} C_{\rm cs} = & \frac{m_s e^4}{4\hbar^3 \epsilon_r^2 \epsilon_0^2 q_s^2} \\ & \times \frac{\kappa_W(\kappa_D + 2\kappa_W + 2q_s)^2}{H(\kappa_W + q_s)^2(\kappa_D + \kappa_W + q_s)^2} \\ & \times \pi \left(\frac{D}{\xi_{01}}\right)^2 \frac{J_0^2(q_s D/2)}{[(q_s D)^2/(2\xi_{01})^2 - 1]^2}, \end{aligned} \tag{6.26}$$

where $J_0(x)$ is the zero order Bessel function and $\xi_{01} = 2.4$ is its first root. The quantum dot is approximated by a cylinder with diameter D and height H. The quantum-dot wave function is assumed to be separable in in-plane and z-coordinates and the in-plane wave function is taken to be the solution to a circular potential with infinite potential walls. Confinement in the z-direction is assumed to be finite and κ_D and κ_W are the characteristic decay constants of wave functions in barriers surrounding the quantum dot and the wetting layer, respectively. The wave number $q_s = \sqrt{2m_s\Delta\epsilon_c/\hbar^2}$ is the wave number of a scattered carrier to which the energy increment $\Delta\epsilon_c$ has been transfered from the captured carrier. This energy increment is given

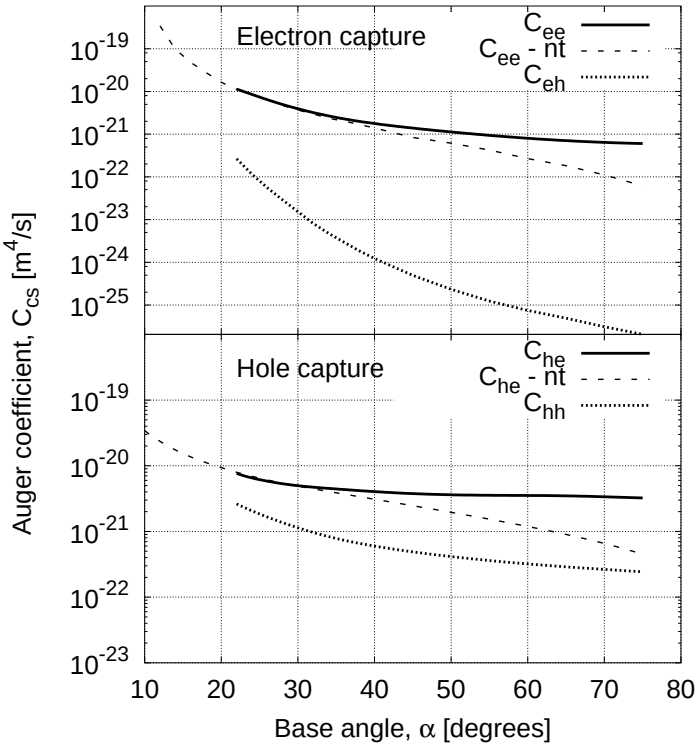

Figure 6.9: Base-angle dependence of Auger coefficients for a truncated cone with $r_0 = 7.5$ nm and $h = 3$ nm. For comparison C_{ee} and C_{he} for capture into a non-truncated cone, labeled "nt", with the same r_0 are shown.

by

$$\Delta\epsilon_c = \epsilon_{Dc} - \epsilon_{Wc}, \tag{6.27}$$

where ϵ_{Dc} and ϵ_{Wc} are the respective binding energies in the quantum dot and the wetting layer. It is assumed that $\Delta\epsilon_c$ does not vary with D. The wave vector of the captured carrier is approximated by $\mathbf{k}_c \approx 0$ and the scattering carrier by $\mathbf{k}_s \approx 0$. Such an approximation amounts to assuming that the only carriers that contribute to the capture are the ones with

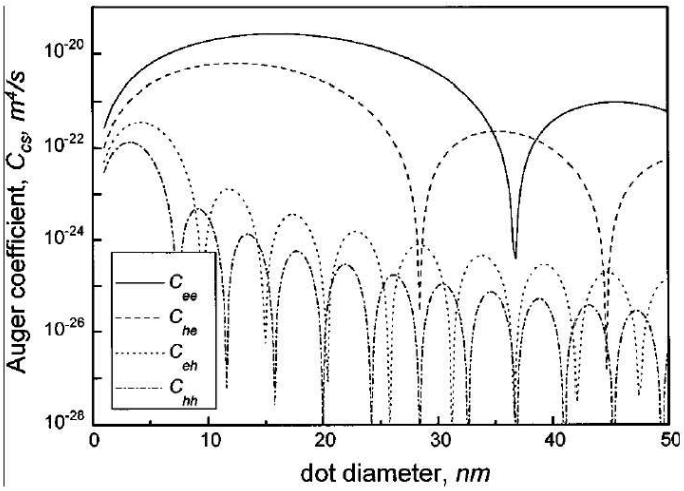

Figure 6.10: Auger coefficients plotted versus the quantum-dot diameter, D. From Ref. [38].

the lowest energy (and the largest Fermi factor). The wave number q_s is approximated as

$$q_s \approx k'_s. \tag{6.28}$$

The wave-vector terms that enter in the derivation of Eq. (6.26), $|\mathbf{k}_s - \mathbf{k}'_s|$ and $|\mathbf{k}_s - \mathbf{k}'_s + \mathbf{k}_c|$, are approximated by

$$\begin{aligned} |\mathbf{k}_s - \mathbf{k}'_s| &\approx k'_s \approx q_s \\ |\mathbf{k}_s - \mathbf{k}'_s + \mathbf{k}_c| &\approx k'_s \approx q_s, \end{aligned} \tag{6.29}$$

where $\mathbf{k}_s$, $\mathbf{k}_c$ and $\mathbf{k}'_s$ are defined as in section 6.1. The middle line in Eq. (6.26) gives the matrix element in the z-direction. The in-plane matrix element is the last line of Eq. (6.26). The Auger coefficients calculated with Eq. (6.26) are shown in Fig. 6.10.[1]

In general, quantitative comparison between the two models, the one presented in section 6.1 and the model from Eq. (6.26), is difficult, mainly

[1]Note that the factor of 2 in the last line of Eq. (6.26) is misprinted as 4 in Ref. [38]. However, all results in [38] are plotted with the correct factor of 2.

due to the fact that different dot geometries have been assumed. Furthermore, the latter model does not account for the increasing energy separation between the wetting-layer band edge and the quantum-dot level with increasing dot size ($\Delta\epsilon_c$ from Eq. (6.27) does not change with dot size). We therefore choose to take an alternative route. We will in the following develop a similar model to the one presented in Eq. (6.26) but we will use the same wave functions as in section 6.1. This model will then be compared to the model in section 6.1. We develop the simplified model in the case of capture into $|1S\rangle$. With the approximations for the wave vectors in Eq. (6.29) the in-plane matrix element from Eq. (6.21) is given by

$$\begin{aligned} M_\rho &\equiv \langle \Phi_\perp | e^{i(\mathbf{k}_s - \mathbf{k}'_s} | \Phi_{k_c} \rangle_\perp \\ &= \frac{2\sqrt{\pi}\beta_S}{\sqrt{S}} \exp\left(-\frac{(\mathbf{k}_s - \mathbf{k}'_s + \mathbf{k}_c)^2 \beta_S^2}{2} \right) \\ &\approx \frac{2\sqrt{\pi}\beta_S}{\sqrt{S}} \exp\left(-\frac{q_s^2 \beta_S^2}{2} \right), \end{aligned} \tag{6.30}$$

and the Coulomb matrix element [Eq. (6.21)] is then given by

$$\left\langle d, \mathbf{k}'_s \left| V_c \right| \mathbf{k}_c, \mathbf{k}_s \right\rangle \approx \frac{\sqrt{\pi} e^2}{\epsilon_r \epsilon_0} \frac{1}{S^{3/2}} \frac{H(q_s)}{q_s} \beta_S \exp\left(-\frac{q_s^2 \beta_S^2}{2} \right). \tag{6.31}$$

Furthermore, individual terms in the summation of Eq. (6.1) do not depend on any angles of wave vectors. We can therefore transform the summation in Eq. (6.1) into an integral,

$$\sum_{\mathbf{k}_c, \mathbf{k}_s, \mathbf{k}'_s} \longrightarrow \frac{S^3}{(2\pi)^3} \int dk_c k_c \int dk_s k_s \int dk'_s k'_s, \tag{6.32}$$

where the integration over angles has already been performed. The integral over k'_s is easily performed due to the δ function. The wavenumber q_s is calculated from $q_s = \sqrt{2m_s \left(E_{\mathrm{WL}} - E_{|1S\rangle} \right) / \hbar^2}$. We obtain

$$R = \frac{m_s e^4}{2\hbar^3 \epsilon_r^2 \epsilon_0^2} \frac{|H(q_s)|^2}{q_s^2} 4\pi \beta_S^2 \exp\left(-q_s^2 \beta_S^2 \right) n_{2\mathrm{D}}^2, \tag{6.33}$$

where we have used the relation $\int dk k f(\epsilon_k) = \pi n_{2\mathrm{D}}$. In arriving at Eq. (6.33) we have therefore neglected the dependence of the Coulomb matrix element

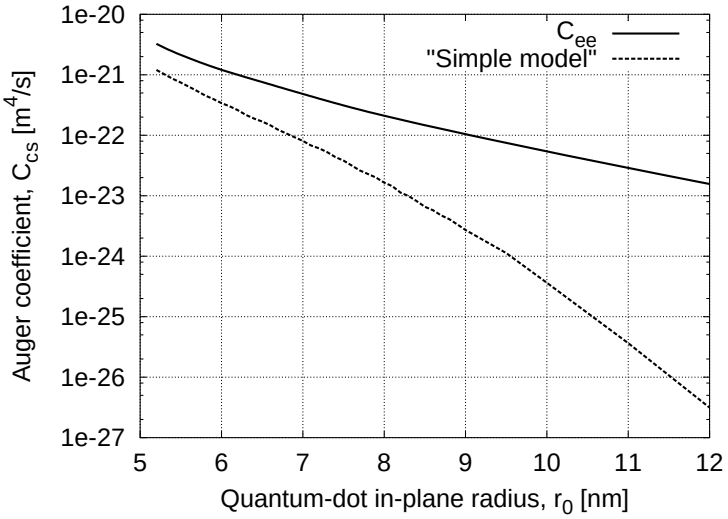

Figure 6.11: Auger capture coefficient $C_{\rm ee}$ for capture into $|1S\rangle$ calculated from the model in section 6.1 and the "simple model" from Eq. (6.34). Same dot parameters as in the right hand side panel of Fig. 6.5 are used.

on wave vectors, which, in view of Eq. (6.21) seems to be a rather crude approximation. The Auger coefficient derived from Eq. (6.33) is given by

$$C_{\rm cs} = \frac{m_s e^4}{2\hbar^3 \epsilon_r^2 \epsilon_0^2} \frac{|H(q_s)|^2}{q_s^2} 4\pi\beta_S^2 \exp\left(-q_s^2\beta_S^2\right). \tag{6.34}$$

We have multiplied by a factor of 8 that comes from the sum over spin configurations since it is also done in section 6.1.[2] The analogy with Eq. (6.26) is clear. $|H(q_s)|^2$ (the form factor squared) corresponds to the second line in Eq. (6.26) and the term $4\pi\beta_S^2 \exp\left(-q_s^2\beta_S^2\right)$ from the in-plane matrix element corresponds to the last line in Eq. (6.26). This is not very surprising since separable wave functions are used in both models and the same approximations for wave vectors used. In Fig. 6.11 we plot the Auger coefficient $C_{\rm ee}$, calculated with Eq. (6.34), together with the corresponding coefficient from the model in section 6.1. The same dot parameters as in the left hand side panel of Fig. 6.5 are used. We hold the dot height constant, $h = 3$ nm, while varying r_0. One clear difference is seen between the coefficients in Figs. 6.10 and 6.11. The oscillations from Fig. 6.10 are absent in both

[2]Note that there has only been multiplied by a factor of 4 in Eq. (6.26).

curves in Fig. 6.11. The oscillations in Fig. 6.10 arise from oscillations in the in-plane matrix element with dot size [last line of Eq. (6.26)]. The zero points of $C_{\rm cs}$ are the zeros of the Bessel function $J_0(q_s D/2)$. These oscillations occur due to the assumption that the in-plane potential walls are infinite. Therefore they are not seen in Fig. 6.11.

A comparison of the two curves in Fig. 6.11 reveals that $C_{\rm ee}$ from the "simple model" is always lower than the coefficient calculated with the more elaborate model from section 6.1. Furthermore, it decreases much faster with dot size. At $r_0 = 12$ nm the value is about 10^{-23} m^4/s for the latter model while it is about 4 orders of magnitude lower for the "simple model". This indicates that some of the approximations leading to Eq. (6.34) cannot be justified. The fast decrease of $C_{\rm ee}$ in the "simple model" is seen to arise from the exponential decrease of $|M_\rho|^2$ [Eq. (6.30)]. Both β_S and q_s increase with dot size. β_S increases because the wave function becomes more extended and q_s increases because $(E_{\rm WL} - E_{|1S\rangle})$ increases. This leads to the decrease of $|M_\rho|^2$ over about five orders of magnitude for r_0 ranging from about 5 to 12 nm. At the same time the form factor squared, $|H(q_s)|^2$, decreases by about a factor 1.5. The small variation of $H(q_s)$ with dot size lies mainly in the fact that the dot height is constant, $h = 3$ nm, so the $z-$part of the dot wave function does not vary appreciably with r_0. The large variation of M_ρ with q_s also indicates that the dependence of M_ρ on wave vectors [Eq. (6.30)] cannot be neglected in the evaluation of integrals over wave vectors but this was done to arrive at Eq. (6.34).

6.3 Comparison of Auger and phonon capture rates

In this section we compare our previous calculations of phonon-mediated capture rates from section 4.2 to Auger carrier capture rates that were calculated in section 6.1. In section 4.2 we calculated rates of carrier capture of electrons with a hole already present in the dot, or vice versa. Phonon-mediated carrier capture rates into an empty dot state were obtained by setting the intradot Coulomb interaction energy to zero. The results of these calculations were shown in Fig. 4.7. We plot the Auger carrier capture rates and single-phonon capture rates (emission of one LO phonon) in Fig. 6.12 as a function of carrier sheet density. The phonon capture rate is determined by Eq. (4.25). The single-phonon capture process is allowed for $E_d > E_{\rm WL} - \hbar\omega_{\rm LO}$ due to the energy conservation requirement. For the dot geometry that we study here, i. e. a truncated cone with $r_0 = 5.4$ nm,

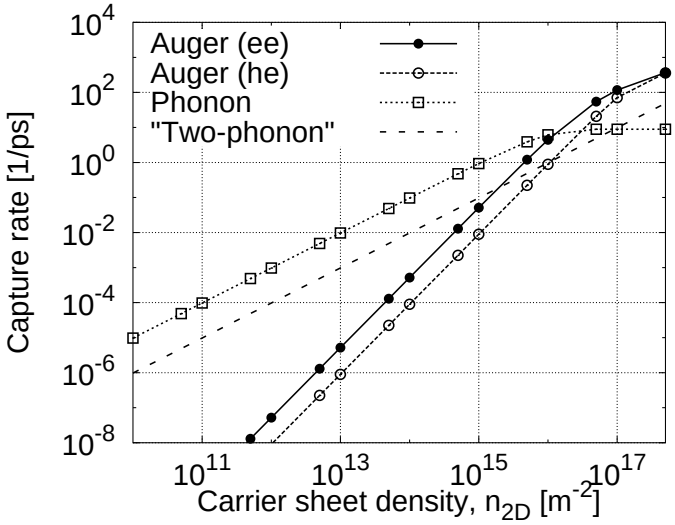

Figure 6.12: The dependence of phonon-mediated and Auger carrier capture rates on carrier sheet density for a quantum-dot geometry where phonon-mediated carrier capture is allowed. Single-phonon capture is labeled by 'Phonon'. The Auger coefficient is given by $C_{\rm ee} = 6.6 \times 10^{-21}{\rm m}^4/{\rm s}$ and the phonon coefficient by $A_e = 9.7 \times 10^{-4}{\rm m}^2/{\rm s}$. The dot is a truncated cone with $r_0 = 5.4$ nm, $h = 3$ nm, $\alpha = 30^\circ$. Wetting-layer thickness is $d = 0.33$ nm and $E_{\rm WL} - E_{\rm 1P} = 31$ meV.

$h = 3$ nm and $\alpha = 30^\circ$, phonon capture of electrons is allowed but the hole level is too deeply bound to be attained in a single-phonon process. We therefore only show electron phonon capture. It is seen from Fig. 6.12 that for the dot geometry that we have chosen, the Auger capture rates are much smaller than phonon-mediated capture rates at low to moderate carrier densities and Auger rates exceed the single-phonon-mediated capture rates at carrier sheet densities $\sim 10^{16}{\rm m}^{-2}$. The largest wetting-layer carrier density attained in rate-equation simulations is about $10^{24}{\rm m}^{-3}$ [81] which translates into a carrier sheet density $n_{\rm 2D} = 3.3 \times 10^{14}{\rm m}^{-2}$ here (we have used wetting-layer thickness $d = 0.33$ nm). Two-phonon capture rates have been shown to be at most one order of magnitude smaller than single-phonon capture rates (see Fig. 3.7 in section 3.2 and Ref. [49]). As a guide to the eye we plot $R = 0.1 A_e n_{\rm 2D}$ (labeled "Two-phonon") in Fig. 6.12, where A_e is the single-phonon capture coefficient [Eq. (4.30)], to illustrate the regime for the two-phonon capture rate. Auger capture rates exceed two-phonon capture rates at carrier sheet densities $\sim 10^{15}{\rm m}^{-2}$.

We stress however that the dot geometry is explicitly chosen so that single-phonon capture is allowed. It was mentioned in section 4.2.2 that for $\alpha = 30^\circ$ and $V_e = 697$ meV, the range of dot sizes, where single-phonon capture is allowed, is very narrow. One reason is the strong confinement that gives a fast decrease of energy levels with dot size. It may very well be the case that phonon-mediated capture processes are very efficient *for dot geometries where they are allowed* but we need to bear in mind that Auger processes of the type that we have studied in this chapter are always allowed as long as bound states exist in the dots. There is therefore no definite conclusion that can be reached as to whether phonon– or Coulomb–mediated capture processes are more efficient. The decisive factor is mainly the strength of the confinement and the actual parameters that define the dot (shape, strain, piezoelectric effects,...) which, to date, are not very well known.

6.4 Orthogonalization of wetting-layer states to quantum-dot states

In the preceeding sections, we have calculated the Auger carrier capture coefficients under the assumption that the wave functions for the wetting layer and the quantum dot are obtained by separate solutions of the Schrödinger equation for the wetting-layer and the quantum-dot system. The quantum-dot wave functions are variational solutions to the Schrödinger equation for a cone *in the presence of the wetting layer* (see Appendix D). For instance, the ground state wave function is written as

$$\Psi_S(\mathbf{r}) = \frac{1}{\sqrt{\sigma_S \beta_S^2 \pi^{3/2}}} \exp\left(-\frac{(z - z_{0S})^2}{2\sigma_S^2}\right) \exp\left(-\frac{\rho^2}{2\beta_S^2}\right). \tag{6.35}$$

The wetting-layer wave functions are solved for only the wetting layer, i. e., not in the presence of the quantum-dot potential. The wetting-layer wave functions can therefore be written as the conventional quantum-well functions,

$$\begin{aligned} \Psi_k(\mathbf{r}) &= \Phi_k(\boldsymbol{\rho})\Phi_{\mathrm{WL}}(z) \\ &= \frac{e^{i\mathbf{k}\cdot\boldsymbol{\rho}}}{\sqrt{S}}\Phi_{\mathrm{WL}}(z), \end{aligned} \tag{6.36}$$

where $\Phi_{\mathrm{WL}}(z)$ is the wave function associated with a one-dimensional quantum well with finite confinement and S is a macroscopic area, e. g. the total wetting-layer area. The fact that in the quantum-dot wave-function solutions, the wetting-layer is taken into account, but the quantum dot is not taken into account in the wetting-layer wave-function solutions means that the wave functions associated with the wetting-layer states are not inherently orthogonal to the quantum-dot states. This might lead to unphysical overlaps of wave functions that could affect the capture rate. A way to avoid such overlaps is to orthogonalize the wetting-layer states to the quantum-dot states. In general, orthogonalization is not an easy task for such a system. It was tried in Ref. [23] to calculate the wetting-layer states in a combined quantum-dot and wetting-layer system but unrealistic states were found. It can be done analytically or semi-analytically in simple geometries, such as for a spherical quantum dot, where the "wetting layer" is a 3D continuum. This we have seen already in chapter 5 and Appendix G.1. For more complex geometries, such as the one that we study here, one must resort to numerical calculations of the wetting-layer states [82] and time consuming calculations of the carrier capture rates. In this section we will investigate the influence of the orthogonalization on Auger carrier capture rates without numerical calculations such as the ones presented in [82]. We follow here the same procedure as in Refs. [34, 80], where only the in-plane part of the wetting-layer wave function is orthogonalized to the in-plane part of the quantum-dot wave function. As we shall see, the "total" wetting-layer and quantum-dot wave functions, with the $z-$part included, will then also be orthogonal to each other. We take only the quantum-dot ground state into account in the calculations and write the wetting-layer and quantum-dot states as in Eq. (6.16). We write the "new" wetting-layer states as

$$|\widetilde{\Phi}_k\rangle = \frac{1}{N_k}\left[|\Phi_k\rangle - \langle\Phi_\perp|\Phi_k\rangle_\perp|\Phi_\perp\rangle\right], \tag{6.37}$$

where $\Phi_\perp(\boldsymbol{\rho})$ is the in-plane part of the quantum-dot wave function, given by

$$\Phi_\perp(\boldsymbol{\rho}) = \frac{1}{\sqrt{\pi\beta_S^2}}\exp\left(-\frac{\rho^2}{2\beta_S^2}\right) \tag{6.38}$$

for the ground state. N_k is a normalization constant given by

$$N_k^2 = 1 - |\langle\Phi_\perp|\Phi_k\rangle_\perp|^2 . \tag{6.39}$$

The "new" wetting-layer state, $|\widetilde{\Psi}_k\rangle = |\widetilde{\Phi}_k\rangle|\Phi_{\mathrm{WL}}\rangle$, is therefore orthogonal to the quantum-dot state, $|\Psi_d\rangle$, because we have that

$$\begin{aligned}\langle\Psi_d|\Psi_k\rangle &= \frac{1}{N_k}\langle\Phi_z|\Phi_{\mathrm{WL}}\rangle_z\left[\langle\Phi_\perp|\Phi_k\rangle_\perp - \langle\Phi_\perp|\Phi_k\rangle_\perp\right] \\ &= 0\end{aligned} \tag{6.40}$$

where the scalar product in z is defined as

$$\langle\Phi_z|\Phi_{\mathrm{WL}}\rangle_z = \int_{-\infty}^{\infty} dz\Phi_z^*(z)\Phi_{\mathrm{WL}}(z). \tag{6.41}$$

Note that the orthogonalization in Eq. (6.37) is not the only possibility. For instance, another wetting-layer state that is orthogonal to the quantum-dot state is the following state,

$$|\widetilde{\Psi}_k\rangle = \frac{1}{N_k'}\left[|\Psi_k\rangle - \langle\Psi_d|\Psi_k\rangle|\Psi_d\rangle\right], \tag{6.42}$$

where the scalar product is now $\langle\Psi_d|\Psi_k\rangle = \int d^3r\Psi_d^*(\mathbf{r})\Psi_k(\mathbf{r})$ and N_k' is a normalization constant different from N_k.

With the orthogonalization in Eq. (6.37), we have simultaneously imposed that the new in-plane wetting-layer states, $|\widetilde{\Phi}_k\rangle$, are no longer orthonormal to each other. In particular, in-plane momentum is no longer conserved, i. e., the relation $\langle\widetilde{\Phi}_k|\widetilde{\Phi}_{k'}\rangle = \delta_{\mathbf{k},\mathbf{k}'}$ does not hold. We do therefore not have an orthonormal basis of wave functions for the combined quantum-dot and wetting-layer system. We need however to bear in mind that the purpose of our orthogonalization procedure is to calculate the Coulomb matrix element. The matrix element contains an integration over two spatial variables, $\mathbf{r}_s$ and $\mathbf{r}_c$ for the scattered and captured carrier respectively. Whenever localized quantum-dot and delocalized wetting-layer states are paired with the same spatial variable, we replace $|\Phi_k\rangle$ by $|\widetilde{\Phi}_k\rangle$. We notice in the Coulomb matrix element [Eq. (6.17)] that the integration over $\mathbf{r}_s$ only pairs wetting-layer states together. We will therefore not change integrals over $\mathbf{r}_s$. Quantum-dot and wetting-layer states are paired in the integration over the spatial variable $\mathbf{r}_c$. In particular, the scalar product $\langle\Phi_\perp|e^{i\boldsymbol{\beta}_\perp\cdot\boldsymbol{\rho}_c}|\Phi_{k_c}\rangle_\perp$ changes due to Eq. (6.37). In the following, we will re-evaluate this scalar product using Eq. (6.37).

We have that

$$\begin{aligned}\langle\Phi_\perp|e^{i\boldsymbol{\beta}_\perp\cdot\boldsymbol{\rho}_c}|\widetilde{\Phi}_{k_c}\rangle_\perp &= \int d^2\rho_c \Phi_\perp^*(\boldsymbol{\rho}_c) e^{i\boldsymbol{\beta}_\perp\cdot\boldsymbol{\rho}_c}\widetilde{\Phi}_{k_c}(\boldsymbol{\rho}_c) \\ &= \frac{2\sqrt{\pi}\beta_S}{N_k\sqrt{S}}\left[\exp\left(-\frac{(\mathbf{k}_c+\boldsymbol{\beta}_\perp)^2\beta_S^2}{2}\right) - \exp\left(-\frac{\left(2k_c^2+\beta_\perp^2\right)\beta_S^2}{4}\right)\right]\end{aligned} \tag{6.43}$$

It is easily verified that the relation $\langle\Phi_\perp|\widetilde{\Phi}_{k_c}\rangle_\perp = 0$ is satisfied by setting $\beta_\perp = 0$ in Eq. (6.43). Hence, $\langle\Psi_d|\Psi_k\rangle = 0$ is also fulfilled. The term that enters the capture rate is the scalar product squared

$$\begin{aligned}&\left|\langle\Phi_\perp|e^{i\boldsymbol{\beta}_\perp\cdot\boldsymbol{\rho}_c}|\widetilde{\Phi}_{k_c}\rangle_\perp\right|^2 = \frac{4\pi\beta_S^2}{N_k^2 S}\exp\left(-\frac{(2k_c^2+\beta_\perp^2)\beta_S^2}{2}\right) \\ &\times\left[\exp\left(-\frac{\beta_S^2\beta_\perp^2}{2} - 2k_c\beta_\perp\beta_S^2\cos\phi\right) + 1 - 2\exp\left(-\frac{\beta_S^2\beta_\perp^2}{4} - k_c\beta_\perp\beta_S^2\cos\phi\right)\right]\end{aligned} \tag{6.44}$$

and integration over ϕ, the angle between $\boldsymbol{\beta}_\perp$ and $\mathbf{k}_c$, yields

$$\begin{aligned}\langle|M_\rho|^2\rangle_\phi &\equiv \int_0^{2\pi} d\phi \left|\langle\Phi_\perp|e^{-i\boldsymbol{\beta}_\perp\cdot\boldsymbol{\rho}_c}|\widetilde{\Phi}_{k_c}\rangle_\perp\right|^2 \\ &= \frac{(8\pi)^2\beta_S^2}{N_k^2 S}\exp\left(-\frac{(2k_c^2+\beta_\perp^2)\beta_S^2}{2}\right) \\ &\times\left[\exp\left(-\frac{\beta_S^2\beta_\perp^2}{2}\right) I_0(2k_c\beta_\perp\beta_S^2) + 1 - 2\exp\left(-\frac{\beta_S^2\beta_\perp^2}{4}\right) I_0(k_c\beta_\perp\beta_S^2)\right],\end{aligned} \tag{6.45}$$

where I_0 is a Bessel function of the second kind. The selection rule from Eq. (6.20) gives $\boldsymbol{\beta}_\perp = \mathbf{k}_s - \mathbf{k}_s'$. Eq. (6.45) can be compared to Eq. (H.9) which is the scalar product obtained with wetting-layer plane-wave states, $|\Phi_k\rangle$. In Fig. 6.13 we plot the average in-plane matrix elements, calculated with the two methods, as a function of $\beta_\perp$. At $\beta_\perp = 0$ the matrix element with the orthogonalized plane waves is zero as expected. However, for the non-orthogonalized plane waves, it is maximal, simply because it is essentially a Fourier transform of the Gaussian ground state wave function with respect to $\boldsymbol{\beta}_\perp$, see e. g. Eq. (H.4), i. e., also a Gaussian. For small $\beta_\perp$, the matrix element with orthogonalized plane waves, $\langle|M_\rho^O|^2\rangle_\phi$, is much smaller than the matrix element with the non-orthogonal waves, $\langle|M_\rho^P|^2\rangle_\phi$.

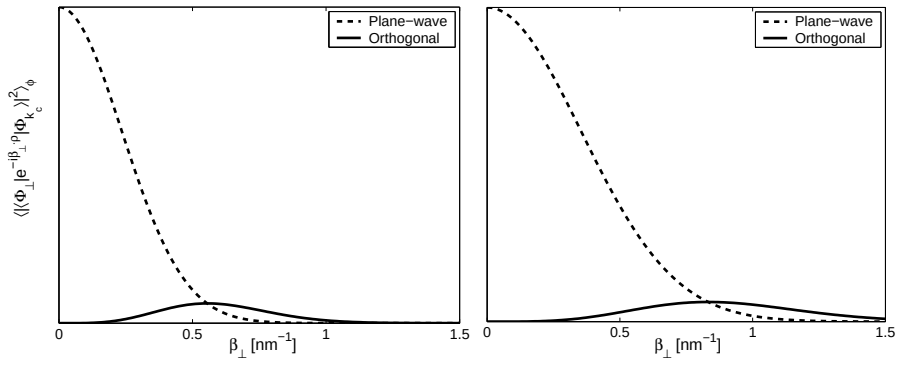

Figure 6.13: The average in-plane matrix element [Eq. (6.45)], compared to the average in-plane matrix element found using plane-wave states [Eq.(H.9))], for $\beta_s = 3$ nm (left) and $\beta_s = 2$ nm (right). We have set $k_c = 0$.

As $\beta_\perp$ increases, $\langle|M_\rho^O|^2\rangle_\phi$ exceeds $\langle|M_\rho^P|^2\rangle_\phi$, at higher $\beta_\perp$ for the smaller β_S. Figs. 6.14 and 6.15 show the Auger coefficients for capture of electrons and holes, respectively, calculated with the two methods. The coefficients are plotted as a function of r_0 in the range where only $|1S\rangle$ is bound in the dot. In general it is seen that Auger coefficients calculated with the orthogonalization, $C_{\mathrm{cs,o}}$, are smaller than the ones calculated for plane waves, $C_{\mathrm{cs,p}}$, by about one order of magnitude in most cases. Due to the relatively low ΔE, i. e., the energy separation between the wetting-layer band edge and the quantum-dot level, $|\mathbf{k}_s - \mathbf{k}'_s|$ is relatively low. This is also where the in-plane matrix element for orthogonalized plane waves, $\langle|M_\rho^O|^2\rangle$ is smaller than $\langle|M_\rho^P|^2\rangle$ (we have the selection rule $\boldsymbol{\beta}_\perp = \mathbf{k}_s - \mathbf{k}'_s$ from Eq. (6.20)). As the dot becomes larger, the orthogonalization procedure is slightly more complex, because then the wetting-layer state needs to be orthogonal to all quantum-dot states. This can be achieved for instance by a generalization of Eq. (6.37),

$$|\widetilde{\Phi}_k\rangle = \frac{1}{N_k}\left(|\Phi_k\rangle - \sum_{i=1}^{n_b}\langle\Phi_\perp^i|\Phi_k\rangle_\perp|\Phi_\perp^i\rangle\right), \tag{6.46}$$

where n_b is the number of bound states in the dot and $|\Phi_\perp^i\rangle$ is the in-plane state for bound state i. We have not pursued such calculations for several reasons. Most importantly, the orthogonalization procedure such as the one presented here includes some degree of arbitrariness. This can be seen for

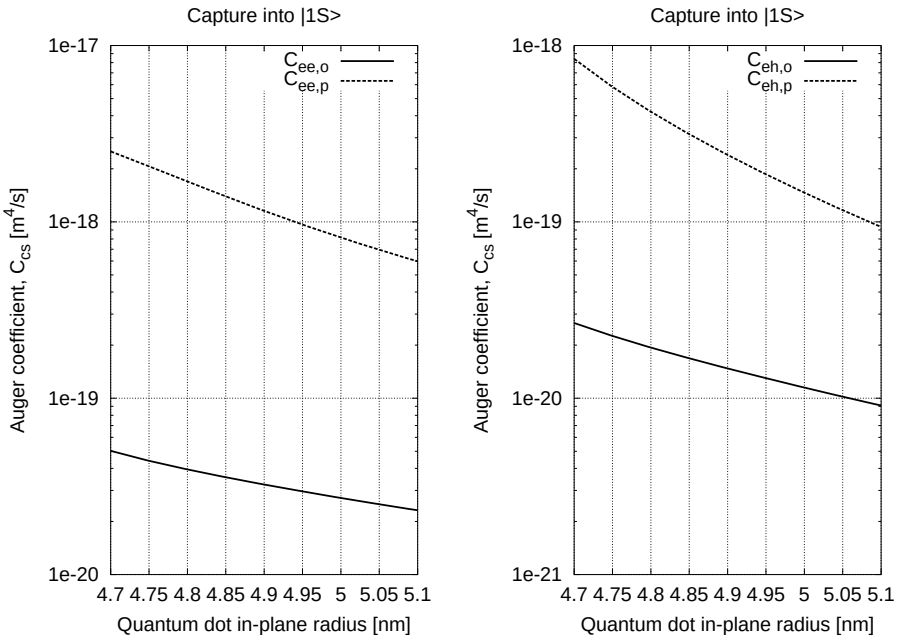

Figure 6.14: The Auger coefficients C_{ee} (left) and C_{eh} (right) calculated with orthogonalized plane waves ("$C_{\mathrm{cs,o}}$") compared with results obtained by non-orthogonalized plane waves ("$C_{\mathrm{cs,p}}$").

instance by comparing Eqs. (6.37) and (6.42). Both give different wetting-layer states that are orthogonal to dot states. Further work is needed to understand the differences and whether an entirely different approach is needed, e. g., numerical methods.

6.5 Auger transport

In this section we will investigate a mechanism of Auger transport which, if effective, might reduce spectral hole burning. The term 'spectral hole burning' is used about a local decrease that can occur in gain spectra at a given energy if not enough active carriers are present at this transition energy. In the process that we investigate here, illustrated in Fig. 6.16, a carrier in the vicinity of a quantum dot interacts with a quantum-dot carrier in another quantum dot promoting the latter carrier out of the

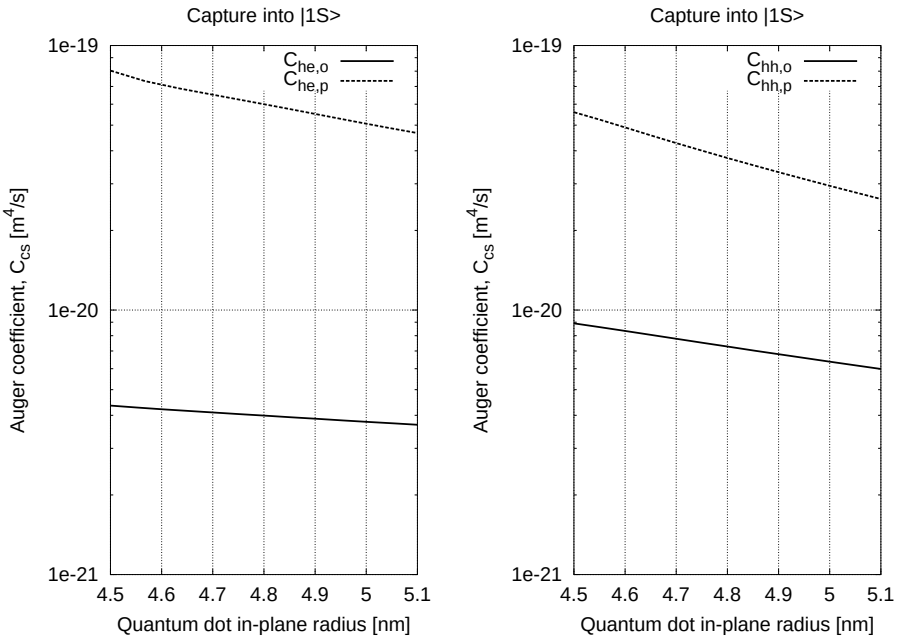

Figure 6.15: The Auger coefficients C_{he} (left) and C_{hh} (right) calculated with orthogonalized plane waves ("$C_{\mathrm{cs,o}}$") compared with results obtained by non-orthogonalized plane waves ("$C_{\mathrm{cs,p}}$").

dot while the former one is captured into the first dot. It would reduce spectral hole burning if the quantum-dot state to which the former carrier is captured is a lasing level while the quantum-dot state, from which the latter carrier is promoted, is not. We will show in this section that such a process depends on the dipole matrix element between quantum-dot and wetting-layer states to fourth order and only if this matrix element is on the order of the quantum-dot typical size will it be efficient in self-assembled quantum dots. We will however show that this is not the case due to the fact that this dipole matrix element is one order of magnitude smaller than typical quantum-dot dimensions. In the language of Fermi's golden rule this process is described by the capture rate

$$R = \frac{2\pi}{\hbar} \sum_{\mathbf{k}_c, \mathbf{k}'_s} \left| \langle d_1, \mathbf{k}'_s \left| V_c \right| \mathbf{k}_c, d_2 \rangle \right|^2 f(\epsilon_{k_c})(1 - f(\epsilon_{k'_s}))\delta\left(E_f - E_i\right), \quad (6.47)$$

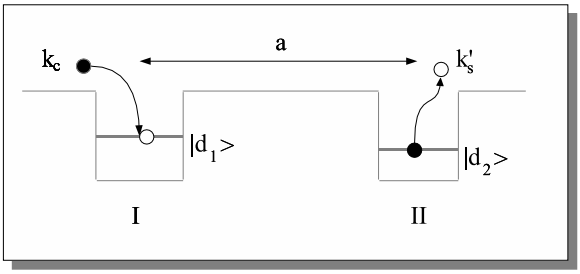

Figure 6.16: Illustration of an Auger transport process. Carrier $|\mathbf{k}_c\rangle$ is captured into dot I, exciting a carrier in dot II out of the dot to the state $|\mathbf{k}'_s\rangle$.

where $\mathbf{k}_c$ and $\mathbf{k}'_s$ are the wave vectors characterizing the captured and the scattered carrier, respectively. $|d_1\rangle$ and $|d_2\rangle$ are the quantum-dot states of the two dots. We write the Coulomb interaction in terms of the interdot distance $\mathbf{a}$,

$$V_c(|\mathbf{r}_s + \mathbf{a} - \mathbf{r}_c|) = \frac{e^2}{4\pi\epsilon_r\epsilon_0|\mathbf{a} + \mathbf{r}_s - \mathbf{r}_c|}, \tag{6.48}$$

where $\mathbf{r}_s$ and $\mathbf{r}_c$ are local position vectors within each quantum dot. If $a >> r_s, r_c, |\mathbf{r}_s - \mathbf{r}_c|$ we can by a very good approximation write the Coulomb interaction in the dipole approximation. We define $\mathbf{v} \equiv \mathbf{r}_s - \mathbf{r}_c$ and write

$$\begin{aligned} \frac{1}{|\mathbf{a}+\mathbf{v}|} &= \frac{1}{(a^2 + v^2 + 2\mathbf{a}\cdot\mathbf{v})^{1/2}} \\ &= \frac{1}{a\left(1 + \frac{v^2+2\mathbf{a}\cdot\mathbf{v}}{a^2}\right)^{1/2}}. \end{aligned} \tag{6.49}$$

A Taylor expansion in $\frac{v^2+2\mathbf{a}\cdot\mathbf{v}}{a^2}$ yields

$$\frac{1}{|\mathbf{a}+\mathbf{v}|} \approx \frac{1}{a}\left(1 - \frac{1}{2}\left(\frac{v^2 + 2\mathbf{a}\cdot\mathbf{v}}{a^2}\right) + \frac{3}{8}\left(\frac{v^2 + 2\mathbf{a}\cdot\mathbf{v}}{a^2}\right)^2\right). \tag{6.50}$$

We retain terms up to second order in (v/a),

$$\begin{aligned}\frac{1}{|\mathbf{a}+\mathbf{v}|} &\approx \frac{1}{a}\left(1-\frac{1}{2}\frac{v^2}{a^2}+\frac{\mathbf{a}\cdot\mathbf{v}}{a^2}+\frac{3}{2}\frac{(\mathbf{a}\cdot\mathbf{v})^2}{a^4}\right)\\ &= \frac{1}{a}\left(1-\frac{1}{2}\frac{r_s^2+r_c^2-2\mathbf{r}_s\cdot\mathbf{r}_c}{a^2}+\frac{(x_s-x_c)}{a}+\frac{3}{2}\frac{x_s^2+x_c^2-2x_sx_c}{a^2}\right).\end{aligned} \tag{6.51}$$

In the last expression we have set $\mathbf{a}\|\hat{x}$. We can drop all terms in which $\mathbf{r}_s$ and $\mathbf{r}_c$ do not couple. The matrix elements of these terms give zero, due to orthogonality of single-particle quantum-dot and wetting-layer wave functions. The terms that give non-zero contributions in the matrix element of Eq. (6.47) are therefore

$$V_c(|\mathbf{r}_s-\mathbf{r}_c|) \longrightarrow \frac{1}{a^3}\left(\mathbf{r}_s\cdot\mathbf{r}_c-3x_sx_c\right). \tag{6.52}$$

We approximate

$$\begin{aligned}|\mathbf{k}_c,d_2\rangle &= |\mathbf{k}_c\rangle|d_2\rangle,\\ |d_1,\mathbf{k}_s'\rangle &= |d_1\rangle|\mathbf{k}_s'\rangle,\end{aligned} \tag{6.53}$$

and the wave functions are written as in Eq. (6.16). The Coulomb matrix element is then given by

$$\begin{aligned}&\langle d_1,\mathbf{k}_s'\,|V_c|\,\mathbf{k}_c,d_2\rangle = \frac{e^2}{4\pi\epsilon_r\epsilon_0}\frac{1}{Sa^3}\\ &\times\Big[\int d^3r_c\Phi_{\mathrm{I}}^*(\mathbf{r}_c)\mathbf{r}_c e^{i\mathbf{k}_c\cdot\boldsymbol{\rho}_c}\Phi_{\mathrm{WL}}(z_s)\int d^3r_s e^{-i\mathbf{k}_s'\cdot\boldsymbol{\rho}_s}\Phi_{\mathrm{WL}}^*(z_s)\mathbf{r}_s\Phi_{\mathrm{II}}(\mathbf{r}_s)\\ &-3\int d^3r_c\Phi_{\mathrm{I}}^*(\mathbf{r}_c)x_c e^{i\mathbf{k}_c\cdot\boldsymbol{\rho}_c}\Phi_{\mathrm{WL}}(z_s)\int d^3r_s e^{-i\mathbf{k}_s'\cdot\boldsymbol{\rho}_s}\Phi_{\mathrm{WL}}^*(z_s)x_s\Phi_{\mathrm{II}}(\mathbf{r}_s)\Big]\\ &\equiv \frac{e^2}{4\pi\epsilon_r\epsilon_0}\frac{1}{a^3}\left[\mathbf{d}_{\mathrm{I},\mathbf{k}_c}\cdot\mathbf{d}_{\mathrm{II},\mathbf{k}_s'}^*-3d_{\mathrm{I},\mathbf{k}_c}^x(d_{\mathrm{II},\mathbf{k}_s'}^x)^*\right],\end{aligned} \tag{6.54}$$

where $\mathbf{d}$ is the dipole moment between quantum-dot and wetting-layer states and d^x is the x-part of the dipole moment. We have defined these dipole moments as

$$\begin{aligned}\mathbf{d}_{\mathrm{I},\mathbf{k}} &\equiv \int d^3r\Phi_{\mathrm{I}}^*(\mathbf{r})\mathbf{r}e^{i\mathbf{k}\cdot\boldsymbol{\rho}}\Phi_{\mathrm{WL}}(z)\\ d_{\mathrm{I},\mathbf{k}}^x &\equiv \int d^3r\Phi_{\mathrm{I}}^*(\mathbf{r})xe^{i\mathbf{k}\cdot\boldsymbol{\rho}}\Phi_{\mathrm{WL}}(z).\end{aligned} \tag{6.55}$$

We wish to get a rough estimation of the capture rate. The Coulomb matrix element is approximated by its value at $\mathbf{k}_c = 0$ and $\mathbf{k}'_s = 0$. A priori its value at this wave vector is expected to be the maximal value. Therefore we get an upper limit for the capture rate in Eq. (6.47). Furthermore we investigate capture into the *ground* state of the quantum dot , i. e. the in-plane quantum-dot wave function fulfills $\Phi_\perp(\boldsymbol{\rho}) = \Phi_\perp(\rho)$. With these assumptions the x and y-parts of the dipole moment give zero and we are left with

$$\begin{aligned}\langle d_1, \mathbf{k}'_s \left| V_c \right| \mathbf{k}_c, d_2 \rangle &\approx \frac{e^2}{4\pi\epsilon_r\epsilon_0}\frac{1}{Sa^3} d^z_{\mathrm{I},\mathbf{k}_c=0}\left(d^z_{\mathrm{II},\mathbf{k}'_s=0}\right)^* \\ &= \frac{e^2}{4\pi\epsilon_r\epsilon_0}\frac{1}{Sa^3}\left|d^z_{\mathrm{I},\mathbf{k}_c=0}\right|^2.\end{aligned} \tag{6.56}$$

The carrier capture rate is given by

$$\begin{aligned}R = &\frac{2\pi}{\hbar}\left(\frac{e^2}{4\pi\epsilon_r\epsilon_0}\right)^2\frac{1}{S^2a^6} \\ &\times\sum_{\mathbf{k}'_s,\mathbf{k}_c}\left|d^z_{\mathrm{I},\mathbf{k}_c=0}\right|^4 f(\epsilon_{k_c})\left(1-f(\epsilon_{k'_s})\right)\delta\left(\frac{\hbar^2 k_s'^2}{2m_s}-\frac{\hbar^2k_c^2}{2m_c}+\Delta E\right),\end{aligned} \tag{6.57}$$

where $\Delta E \equiv E_d^{\mathrm{I}} - E_d^{\mathrm{II}}$ is the energy difference between the quantum-dot energy levels in dots I and II. The summations over the wave vectors $\mathbf{k}'_s$ and $\mathbf{k}_c$ are replaced by integrals. In our approximation the integrand only depends on k'_s and k_c. We can therefore write

$$\sum_{\mathbf{k}'_s,\mathbf{k}_c} \longrightarrow \frac{S^2}{(2\pi)^2}\int dk'_s k'_s \int dk_c k_c, \tag{6.58}$$

where we have integrated over the angles of $\mathbf{k}'_s$ and $\mathbf{k}_c$. Note that the above expression does not include any sum over spin, i. e. the carriers are assumed to have some given spin. We approximate $[1-f(\epsilon_{k'_s})] \approx 1$ and we can easily integrate over k_s due to the δ function. We then get

$$\begin{aligned}R &= \frac{2\pi}{\hbar}\left(\frac{e^2}{4\pi\epsilon_r\epsilon_0}\right)^2\frac{1}{S^2a^6}\frac{S^2}{(2\pi)^2}\left|d^z_{\mathrm{I},\mathbf{k}_c=0}\right|^4\frac{m_s}{\hbar^2}\int dk_c k_c f(\epsilon_{k_c}) \\ &= \frac{m_s}{32\pi^2\hbar^3}\left(\frac{e^2}{\epsilon_r\epsilon_0}\right)^2\frac{\left(d^z_{\mathrm{I},\mathbf{k}_c=0}\right)^4}{a^6}n_{2\mathrm{D}},\end{aligned} \tag{6.59}$$

where we have inserted the expression for the carrier sheet density, $n_{2\mathrm{D}} = 1/\pi \int_0^{+\infty} dk_c k_c f(\epsilon_{k_c})$. We now average over the interdot distances a. We define N_D as the number of dots per unit area. A carrier in a specific dot, which we label I, can interact with $da2\pi aN_D$ carriers in dots that are situated at distance a from dot I, $da2\pi a$ being an infinitesimal surface of a circle with thickness da and radius a. Such averaging certainly assumes also that at least one carrier occupies each dot. The average rate becomes

$$R = \int_{2r_0}^{+\infty} da2\pi aN_D R_a, \tag{6.60}$$

where R_a is the rate from Eq. (6.59) for a second dot, II, at a distance **a** from dot I. r_0 is the dot size so that $2r_0$ is the minimal interdot distance. In principle we should also average over the dot sizes. This could be an average over ΔE which then would reflect the dot sizes in some manner. In our estimate we will assume that the dots are identical and will therefore not perform this average. The average over **a** yields the rate

$$R = \frac{m_s}{1024\pi\hbar^3}\left(\frac{e^2}{\epsilon_r\epsilon_0}\right)^2 N_D \left(\frac{d^z_{\mathrm{I},\mathbf{k}_c=0}}{r_0}\right)^4 n_{2\mathrm{D}}. \tag{6.61}$$

We estimate the in-plane part of the z dipole moment to be $\sqrt{\pi}r_0$, i. e. on the order of the in-plane radius. We are thus left with

$$R = \frac{\pi m_s}{1024\hbar^3}\left(\frac{e^2}{\epsilon_r\epsilon_0}\right)^2 N_D d_z^4 n_{2\mathrm{D}}, \tag{6.62}$$

where $d_z = \int dz\Phi_z^*(z)z\Phi_{\mathrm{WL}}(z)$ is the dipole moment in the z-direction, involving only the $z-$part of the quantum-dot and wetting-layer wave functions. We see that the transport rate R is very dependent upon the magnitude of d_z. In Fig. 6.17 we plot the transport rate versus d_z.

We now estimate the z dipole moment. Actually if we assume that the quantum dot is a cylinder with infinite confinement and the wetting layer is approximated, as before, as a thin quantum well with finite confinement we get $d_z = 0.8$ nm. We have set $V_e = 500$ meV and wetting-layer thickness $d = 1$ nm in this estimation. From Figure 6.17 we see that this would correspond to a transport time $R^{-1} = 200$ ns! Even though we use somewhat more elaborate wave functions such as the variational wave functions used in previously in this chapter (see Appendix D) we get $d_z = 0.7 - 1$ nm for

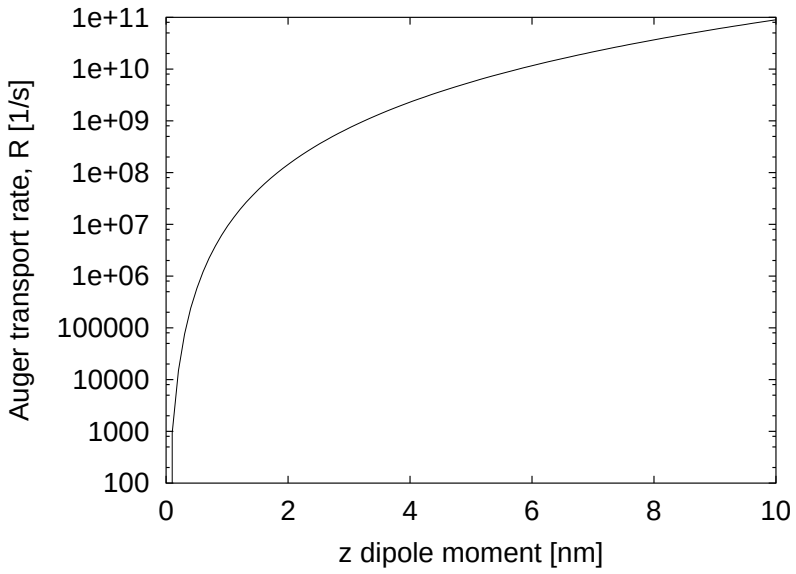

Figure 6.17: Dependence of the Auger transport rate on the dipole moment in the z-direction. We use $m_s = 0.07m_e$, $\epsilon_r = 12.5$ (GaAs), $N_D = 10^{15}\mathrm{m}^{-2}$ and $n_{2\mathrm{D}} = 10^{15}\mathrm{m}^{-2}$.

quantum-dot height ranging between 3 and 10 nm for in-plane radius $r_0 =$ 10 nm. Looking at Figure 6.17 it is seen that this corresponds to a minimum transport time of 100 ns. We therefore conclude that this kind of Auger transport process does not seem to be very efficient. Indeed if the curve in Figure 6.17 is extrapolated to larger dipole moments a transport time of about 10 ps is reached only if the dipole moment is about 10 nm! Even the intradot dipole moment $\int dz|\Phi_z(z)|^2 z$ is less than 2 nm for quantum-dot heights from 3 to 10 nm calculated with the variational wave functions. In the present structure dipole moments between quantum-dot and wetting-layer wave functions of the order 10 nm are very unlikely to ever be obtained due to a small extension of the wetting-layer wave function and localization of the quantum-dot wave function.

6.6 Summary

In this chapter we have calculated Auger carrier capture rates into quantum dots mediated by the Coulomb interaction of two carriers in the wetting

layer. As a result of this interaction one carrier is captured into a quantum dot while another is promoted to a higher energy in the wetting layer. The geometry dependence of such capture processes was studied in detail and the behavior of Auger coefficients was identified in terms of wave-function overlaps.

Auger capture processes were compared to single-phonon-assisted capture processes at quantum-dot geometries where these phonon-assisted processes are energetically allowed. It was shown that Auger capture rates exceed phonon-assisted capture rates only at relatively high carrier sheet densities, single-phonon capture rates at $n_{2D} \sim 10^{16}\mathrm{m}^{-2}$ and two-phonon capture rates at $n_{2D} \sim 10^{15}\mathrm{m}^{-2}$. The highest carrier densities attained in rate-equation simulations for quantum-dot amplifiers are on the order $n_{3D} \approx 10^{24}\mathrm{m}^{-3}$ [81] which translates into a carrier sheet density $n_{2D} = 10^{15}\mathrm{m}^{-2}$ for 1 nm thick wetting layer and lower for thinner wetting layer. It thus seems that phonon-assisted capture processes are the dominant ones *at dot sizes where they are energetically allowed* but these dot-size intervals seem to be rather narrow. However, we pointed out that the Auger processes that we investigated are energetically allowed irrespective of the dot geometry, as long as there are bound states in the dot. The efficiency of these processes depends therefore to a large extent on the energy-level separation between the wetting-layer band edge and the quantum-dot state to which the capture takes place.

A simplified model similar to the one presented in Ref. [38] was developed and compared to the more elaborate model that was presented in section 6.1. While this simplified model is useful in understanding the physical aspects of Auger carrier capture rates, it is very approximate in that dependence of the Coulomb matrix element on wetting-layer wave vectors is neglected and this gives (unnecessarily) rather approximate results.

Our results were obtained under the assumption that wave functions for quantum-dot and wetting-layer systems were obtained by separate solutions; quantum-dot functions were found for a combined quantum-dot and wetting-layer system whereas wetting-layer wave functions were determined without taking the presence of the quantum dot into account. We investigated the influence of orthogonalization of the wetting-layer states to the quantum-dot ground state in the dot size range where only one state

is bound in the dot. It seems that the capture rate decreases by one order of magnitude due to the orthogonalization. We however pointed out that wetting-layer states and quantum-dot states can be orthogonalized with different methods. These methods are to some extent "arbitrary" in that different methods give different wetting-layer states. An orthogonalization of wetting-layer states to quantum-dot states can furthermore give wetting-layer states that are not orthogonal to each other. This subject needs to be addressed in the near future.

We have also investigated a transport mechanism mediated by Auger processes in which a carrier in the vicinity of a quantum dot interacts with a quantum-dot carrier in another dot promoting the latter carrier out of the dot while the former one is captured into the first dot. This process was shown to be very inefficient.

Chapter 7

Summary and outlook

In this thesis, calculations of carrier relaxation in quantum-dot structures, with emphasis on carrier capture into quantum dots, have been presented and discussed.

Calculations of phonon-mediated capture processes were presented in chapter 3. Capture by emission of one or two LO phonons was investigated and the dependence of these processes on quantum-dot size, temperature and carrier density in the barrier was studied. Single-phonon mediated capture rates were shown to be on the subpicosecond scale for carrier densities of 10^{17} cm^{-3}. Two-phonon mediated capture processes were calculated to energy levels that are lying too deep to be attained in a single-phonon process. Capture rates were found to be at most one order of magnitude lower than single-phonon capture rates for the same carrier density in the barrier. Two-phonon capture rates were calculated using second-order perturbation theory. In the expression for the two-phonon capture rate, a sum over *intermediate states* appears. We showed that an interference pattern between the different intermediate states occurs and that it can be quite complicated for many states bound to the dot. In the sum, denominators that express the energy difference between the initial and the intermediate states occurs. It was shown that the sign of this denominator plays a crucial role in the interference pattern. Furthermore, in the case of intermediate states in the discrete part of the energy spectrum, a good wave-function overlap of an intermediate state with the final state can increase the capture rate. Such an enhancement was identified.

In the case of single-phonon capture into a quantum dot, the influence of the presence of a charge in the quantum-dot state to which the capture takes place, was investigated in chapter 4. The order of magnitude for carrier capture rates was shown to be of the same order as in the case of carrier capture into an empty dot state. In the case where the incident carrier and the quantum-dot carrier are of a different type, it was however shown that the dot size interval, in which the capture process is energetically allowed, is considerably reduced in comparison to capture into an empty dot state. This arises due to the large binding energy of the final bound electron-hole state that is an appreciable fraction of the LO phonon energy. In the case where the two carriers are of the same type, two electrons or two holes, there are three possible final states due to the particles' mutual Coulomb interaction. The dot-size intervals, for which the capture is allowed, is shifted depending on the final state. This shift is however not significant and the dot size interval is very similar to capture into an empty dot.

In chapter 5, carrier-LO phonon interaction of carriers in quasi-bound quantum-dot states was investigated. Starting with a discussion of the carrier-LO phonon interaction of carriers in discrete quantum-dot states, the scene was set, because interaction of carriers in quasi-bound states with LO phonons is in many aspects similar to the case of carriers in discrete states. It was shown that carriers in discrete states interact strongly with LO phonons. Owing to the strong interaction, entities constituted of both carriers and phonons - polarons - are formed. Two polaron levels were shown to exist. The notion of irreversible carrier relaxation by phonon emission are not applicable to polarons because such relaxation is a result of a perturbative treatment of the carrier-LO phonon interaction. Instead, polarons relax due to the anharmonic decay of the phonons. For carriers in quasi-bound quantum-dot states it was shown that strong coupling *can* occur when the quasi-bound level is separated by one LO phonon energy, or thereabout, from a discrete quantum-dot state. In the case where the quasi-bound state is very close in energy to the onset of the continuum, the lower polaron level was shown to become a discrete state and the relaxation of the state to the ground state was calculated to be only a few picoseconds. The investigation here was performed under the assumption that the quantum dot has spherical symmetry. An intriguing question is the influence of quantum-dot geometry on the quasi-bound states and whether such states may have an impact in self-assembled dot structures. It would be interest-

ing to know how sharp they can be in these systems where the symmetry is low. Such investigations are quite complicated in that they probably require numerical investigations of the combined quantum-dot/wetting-layer system.

Carrier capture processes of the Auger type were studied in chapter 6. We investigated the process where the Coulomb interaction of two wetting-layer carriers leads to the capture of one carrier to the dot while the other carrier is excited to a higher energy in the wetting layer. Carrier capture rates were shown to decrease with increasing energy level separation, ΔE, between the wetting-layer band edge and the quantum-dot level to which the capture takes place. The capture rates to the ground and first-excited states were calculated and they were found to be nearly identical when plotted as a function of ΔE. Capture with scattering of electrons were shown to be more efficient than capture with scattering of holes.

Our results were obtained under the assumption that wave functions for quantum-dot and wetting-layer systems were obtained by separate solutions; quantum-dot functions were found for a combined quantum-dot and wetting-layer system whereas wetting-layer wave functions were determined without taking the presence of the quantum dot into account. We investigated the influence of orthogonalization of the wetting-layer states to the ground state in the dot size range where only one state is bound in the dot. With the choice of orthogonalization, the capture rate was shown to decrease by one order of magnitude due to the orthogonalization. It was pointed out that other orthogonalization methods can also give wetting-layer states that are orthogonal to the dot states. In this respect, these methods cannot be fully trusted. An orthogonalization of wetting-layer states to quantum-dot states can furthermore give wetting-layer states that are not orthogonal to each other. Probably, a numerical investigation of the combined quantum-dot and wetting-layer system needs to be put forward to shed more light on the subject.

Capture mediated by Coulomb scattering were compared to single-phonon capture. Coulomb-mediated capture processes of the type that we investigated are always energetically allowed whereas there is a small range of dot sizes where phonon-mediated capture is energetically allowed. Emission by more than one LO phonon gives larger dot size intervals be-

cause the energy difference between the wetting-layer band edge and the quantum-dot state can be larger. At resonance, i. e., at dot sizes where single-phonon capture is energetically allowed, phonon-mediated capture rates were shown to exceed largely Coulomb-mediated capture rates. We showed in chapter 3 that two-phonon mediated capture rates are at most one order of magnitude larger than single-phonon capture rates. Capture by emission of more than two LO phonons have to date not been calculated. However, in view of the trends in the capture rates when going from single-phonon to two-phonon emission (from first- to second-order perturbation), capture rates by multiphonon emission are expected to be lowered with increasing number of emitted phonons. The efficiency of Coulomb- versus phonon-mediated capture can therefore depend largely on the energy level spacing between the wetting-layer band edge and the higher lying dot levels, which, in self-assembled quantum-dot structures, varies due to the inhomogeneous broadening. Therefore, a quantitative comparison of Coulomb- and phonon-mediated capture could be made in a rate-equation model, where the processes are simply related to the energy level spacing between the wetting-layer band edge and the dot levels. This could give a good understanding of the capture processes that are involved and should be the subject of a further investigation of the matter. In general, the quest of including microscopic calculations, such as the ones presented in this thesis, into macroscopic models, such as the rate-equation models that we discussed in chapter 2, is a challenging but necessary task for the understanding of the carrier dynamics in quantum-dot structures in a more fundamental manner.

Appendix A

Carrier-LO phonon interaction

The electron-phonon interaction in crystals is an interaction of vibrational modes with conduction electrons. In polar materials, such as III-V and II-VI compounds, the vibrations of oppositely charged ions give rise to long range electric fields and the field interaction with electrons is the dominant scattering mechanism [9]. A schematic of two oppositely charged ions in the presence of an electron is shown in Fig. A.1. In the following, we derive the Hamiltonian for the carrier-LO phonon interaction that is often referred to as the Fröhlich interaction. To this end, the effective charge of the ions, shown schematically in Fig. A.1, needs to be determined.

A.1 The effective charge

The effective charge of the ions can be found by using the fact that at high frequencies, the ion contribution from the heavy ions to the polarization vanishes. In the static case, both ions and electrons contribute to the polarization. The equation of motion for the ion displacement (phonons) is

$$\mu\left(\frac{\partial^2\mathbf{X}}{\partial t^2}+\omega_{\mathbf{q}}^2\mathbf{X}\right)=\mathbf{F}, \tag{A.1}$$

where μ is the effective mass of the ions, $\mathbf{X}$ is the relative ion displacement, $\omega_{\mathbf{q}}$ is the oscillation frequency and $\mathbf{F}$ is an external force. If we assume that the external force is the force due to a nearby electron, we have that

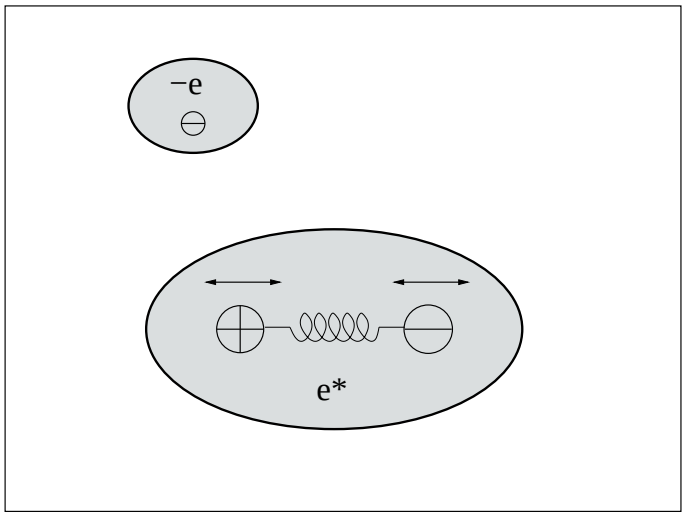

Figure A.1: A schematic of two oscillating oppositely charged ions and a nearby electron. The ions' effective charge is e^*.

$\mathbf{F} = e^*\mathbf{D}/\epsilon_0$, where e^* is the ion effective charge and $\mathbf{D}$ is the electric displacement. This relative motion gives rise to a polarization

$$\mathbf{P} = \frac{e^*}{V_0}\mathbf{X}, \tag{A.2}$$

where V_0 is the volume of a unit cell and e^*/V_0 is therefore the effective ion charge per unit cell. We can rewrite the equation of motion (A.1) using (A.2) and the expression for the electric force as

$$\frac{\mu V_0}{e^*}\left(\frac{\partial^2\mathbf{P}}{\partial t^2} + \omega_{\mathbf{q}}^2\mathbf{P}\right) = \frac{e^*}{\epsilon_0}\mathbf{D}, \tag{A.3}$$

In the static case ($\partial^2\mathbf{P}/\partial t^2 = 0$) the polarization due to the ion motion is given by

$$\mathbf{P} = \frac{e^{*2}}{\mu V_0 \omega_{\mathbf{q}}^2 \epsilon_0}\mathbf{D}. \tag{A.4}$$

The total polarization due to both electron and ion motion in the static case is given by

$$\mathbf{P}_0 = \mathbf{D} - \epsilon_0\mathbf{E} = \left(1 - \frac{1}{\epsilon_r}\right)\mathbf{D}, \tag{A.5}$$

where ϵ_r is the static permittivity. At high frequencies, the polarization due to ion motion vanishes and only the electron motion contributes to the polarization. In this case we have

$$\mathbf{P}_\infty = \left(1 - \frac{1}{\epsilon_\infty}\right)\mathbf{D}. \tag{A.6}$$

The polarization due to ion motion only is obtained by subtracting $\mathbf{P}_\infty$ from $\mathbf{P}_0$,

$$\mathbf{P} = \mathbf{P}_0 - \mathbf{P}_\infty = \mathbf{D}\left(\frac{1}{\epsilon_\infty} - \frac{1}{\epsilon_r}\right) \tag{A.7}$$

The effective charge of the ions, e^*, can now be deduced by equating Eqs. (A.4) and (A.7)

$$e^{*2} = \frac{\mu V_0 \omega_{\mathbf{q}}^2 \epsilon_0}{\epsilon^*}, \tag{A.8}$$

where we have defined

$$\frac{1}{\epsilon^*} = \left(\frac{1}{\epsilon_\infty} - \frac{1}{\epsilon_r}\right). \tag{A.9}$$

A.2 The Fröhlich interaction

We assume local charge neutrality, i. e. that $\mathbf{D} = 0$. We can therefore find the internal field associated with the ionic displacements from $\mathbf{D} = \epsilon_0\mathbf{E}+\mathbf{P}$,

$$\begin{aligned}\mathbf{E} &= -\frac{1}{\epsilon_0}\mathbf{P} \\ &= -\frac{e^*}{\epsilon_0 V_0}\mathbf{X},\end{aligned} \tag{A.10}$$

where the latter expression is obtained from Eq. (A.2). The displacement can be written in terms of plane waves as [9]

$$\mathbf{X} = \frac{1}{\sqrt{N}}\sum_{\mathbf{q}}\left(Q_{\mathbf{q}}\hat{\mathbf{e}}_{\mathbf{q}}e^{-i\mathbf{q}\cdot\mathbf{r}} + c.c.\right), \tag{A.11}$$

where $Q_{\mathbf{q}}$ are normal coordinates, $\hat{\mathbf{e}}_{\mathbf{q}}$ is a unit polarization vector, N is the number of unit cells in the crystal and $\mathbf{q}$ is the phonon wave vector. The internal field thus becomes

$$\mathbf{E} = -\frac{e^*}{\epsilon_0 V_0\sqrt{N}}\sum_{\mathbf{q}}\left(Q_{\mathbf{q}}\hat{\mathbf{e}}_{\mathbf{q}}e^{i\mathbf{q}\cdot\mathbf{r}} + c.c.\right). \tag{A.12}$$

This internal field, **E**, can be written as the gradient of the potential that arises due to the relative motion of the ions,

$$\mathbf{E} = -\nabla U_{\rm ph}. \tag{A.13}$$

$U_{\rm ph}$ can now easily be found, by using $\nabla(e^{i\mathbf{q}\cdot\mathbf{r}}) = iq\hat{\mathbf{e}}_{\mathbf{q}}e^{i\mathbf{q}\cdot\mathbf{r}}$,

$$U_{\rm ph} = \frac{e^*}{\epsilon_0 V_0\sqrt{N}}\sum_{\mathbf{q}}\left(\frac{-iQ_{\mathbf{q}}}{q}e^{i\mathbf{q}\cdot\mathbf{r}} + c.c.\right). \tag{A.14}$$

This interaction can be written in second quantization by writing the normal coordinates in terms of the phonon creation and annihilation operators, $\hat{a}^\dagger_{\mathbf{q}}$ and $\hat{a}_{\mathbf{q}}$, according to

$$Q_{\mathbf{q}} = \sqrt{\frac{\hbar}{2\mu\omega_{\mathbf{q}}}}\hat{a}_{\mathbf{q}}. \tag{A.15}$$

The potential becomes

$$\begin{aligned} U_{\rm ph} &= \frac{e^*}{\epsilon_0 V_0\sqrt{N}}\sqrt{\frac{\hbar}{2\mu\omega_{\mathbf{q}}}}i\sum_{\mathbf{q}}\frac{1}{q}\left(e^{-i\mathbf{q}\cdot\mathbf{r}}\hat{a}^\dagger_{\mathbf{q}} - e^{i\mathbf{q}\cdot\mathbf{r}}\hat{a}_{\mathbf{q}}\right) \\ &= \sqrt{\frac{\hbar\omega_{\rm LO}}{2\epsilon_0\epsilon^*\Omega}}i\sum_{\mathbf{q}}\frac{1}{q}\left(e^{-i\mathbf{q}\cdot\mathbf{r}}\hat{a}^\dagger_{\mathbf{q}} - e^{i\mathbf{q}\cdot\mathbf{r}}\hat{a}_{\mathbf{q}}\right), \end{aligned} \tag{A.16}$$

where the latter expression was obtained by inserting the ion effective charge from Eq. (A.8). We have set $\omega_{\mathbf{q}} = \omega_{\rm LO}$ in the last expression, since the LO phonons are (almost) dispersionless. $\Omega = NV_0$ is the quantization volume. The Fröhlich Hamiltonian for the electron-phonon interaction is given by $H_{\text{e-ph}} = -eU_{\rm ph}$ ($-e$ is the electron charge),

$$H_{\rm e-ph} = -e\sqrt{\frac{\hbar\omega_{\rm LO}}{2\epsilon_0\epsilon^*\Omega}}i\sum_{\mathbf{q}}\frac{1}{q}\left(e^{-i\mathbf{q}\cdot\mathbf{r}}\hat{a}^\dagger_{\mathbf{q}} - e^{i\mathbf{q}\cdot\mathbf{r}}\hat{a}_{\mathbf{q}}\right). \tag{A.17}$$

We define

$$\alpha(q) \equiv \frac{\alpha_0}{q}, \tag{A.18}$$

where

$$\alpha_0 = -e\sqrt{\frac{\hbar\omega_{\rm LO}}{2\epsilon_0\epsilon^*\Omega}}i, \tag{A.19}$$

and rewrite Eq. (A.17) as

$$H_{\rm e-ph} = \sum_{\mathbf{q}}\left[\alpha(q)e^{-i\mathbf{q}\cdot\mathbf{r}}\hat{a}^\dagger_{\mathbf{q}} + \alpha^*(q)e^{i\mathbf{q}\cdot\mathbf{r}}\hat{a}_{\mathbf{q}}\right]. \tag{A.20}$$

Appendix B

Derivation of probability in one- and two-phonon capture

In the following, we derive the transition probabilities that a carrier is captured from the continuum into the quantum dot via emission of one or two phonons. The transition probability for the single-phonon capture process can be derived from first-order perturbation theory. However, for the two-phonon capture process, the first order term is zero and the transition probability is in this case found with second-order perturbation theory. We derive probabilities for transition between two states and express two-phonon capture probabilities using Fermi's golden rule and the derived probability.

B.1 Perturbation formulas

The derivation of a solution to Schrödinger's equation under the action of a perturbation can be found in many textbooks on quantum mechanics. It is given here to facilitate the reading of the following sections. The derivation here is taken from Ref. [37]. We assume that the eigenstates and eigenenergies for the unperturbed Hamiltonian are known;

$$H_0|\phi_n\rangle = E_n|\phi_n\rangle. \tag{B.1}$$

The system is assumed to be in the state $|\phi_i\rangle$ at $t = -\infty$, so that

$$H_0|\phi_i\rangle = E_i|\phi_i\rangle. \tag{B.2}$$

We wish to determine the probability that the carrier is found in a state $|\phi_f\rangle$ at time t under the action of a perturbation $V(t) = \lambda\hat{V}(t)$, where $\hat{V}(t)$ is an observable and $\lambda << 1$. The Schrödinger equation

$$i\hbar\frac{\mathrm{d}}{\mathrm{dt}}|\psi(t)\rangle = [H_0 + V(t)]\,|\psi(t)\rangle \tag{B.3}$$

along with the initial condition

$$|\psi(t=0)\rangle = |\phi_i\rangle \tag{B.4}$$

determines this probability. This probability can be written

$$P_{if}(t) = |\langle\phi_f|\psi(t)\rangle|^2. \tag{B.5}$$

We expand the wave function $|\psi(t)\rangle$ in the basis $\{|\phi_n\rangle\}$

$$|\psi(t)\rangle = \sum_n a_n(t)|\phi_n\rangle \tag{B.6}$$

and insert it into Eq. (B.3). We project onto the state $|\phi_k\rangle$ and obtain

$$i\hbar\frac{\mathrm{d}}{\mathrm{dt}}a_k(t) = E_k a_k(t) + \sum_n V_{kn}(t)a_n(t). \tag{B.7}$$

If $V(t) = 0$, the solution to (B.7) is given by

$$a_k(t) = b_k \exp\left(-iE_k t/\hbar\right). \tag{B.8}$$

If $V(t)$ is non-zero and since we assume that $V(t)$ is much smaller than H_0, we can expect that the solution to (B.7) remains similar to the solution (B.8). We therefore set

$$a_k(t) = b_k(t) \exp\left(-iE_k t/\hbar\right). \tag{B.9}$$

This is substituted into Eq. (B.7). We obtain

$$i\hbar \exp\left(-iE_k t/\hbar\right)\frac{\mathrm{d}}{\mathrm{dt}}b_k(t) = \sum_n V_{kn}(t)b_n(t)\exp\left(-iE_n t/\hbar\right). \tag{B.10}$$

We now multiply by the factor $\exp(iE_k t/\hbar)$ and introduce the Bohr frequency

$$\omega_{kn} = \frac{E_k - E_n}{\hbar}, \tag{B.11}$$

which now yields

$$i\hbar \frac{\mathrm{d}}{\mathrm{dt}} b_k(t) = \sum_n e^{i\omega_{kn}t} V_{kn}(t) b_n(t). \tag{B.12}$$

The coefficients $b_k(t)$ are then written as a power series in λ

$$b_k(t) = \sum_{r=0}^{+\infty} b_k^{(r)}(t)\lambda^r. \tag{B.13}$$

By inserting this expansion into Eq. (B.12) and equating coefficients of λ^r on each side, the following is obtained:

$$\begin{aligned} i\hbar \frac{\mathrm{d}}{\mathrm{dt}} b_k^{(0)}(t) &= 0, \qquad (r=0), \\ i\hbar \frac{\mathrm{d}}{\mathrm{dt}} b_k^{(r)}(t) &= \sum_n e^{i\omega_{kn}t} \hat{V}_{kn}(t) b_n^{(r-1)}(t), \qquad (r>0). \end{aligned} \tag{B.14}$$

B.1.1 First order perturbation

The solution to $b_k^{(0)}(t)$ is a constant determined by the initial condition $b_k^{(0)}(t=0) = \delta_{ki}$. In general, the solution for $b_k^{(r)}(t)$ is found from $b_k^{(r-1)}(t)$ via (B.14). To first order, the solution is

$$b_k^{(1)}(t) = \frac{1}{i\hbar} \int_{-\infty}^{t} e^{i\omega_{ki}t'} \hat{V}_{ki}(t') dt'. \tag{B.15}$$

We regard the perturbation as being adiabatically applied according to

$$\hat{V}(t) \to e^{\epsilon t} \hat{V} \tag{B.16}$$

with $\epsilon \to 0$ [83]. The solution for $b_k^{(1)}(t)$ is then found to be

$$b_k^{(1)}(t) = -\frac{\hat{V}_{ki}}{\hbar} \frac{e^{(i\omega_{ki}+\epsilon)t}}{\omega_{ki} - i\epsilon}. \tag{B.17}$$

In particular, the probability per unit time that the system is found in state $|\phi_f\rangle$ at time t is

$$\begin{aligned} P_{if}(t) &= \frac{\mathrm{d}}{\mathrm{dt}}|b_f^{(1)}(t)|^2. \\ &= \lim_{\epsilon\to 0}\frac{|\hat{V}_{fi}|^2}{\hbar^2}\frac{2\epsilon e^{2\epsilon t}}{\omega_{fi}^2+\epsilon^2}. \end{aligned} \tag{B.18}$$

We make use of the relation [37]

$$\lim_{\epsilon\to 0}\frac{2\epsilon}{x^2+\epsilon^2} = 2\pi\delta(x). \tag{B.19}$$

With this relation, the probability becomes

$$\begin{aligned} P_{if}(t) &= 2\pi\frac{|\hat{V}_{fi}|^2}{\hbar^2}\delta(\omega_{fi}) \\ &= \frac{2\pi}{\hbar}|\hat{V}_{fi}|^2\delta(E_f-E_i). \end{aligned} \tag{B.20}$$

In the last expression, we have used that $\omega_{fi} = (E_f - E_i)/\hbar$ and $\delta(ax) = (1/a)\delta(x)$.

B.1.2 Second-order perturbation

If the matrix element $\hat{V}_{fi}$ is zero, one needs to evaluate the probability to second order. We have, from the secular equation (B.14), that b_f can be found to second order when the solution to zeroth and first order is known. We have that

$$i\hbar\frac{\mathrm{d}}{\mathrm{dt}}b_f^{(2)}(t) = \sum_\nu e^{i\omega_{f\nu}t}\hat{V}_{f\nu}(t)b_\nu^{(1)}(t). \tag{B.21}$$

We have the expression for $b_\nu^{(1)}(t)$ from Eq. (B.17) that, inserted into (B.21), gives

$$i\hbar\frac{\mathrm{d}}{\mathrm{dt}}b_f^{(2)}(t) = -\frac{1}{\hbar}\sum_\nu e^{i\omega_{f\nu}t}\hat{V}_{f\nu}\hat{V}_{\nu i}\frac{e^{(i\omega_{\nu i}+2\epsilon)t}}{\omega_{\nu i}-i\epsilon} \tag{B.22}$$

This first order differential equation can easily be solved, yielding

$$b_f^{(2)}(t) = \frac{1}{\hbar^2}\sum_\nu\frac{\hat{V}_{f\nu}\hat{V}_{\nu i}}{(\omega_{\nu i}-i\epsilon)(\omega_{fi}-2i\epsilon)}e^{(i\omega_{fi}+2\epsilon)t}, \tag{B.23}$$

and the probability per unit time that the system is in state $|\phi_f\rangle$ at time t is given by

$$P_{if}(t) = \lim_{\epsilon \to 0} \frac{\mathrm{d}}{\mathrm{dt}} |b_f^{(2)}(t)|^2 \tag{B.24}$$

$$= \frac{2\pi}{\hbar} \left| \sum_{\nu} \frac{\hat{V}_{f\nu} \hat{V}_{\nu i}}{E_\nu - E_i} \right|^2 \delta(E_f - E_i), \tag{B.25}$$

where we have used Eq. (B.19). The states, for which $\hat{V}_{f\nu}$ and $\hat{V}_{\nu i}$ are different from zero, are referred to as *intermediate* states.

B.2 Two-phonon capture

In the case of a two-phonon capture process, the transition probability is zero to first order in the Fröhlich Hamiltonian if we assume that the phonon populations in the initial and final states differ by two. We assume therefore that a carrier with wave vector $\mathbf{k}$ is captured by emitting phonons with *given* wave vectors $\mathbf{q}_1$ and $\mathbf{q}_2$ and we determine the transition probability with second-order perturbation theory (Eq. (B.25)).

$$w(\mathbf{k}, \mathbf{q}_1, \mathbf{q}_2) = \frac{2\pi}{\hbar} \Big| \sum_{\nu} \frac{\hat{V}^{\mathrm{em}}_{\mathrm{f}\nu} \hat{V}^{\mathrm{em}}_{\nu \mathrm{i}}}{E_i - E_\nu} \Big|^2 \delta(E_f - E_i). \tag{B.26}$$

Note that the above formula should, according to Fermi's golden rule, include an average over initial phonon modes and a sum over final phonon modes. We do not do this here. Instead we replace phonon populations by their average in the final result. The Hamiltonian for emission of two phonons is given by

$$\hat{V}^{\mathrm{em}}(\mathbf{q}_1, \mathbf{q}_2) = \alpha(q_1) e^{-i\mathbf{q}_1 \cdot \mathbf{r}} \hat{a}^\dagger_{\mathbf{q}_1} + \alpha(q_2) e^{-i\mathbf{q}_2 \cdot \mathbf{r}} \hat{a}^\dagger_{\mathbf{q}_2} \tag{B.27}$$

and E_i (E_ν) is the energy of the initial (intermediate) state. In this two-phonon capture process, the carrier relaxes through an intermediate state, $|\nu\rangle$, where its electronic part is either a state in the continuous part of the energy spectrum $|\mathbf{k}_\nu\rangle$, or a discrete quantum-dot state, $|d_\nu\rangle$, hereafter labeled $|\zeta_\nu\rangle$. The states involved in the process are labeled as follows

$$\begin{aligned} |i\rangle &= |\mathbf{k}\rangle |\{n^i_{\mathbf{q}}\}\rangle, \\ |f\rangle &= |d\rangle |\{n^f_{\mathbf{q}}\}\rangle, \\ |\nu\rangle &= |\zeta_\nu\rangle |\{n^\nu_{\mathbf{q}}\}\rangle. \end{aligned} \tag{B.28}$$

We assume that the phonons are emitted into two *different* phonon modes, that we label $\mathbf{q}_1$ and $\mathbf{q}_2$, so that the initial and final phonon states differ only in the number of phonons in modes $\mathbf{q}_1$ and $\mathbf{q}_2$,

$$n^f_{\mathbf{q}_1} = n^i_{\mathbf{q}_1} + 1, \tag{B.29}$$

$$n^f_{\mathbf{q}_2} = n^i_{\mathbf{q}_2} + 1. \tag{B.30}$$

It can be shown that contribution from phonons emitted into the same mode is negligible. If we assume that the wave vector of the first emitted phonon is $\mathbf{q}_1$, so that

$$n^\nu_{q_1} = n^i_{q_1} + 1, \tag{B.31}$$

the transition matrix element from $|i\rangle$ to $|\nu\rangle$ is given by

$$V^{\mathrm{em}}_{\nu i} = \langle\{n^\nu_{\mathbf{q}}\}|\langle\zeta_\nu|\hat{V}^{\mathrm{em}}|\mathbf{k}\rangle|\{n^i_{\mathbf{q}}\}\rangle \tag{B.32}$$

$$= \langle\{n^\nu_{\mathbf{q}}\}|\langle\zeta_\nu|\alpha(q_1)e^{-i\mathbf{q}_1\cdot\mathbf{r}}\hat{a}^\dagger_{\mathbf{q}_1}|\mathbf{k}\rangle|\{n^i_{\mathbf{q}}\}\rangle \tag{B.33}$$

$$= \sqrt{n_{q_1}+1}\alpha(q_1)\langle\zeta_\nu|e^{-i\mathbf{q}_1\cdot\mathbf{r}}|\mathbf{k}\rangle, \tag{B.34}$$

$$= \sqrt{n_{q_1}+1}\alpha(q_1)M^{q_1}_{\nu i}, \tag{B.35}$$

where n_{q_1} is the population of phonon mode with wave vector $\mathbf{q}_1$. Correspondingly, the transition matrix element from $|\nu\rangle$ to $|f\rangle$ is given by

$$V_{f\nu} = \sqrt{n_{q_2}+1}\alpha(q_2)\langle d|e^{-i\mathbf{q}_2\cdot\mathbf{r}}|\zeta_\nu\rangle, \tag{B.36}$$

$$= \sqrt{n_{q_2}+1}\alpha(q_2)M^{q_2}_{f\nu}. \tag{B.37}$$

It is of course also possible to label the phonon vectors in the reverse order, such that the sum over intermediate states consists of two contributions. The transition probability then becomes

$$w(\mathbf{k},\mathbf{q}_1,\mathbf{q}_2) = \frac{2\pi}{\hbar}(\overline{n}+1)^2 \times \left|\sum_\nu \alpha(q_1)\alpha(q_2)\frac{M^{q_2}_{f\nu}M^{q_1}_{\nu i} + M^{q_1}_{f\nu}M^{q_2}_{\nu i}}{\epsilon_k - \epsilon_\nu - \hbar\omega_{LO}}\right|^2 \delta(E_f - E_i), \tag{B.38}$$

where $\epsilon_{\mathbf{k}}$ (ϵ_ν) is the energy of the initial (intermediate) carrier state. It should be noted here that a discrete quantum-dot intermediate carrier state can be the same as the final carrier state, since the matrix elements $M^{q_i}_{ff}$, $i = 1, 2$, are in general non-zero. Here we have replaced n_{q_i}, $i = 1, 2$, with the average population $\overline{n}$ which arises from the average over initial phonon modes.

Appendix C

Bound states in a spherical quantum dot

The confinement potential is described by

$$V(\mathbf{r}) = \begin{cases} 0 & r \leq a, \\ V_0 & r > a, \end{cases} \tag{C.1}$$

where $V_0 > 0$. The total wave function can be separated as follows;

$$\Psi_d(\mathbf{r}) = Y_\ell^m(\theta, \phi)\chi_\ell(r), \tag{C.2}$$

because the confinement potential is spherically symmetric, $V(\mathbf{r}) = V(r)$. Y_ℓ^m are the spherical harmonics and the radial part, χ_ℓ, is found to be a spherical Bessel function of the form

$$\chi_\ell(r) = \begin{cases} a_\ell j_\ell(\alpha r) & r \leq a, \\ b_\ell h_\ell^{(+)}(i\beta r) & r > a. \end{cases} \tag{C.3}$$

The spherical Hankel functionsl $h_\ell^\pm$ are defined by

$$h_l^{(+)}(\rho) = i\left(j_\ell(\rho) + i n_l(\rho)\right) \tag{C.4}$$

$$h_l^{(-)}(\rho) = -i\left(j_\ell(\rho) - i n_l(\rho)\right), \tag{C.5}$$

where j_ℓ is the spherical Bessel function and n_l the spherical Neumann function. The spherical Bessel- and Neumann functions are defined in the usual way (see e. g. Ref. [84]). α and β are related according to

$$(\alpha a)^2 + (\beta a)^2 = \frac{2m^*}{\hbar^2} V_0, \tag{C.6}$$

where V_0 is the confinement potential strength and m^* is the carrier effective mass. To determine the wave function fully, the following steps are pursued;

- α and hence β are determined by the continuity of the logarithmic derivative $\frac{1}{R}\frac{dR}{dr}$ at $r = a$. This condition reads

$$\frac{(\alpha a)j_{\ell-1}(\alpha a) - (\ell+1)j_\ell(\alpha a)}{j_\ell(\alpha a)} = \frac{(i\beta a)h^{(+)}_{\ell-1}(i\beta a) - (\ell+1)h^{(+)}_\ell(i\beta a)}{h^{(+)}_\ell(i\beta a)}. \tag{C.7}$$

- Once α and β have been found, a_ℓ and b_ℓ are found from the continuity of the wavefunction at $r = a$;

$$a_\ell j_\ell(\alpha a) = b_\ell h^{(+)}_\ell(i\beta a), \tag{C.8}$$

and from the normalization

$$|a_\ell|^2 \int_0^a dr r^2 j^2_\ell(\alpha r) + |b_\ell|^2 \int_a^{+\infty} dr r^2 |h^{(+)}_\ell(i\beta r)|^2 = 1. \tag{C.9}$$

The second integral needs to be found numerically, whereas the first one is found analytically to be

$$\int_0^a dr r^2 j^2_\ell(\alpha r) = \begin{cases} \frac{1}{\alpha^2}\left(\frac{a}{2} - \frac{\sin(2\alpha a)}{4\alpha}\right), & \ell = 0, \\ \frac{a^3}{2}\left(j^2_\ell(\alpha a) - j_{\ell-1}(\alpha a) j_{\ell+1}(\alpha a)\right), & \ell > 0. \end{cases} \tag{C.10}$$

Appendix D

States of a quantum dot with cone symmetry

In this appendix we discuss the wave functions of a quantum dot that is approximated by a cone or a truncated cone. The dot and the wetting layer are illustrated in Fig. 4.2. Due to the cylindrical symmetry of the quantum dot, the Hamiltonian is invariant by rotation around the z-axis. The eigenstates are therefore also eigenstates of L_z, the z-part of the angular momentum operator.

Bound states

The single-particle wave functions are labeled by the z-projection of the angular momentum,

$$\Psi_{m,n}(\rho,\phi,z) = e^{im\phi}\rho^{|m|}f_{m,n}(\rho,z), \tag{D.1}$$

where $m = 0, \pm 1, \pm 2, \ldots$ is the quantum number that describes rotation around the z-axis.[1] In general, $(n-1)$ is the number of radial nodes of $f_{m,n}(\rho,z)$. Here, we focus on $n = 1$. The function $f_{m,n=1}(\rho,z)$ is written as a variational wave function,

$$f_{m,n=1}(\rho,z) = N_m \exp\left(-\frac{\rho^2}{2\beta_m^2}\right)\exp\left(-\frac{(z-z_{0m})^2}{2\sigma_m^2}\right), \tag{D.2}$$

[1] Note that this quantum number is not the same as the azimuthal quantum number for a spherically symmetric dot because the total angular momentum ℓ is not a good quantum number.

where N_m are normalization constants and β_m, z_{0m} and σ_m are variational parameters. The variational parameters are determined for the total Hamiltonian for the cone *and the wetting layer*. Thus, for example by increasing the wetting-layer thickness the energy of the quantum-dot bound states is lowered.

We label the ground state with $|1S\rangle$ ($m = 0$), the first excited with $|1P\rangle$ ($m = \pm 1$), etc. All states are two-fold degenerate, apart from spin, except the ground state which is non-degenerate. Because we assume that the wave functions are separable in z and in-plane coordinates, we can write

$$\Psi_{m,n=1}(\mathbf{r}) = \Phi_{\perp}(\boldsymbol{\rho})\Phi_z(z). \tag{D.3}$$

The wave function in z is given by

$$\Phi_z(z) = N_z \exp\left(-\frac{(z - z_{0m})^2}{2\sigma_m^2}\right), \tag{D.4}$$

where $\sigma_m = \sigma_S, \sigma_P$ and $z_{0m} = z_{0S}, z_{0P}$ for the S and P states. The normalization constant for the z-part of the wave function, N_z, is determined by

$$|N_z|^2 \int_{-\infty}^{+\infty} dz \exp\left(-\frac{(z - z_{0m})^2}{\sigma_m^2}\right) = 1, \tag{D.5}$$

which gives

$$N_z = \frac{1}{\sqrt{\pi^{1/2}\sigma_m}}. \tag{D.6}$$

The in-plane part of the wave function is written as

$$\begin{aligned} \Phi_{\perp,S}(\boldsymbol{\rho}) &= \frac{1}{\sqrt{\pi\beta_S^2}} \exp\left(-\frac{\rho^2}{2\beta_S^2}\right) \\ \Phi_{\perp,P}(\boldsymbol{\rho}) &= \frac{1}{\sqrt{\pi\beta_P^4}} \rho \exp\left(-\frac{\rho^2}{2\beta_P^2}\right) e^{\pm i\phi}. \end{aligned} \tag{D.7}$$

The probability densities $|\Phi_z|^2$ and $\rho|\Phi_{\perp}(\rho)|^2$ are plotted in Fig. 4.3 for one specific dot geometry.

Fourier transforms

Throughout the thesis, in-plane Fourier transforms of quantum-dot wave functions need to be determined. We define the Fourier transform with

$$\Phi(\boldsymbol{\beta}) = \int d^2\rho e^{i\boldsymbol{\beta}\cdot\boldsymbol{\rho}}\Phi(\boldsymbol{\rho}). \tag{D.8}$$

The Fourier transforms of the in-plane wave functions for $|1S\rangle$ and $|1P\rangle$, $\Phi_\perp(\boldsymbol{\rho})$, are given by

$$\begin{aligned}\Phi_S(\boldsymbol{\beta}) &= 2\sqrt{\pi}\beta_S \exp\left(-\frac{\beta^2\beta_S^2}{2}\right)\\ \Phi_P(\boldsymbol{\beta}) &= 2\sqrt{\pi}\beta_P^2\beta \exp\left(-\frac{\beta^2\beta_P^2}{2}\right).\end{aligned} \tag{D.9}$$

Wetting-layer wave functions

The wetting-layer wave functions are assumed to be the solutions of a thin quantum well with the same confinement energy as the quantum dot. The wetting layer is assumed to be sufficiently large so that the wetting-layer wave functions can be separated in in-plane and z wave functions,

$$\Psi_k(\mathbf{r}) = \Phi_k(\boldsymbol{\rho})\Phi_{\mathrm{WL}}(z). \tag{D.10}$$

The in-plane wave function is approximated by a plane wave,

$$\Phi_k(\boldsymbol{\rho}) = \frac{e^{i\mathbf{k}\cdot\boldsymbol{\rho}}}{\sqrt{S}}, \tag{D.11}$$

where S is a macroscopic area, e. g. the wetting-layer area. Because the wetting layer is only one or a few monolayer thick, only the first subband for the z-dependent part is taken into account,

$$\Phi_{\mathrm{WL}}(z) = \begin{cases} B\exp\left(K_z\left(z+\frac{d}{2}\right)\right) & z < -d \\ A\cos\left(k_z\left(z+\frac{d}{2}\right)\right) & -d \le z \le 0 \\ B\exp\left(-K_z\left(z+\frac{d}{2}\right)\right) & z > 0. \end{cases} \tag{D.12}$$

The constants A, B, K_z and k_z are determined by matching $\Phi_{\mathrm{WL}}(z)$ and its derivative with respect to z at $z = -d$ and $z = 0$. The energy of a

wetting-layer carrier with wave vector $\mathbf{k}$ and mass m_c is then determined by

$$E = E^c_{\mathrm{WL}} + \frac{\hbar^2 k^2}{2m_c}, \tag{D.13}$$

where

$$E^c_{\mathrm{WL}} = \frac{\hbar^2 k_z^2}{2m_c}.$$

Appendix E

Total capture rate into a spherical quantum dot

In the following we show that the total capture rate into an energy level of a spherical quantum dot, characterized by the angular momentum quantum number ℓ_d, is independent of whether the incident carrier wave vector $\mathbf{k}$ is chosen along one particular direction or chosen with an arbitrary direction and an integration performed over all angles of $\mathbf{k}$. The total capture rate, from Eq. (3.1), is given by

$$R_{\ell_d} = 2 \sum_{m_d=-\ell_d}^{\ell_d} R^s_{\ell_d,m_d}, \tag{E.1}$$

where $R^s_{\ell_d,m_d}$ is the capture rate into the state (ℓ_d, m_d, s).[1] For our demonstration we calculate a sum that is given by

$$S \equiv \sum_{m_d=-\ell_d}^{\ell_d} \int d\Omega_q \int d\Omega_k \left|\langle d|V(\mathbf{r})|\mathbf{k}\rangle\right|^2, \tag{E.2}$$

where $V(\mathbf{r}) = e^{-i\mathbf{q}\cdot\mathbf{r}}$, $\Omega_q = (\theta_q, \phi_q)$ and $\Omega_k = (\theta_k, \phi_k)$ are the spherical angles that define the directions of $\mathbf{q}$ and $\mathbf{k}$ with respect to a reference axis that we choose to be $\hat{z}$ in the coordinate system of the quantum-dot wave functions. This sum contains the angular part of the summation

[1] The number n has no relevance in the derivation and is therefore omitted.

(integration) in Eq. (3.16) and the sum over m_d. In the derivation we use the addition theorem [85]

$$P_\ell(\cos\theta_{12}) = \frac{4\pi}{2\ell+1}\sum_{m=-\ell}^{\ell} Y_{\ell m}(\hat{\mathbf{r}}_1)Y^*_{\ell m}(\hat{\mathbf{r}}_2), \tag{E.3}$$

where P_ℓ is a Legendre polynomial and θ_{12} is the angle between the directions of $\mathbf{r}_1$ and $\mathbf{r}_2$. We also use the orthogonality of the spherical harmonics,

$$\int d\Omega Y^*_{\ell m}(\Omega)Y_{\ell' m'}(\Omega) = \delta_{\ell\ell'}\delta_{mm'}, \tag{E.4}$$

where the integration is performed over the spherical angle $\Omega \equiv (\theta, \phi)$.

E.1 k is parallel to $\hat{z}$

We first assume that the plane wave propagates along $\hat{z}$. The incident wave can then be written as

$$\begin{aligned}\Psi_k(\mathbf{r}) &= e^{ikz} \\ &= \sum_\ell P_\ell(\cos\theta)R_{k\ell}(r).\end{aligned} \tag{E.5}$$

$R_{k\ell}$ is a spherical Bessel function but its actual form is not relevant for the derivation here. We have neglected the normalization factor $1/\sqrt{\Omega}$ because it is not of relevance for the derivation here. We define

$$\begin{aligned}F &\equiv \langle\Psi_d|V|\Psi_k\rangle \\ &= \sum_\ell F_\ell,\end{aligned} \tag{E.6}$$

where

$$F_\ell = \int d^3r Y^*_{\ell_d m_d}(\hat{\mathbf{r}})R_{\ell_d}(r)V(\mathbf{r})P_\ell(\cos\theta)R_{k\ell}(r). \tag{E.7}$$

We write $S = \sum_{m_d} S_{m_d}$ and calculate

$$\begin{aligned} S_{m_d} &= \int d\Omega_q \int d\Omega_k |F|^2 \\ &= \int d\Omega_q \int d\Omega_k \sum_{\ell\ell'} F_\ell F^*_{\ell'} \\ &= 4\pi \sum_{\ell\ell'} \int d\Omega_q \int d^3r_1 d^3r_2 Y^*_{\ell_d m_d}(\hat{\mathbf{r}}_1) R^*_{\ell_d}(r_1) V(\mathbf{r}_1) P_\ell(\cos\theta_1) R_{k\ell}(r_1) \\ &\times Y_{\ell_d m_d}(\hat{\mathbf{r}}_2) R_{\ell_d}(r_2) V^*(\mathbf{r}_2) P_{\ell'}(\cos\theta_2) R^*_{k\ell'}(r_2). \end{aligned} \tag{E.8}$$

We use the relation (E.3) in the sum over m_d,

$$\begin{aligned} S &= \sum_{m_d} S_{m_d} \\ &= (2\ell_d + 1) \sum_{\ell\ell'} \int d\Omega_q \int d^3r_1 d^3r_2 P_{\ell_d}(\cos\theta_{12}) P_\ell(\cos\theta_1) P_{\ell'}(\cos\theta_2) \\ &\times R^*_{\ell_d}(r_1) R_{k\ell}(r_1) R_{\ell_d}(r_2) R^*_{k\ell'}(r_2) V(\mathbf{r}_1) V^*(\mathbf{r}_2). \end{aligned} \tag{E.9}$$

We rewrite the following Legendre polynomials by means of Eq. (E.3) in terms of the phonon wavevector $\mathbf{q}$,

$$\begin{aligned} P_\ell(\cos\theta_1) &= \frac{4\pi}{2\ell+1} \sum_{m=-\ell}^{\ell} Y_{\ell m}(\theta_q, \phi_q) Y^*_{\ell m}(\theta_{q_1}, \phi_{q_1}), \\ P_{\ell'}(\cos\theta_2) &= \frac{4\pi}{2\ell'+1} \sum_{m'=-\ell'}^{\ell'} Y^*_{\ell' m'}(\theta_q, \phi_q) Y_{\ell' m'}(\theta_{q_2}, \phi_{q_2}), \end{aligned} \tag{E.10}$$

where (θ_q, ϕ_q) are the angles between $\hat{z}$ and $\mathbf{q}$ and $(\theta_{q_i}, \phi_{q_i})$ are the angles between $\mathbf{q}$ and $\mathbf{r}_i$ $(i = 1, 2)$. This gives S to be

$$\begin{aligned} S &= (2\ell_d + 1) \sum_{\ell\ell'} \int d\Omega_q \frac{(4\pi)^2}{(2\ell+1)(2\ell'+1)} \\ &\times \sum_{mm'} \int d^3r_1 d^3r_2 P_{\ell_d}(\cos\theta_{12}) Y_{\ell m}(\theta_q, \phi_q) Y^*_{\ell' m'}(\theta_q, \phi_q) \\ &\times Y^*_{\ell m}(\theta_{q_1}, \phi_{q_1}) Y_{\ell' m'}(\theta_{q_2}, \phi_{q_2}) R^*_{\ell_d}(r_1) R_{k\ell}(r_1) R_{\ell_d}(r_2) R^*_{k\ell'}(r_2) V(\mathbf{r}_1) V^*(\mathbf{r}_2). \end{aligned} \tag{E.11}$$

The interaction potential V depends only on $(\theta_{q_i}, \phi_{q_i})$. By means of the orthogonality relation (E.4) we can easily integrate over $\Omega_q \equiv (\theta_q, \phi_q)$,

$$\begin{aligned} S = (2\ell_d + 1) \sum_{\ell,m} \left(\frac{4\pi}{2\ell + 1} \right)^2 \\ \times \int d^3r_1 d^3r_2 Y^*_{\ell m}(\theta_{q_1}, \phi_{q_1}) Y_{\ell m}(\theta_{q_2}, \phi_{q_2}) P_{\ell_d}(\cos\theta_{12}) \\ \times R^*_{\ell_d}(r_1) R_{k\ell}(r_1) R_{\ell_d}(r_2) R^*_{k\ell}(r_2) V(\mathbf{r}_1) V^*(\mathbf{r}_2). \end{aligned} \tag{E.12}$$

We use relation (E.3) one more time and obtain

$$\begin{aligned} S = (2\ell_d + 1) \sum_{\ell} \frac{4\pi}{2\ell + 1} \int d^3r_1 d^3r_2 P_{\ell}(\cos\theta_{12}) P_{\ell_d}(\cos\theta_{12}) \\ \times R^*_{\ell_d}(r_1) R_{k\ell}(r_1) R_{\ell_d}(r_2) R^*_{k\ell}(r_2) V(\mathbf{r}_1) V^*(\mathbf{r}_2). \end{aligned} \tag{E.13}$$

E.2 General case

In the case where $\mathbf{k}$ has an arbitrary direction, the incident plane wave can be written in terms of the spherical harmonics as

$$\begin{aligned} \Psi_k(\mathbf{r}) &= e^{i\mathbf{k}\cdot\mathbf{r}} \\ &= \sum_{\ell,m} \frac{4\pi}{2\ell + 1} Y_{\ell m}(\hat{\mathbf{k}}) Y^*_{\ell m}(\hat{\mathbf{r}}) R_{k\ell}(r), \end{aligned} \tag{E.14}$$

where $\hat{\mathbf{k}}$ and $\hat{\mathbf{r}}$ are unit vectors in the direction of $\mathbf{k}$ and $\mathbf{r}$, respectively. As before, we neglect the normalization factor $1/\sqrt{\Omega}$. We define

$$\begin{aligned} F &\equiv \langle \Psi_d | V | \Psi_k \rangle \\ &= \sum_{\ell,m} F_{\ell,m}, \end{aligned} \tag{E.15}$$

where

$$F_{\ell,m} = \frac{4\pi}{2\ell + 1} Y^*_{\ell m}(\hat{\mathbf{k}}) \int d^3r Y^*_{\ell_d m_d}(\hat{\mathbf{r}}) R^*_{\ell_d}(r) V(\mathbf{r}) Y_{\ell m}(\hat{\mathbf{r}}) R_{k\ell}(r). \tag{E.16}$$

The individual terms in the sum over m_d in Eq. (E.2) are given by

$$\begin{aligned} S_{m_d} &= \int d\Omega_q \int d\Omega_k |F|^2 \\ &= \int d\Omega_q \int d\Omega_k \sum_{\ell,m,\ell',m'} F_{\ell m} F^*_{\ell' m'} \\ &= \int d\Omega_q \int d\Omega_k \sum_{\ell,m,\ell',m'} \frac{(4\pi)^2}{(2\ell+1)(2\ell'+1)} Y^*_{\ell m}(\hat{\mathbf{k}}) Y_{\ell' m'}(\hat{\mathbf{k}}) \\ &\times \int d^3 r_1 Y^*_{\ell_d m_d}(\hat{\mathbf{r}}_1) R^*_{\ell_d}(r_1) V(\mathbf{r}_1) Y_{\ell m}(\hat{\mathbf{r}}_1) R_{k\ell}(r_1) \\ &\times \int d^3 r_2 Y^*_{\ell' m'}(\hat{\mathbf{r}}_2) R^*_{k\ell'}(r_2) V^*(\mathbf{r}_2) Y_{\ell_d m_d}(\hat{\mathbf{r}}_2) R_{\ell_d}(r_2). \end{aligned} \tag{E.17}$$

We use the orthogonality relation (E.4) and obtain

$$\begin{aligned} S_{m_d} = \sum_{\ell,m} \left(\frac{4\pi}{2\ell+1} \right)^2 \int d\Omega_q \int d^3 r_1 Y^*_{\ell_d m_d}(\hat{\mathbf{r}}_1) R^*_{\ell_d}(r_1) V(\mathbf{r}_1) Y_{\ell m}(\hat{\mathbf{r}}_1) R_{k\ell}(r_1) \\ \times \int d^3 r_2 Y^*_{\ell m}(\hat{\mathbf{r}}_2) R^*_{k\ell}(r_2) V^*(\mathbf{r}_2) Y_{\ell_d m_d}(\hat{\mathbf{r}}_2) R_{\ell_d}(r_2). \end{aligned} \tag{E.18}$$

Summing over m_d and using the relation (E.3) for the sum over m and m_d gives S to be

$$\begin{aligned} S = (2\ell_d+1) \sum_{\ell} \frac{1}{2\ell+1} \int d\Omega_q \int d^3 r_1 d^3 r_2 P_{\ell_d}(\cos\theta_{12}) P_\ell(\cos\theta_{12}) \\ \times R^*_{\ell_d}(r_1) R_{k\ell}(r_1) R_{\ell_d}(r_2) R^*_{k\ell}(r_2) V(\mathbf{r}_1) V^*(\mathbf{r}_2). \end{aligned} \tag{E.19}$$

This last integral is independent on the quantization axis, but depends only upon the angle between $\mathbf{r}_1$ and $\mathbf{r}_2$. Note that the summation over m_d, which allowed one to use the relation (E.3), was absolutely necessary to obtain this result. Integration over Ω_q yields a simple factor of 4π because all the terms in the integrand depend only on θ_{12} and the angles of $\mathbf{r}_1$ and $\mathbf{r}_2$ with respect to $\mathbf{q}$. We thus get

$$\begin{aligned} S = (2\ell_d+1) \sum_{\ell} \frac{4\pi}{2\ell+1} \int d^3 r_1 d^3 r_2 P_\ell(\cos\theta_{12}) P_{\ell_d}(\cos\theta_{12}) \\ \times R^*_{\ell_d}(r_1) R_{k\ell}(r_1) R_{\ell_d}(r_2) R^*_{k\ell}(r_2) V(\mathbf{r}_1) V^*(\mathbf{r}_2). \end{aligned} \tag{E.20}$$

This last result is exactly the same as the sum that we obtained in Eq. (E.13). In the derivation of the sum in the two cases it was necessary to integrate over the angles of $\mathbf{k}$ and $\mathbf{q}$ *and* the angular dependence of $V(\mathbf{r})$ had to be known. Note also that the expression for S in Eqs. (E.13) and (E.20) is not very practical for numerical implementation because it involves a sum over all angular momenta ℓ.

Appendix F

Matrix elements in two-phonon capture

The probability per unit time that a carrier is captured from the continuum to a discrete quantum-dot state by emission of two LO phonons was calculated in Appendix B.2. It is found to be

$$w(\mathbf{k},\mathbf{q}_1,\mathbf{q}_2) = \frac{2\pi}{\hbar}(\overline{n}+1)^2 \times \left| \sum_{\nu} \alpha(q_1)\alpha(q_2) \frac{M_{f\nu}^{q_2} M_{\nu i}^{q_1} + M_{f\nu}^{q_1} M_{\nu i}^{q_2}}{\epsilon_k - \epsilon_\nu - \hbar\omega_{LO}} \right|^2 \delta(E_f - E_i), \tag{F.1}$$

where the matrix elements $M_{f\nu}^{q_i}$ and $M_{\nu i}^{q_i}$, $i = 1, 2$ are defined in Eq. (3.22). Here, we derive equations for the matrix elements. The quantum-dot wave functions are the solutions to a spherically symmetric quantum well (Appendix C) and the wave function of the incident carrier is approximated by a plane wave,

$$\Psi_k(\mathbf{r}) = \frac{1}{\sqrt{\Omega}} e^{i\mathbf{k}\cdot\mathbf{r}}. \tag{F.2}$$

F.1 Matrix elements for continuum intermediate states

The first two terms of Eq. (3.32) are terms in which intermediate continuum states are involved. The matrix elements are given by the function

$$F(\mathbf{k}-\mathbf{q}_1-\mathbf{q}_2)=\frac{1}{\sqrt{\Omega}}\int d^3r\Psi_d^*(\mathbf{r})e^{i(\mathbf{k}-\mathbf{q}_1-\mathbf{q}_2)\cdot\mathbf{r}}, \tag{F.3}$$

i. e. F is essentially a three-dimensional Fourier transform of the quantum-dot wave function. We write all vectors in spherical coordinates,

$$\begin{aligned}\mathbf{k}&=(0,0,k)\\ \mathbf{q}_1&=q_1(\sin\theta_1\cos\phi_1,\sin\theta_1\sin\phi_1,\cos\theta_1)\\ \mathbf{q}_2&=q_2(\sin\theta_2\cos\phi_2,\sin\theta_2\sin\phi_2,\cos\theta_2)\\ \mathbf{r}&=r(\sin\theta_r\cos\phi_r,\sin\theta_r\sin\phi_r,\cos\theta_r).\end{aligned}$$

$\mathbf{k}$ is assumed to be parallel to $\hat{z}$. It was shown in Appendix E that this simplification yields the same total capture rate into a given energy level as when $\mathbf{k}$ is not assumed to have a specific direction. The dot product in the exponential of the integral in Eq. (F.3) is then given by

$$\begin{aligned}(\mathbf{k}-\mathbf{q}_1-\mathbf{q}_2)\cdot\mathbf{r}=r(&k\cos\theta_r-(q_1\sin\theta_1\cos(\phi_r-\phi_1)\\ &+q_2\sin\theta_2\cos(\phi_r-\phi_2))\sin\theta_r\\ &-(q_1\cos\theta_1+q_2\cos\theta_2)\cos\theta_r).\end{aligned} \tag{F.4}$$

The wave function for the state (ℓ,m) is written as

$$\Psi_d(\mathbf{r})=Y_{\ell m}(\theta_r,\phi_r)\chi_\ell(r). \tag{F.5}$$

We express the spherical harmonics by [84]

$$Y_{\ell m}(\theta,\phi)=K_{\ell m}P_\ell^{|m|}(\cos\theta)e^{im\phi}.$$

The factor $K_{\ell m}$ is such that

$$K_{\ell m}=\begin{cases}(-1)^m\left(\frac{2\ell+1}{4\pi}\frac{(\ell-|m|!)}{(\ell+|m|!)}\right)^{1/2}, & m>0\\ \left(\frac{2\ell+1}{4\pi}\frac{(\ell-|m|!)}{(\ell+|m|!)}\right)^{1/2}, & m\leq 0.\end{cases}$$

We can perform the intergration over ϕ_r in Eq. (F.3) analytically. The function to integrate is

$$g(\phi_r) = e^{-i(q_1 \sin\theta_1 \cos(\phi_r - \phi_1) + q_2 \sin\theta_2 \cos(\phi_r - \phi_2))r \sin\theta_r - im\phi_r}. \tag{F.6}$$

The function can be rewritten as

$$\begin{aligned} g(\phi_r) &= e^{-i(q_1 \sin\theta_1 \cos(\phi_r - \phi_1) + q_2 \sin\theta_2 \cos(\phi_r - \phi_2))r \sin\theta_r - im\phi_r} \\ &= e^{-iar \sin\theta_r \cos(\phi_r - \alpha) - im\phi_r}, \end{aligned} \tag{F.7}$$

where the variables a and α are given by

$$\begin{aligned} e^{-i\alpha} = e^{-i\alpha} &= \frac{\sqrt{q_1^2 \sin^2\theta_1 + q_2^2 \sin\theta_2 + 2q_1 q_2 \sin\theta_1 \sin\theta_2 \cos(\phi_1 - \phi_2)}}{q_1 \sin\theta_1 e^{i\phi_1} + q_2 \sin\theta_2 e^{i\phi_2}} \\ a &= \sqrt{q_1^2 \sin^2\theta_1 + q_2^2 \sin^2\theta_2 + 2q_1 q_2 \sin\theta_1 \sin\theta_2 \cos(\phi_1 - \phi_2)}. \end{aligned} \tag{F.8}$$

We use the expansion [86]

$$e^{it\cos\phi} = \sum_{n=-\infty}^{+\infty} i^n e^{in\phi} J_n(t), \tag{F.9}$$

and integration of the function in (F.7) becomes

$$\begin{aligned} \int_0^{2\pi} d\phi_r g(\phi_r) &= \int_0^{2\pi} d\phi_r \sum_{n=-\infty}^{+\infty} (-i)^n e^{-in(\phi_r - \alpha)} J_n(ar \sin\theta_r) e^{-im\phi_r} \\ &= 2\pi(-i)^{-m} e^{-im\alpha} J_{-m}(ar \sin\theta_r) \\ &= 2\pi(-i)^m e^{-im\alpha} J_m(ar \sin\theta_r), \end{aligned} \tag{F.10}$$

where we have used the identity [86]

$$J_{-m}(x) = (-1)^m J_m(x). \tag{F.11}$$

The matrix element F is now given by

$$\begin{aligned} F(\mathbf{k} - \mathbf{q}_1 - \mathbf{q}_2) &= \frac{2\pi}{\sqrt{\Omega}} (-i)^m e^{-im\alpha} K^*_{\ell m} \int_0^{+\infty} dr r^2 R^*_\ell(r) \\ &\times \int_0^{\pi} d\theta_r \sin\theta_r P_\ell^{|m|}(\cos\theta_r) J_m(ar \sin\theta_r) e^{ir\cos\theta_r (k - q_1 \cos\theta_1 - q_2 \cos\theta_2)}. \end{aligned} \tag{F.12}$$

F.2 Matrix elements for discrete intermediate states

We have

$$\begin{aligned} M^q_{f\nu} &= \langle \ell, n, m | e^{-i\mathbf{q}\cdot\mathbf{r}} | \ell_\nu, n_\nu, m_\nu \rangle \\ &= \int d^3 r Y^*_{\ell m}(\theta_r, \phi_r) R^*_\ell(r) e^{-i\mathbf{q}\cdot\mathbf{r}} Y_{\ell_\nu m_\nu}(\theta_r, \phi_r) R_{\ell_\nu}(r). \end{aligned} \tag{F.13}$$

In spherical coordinates, the dot product $\mathbf{q}\cdot\mathbf{r}$ is

$$\mathbf{q}\cdot\mathbf{r} = qr\left[\sin\theta_q \sin\theta_r \cos(\phi_r - \phi_q) + \cos\theta_q \cos\theta_r\right]. \tag{F.14}$$

The integration over ϕ_r can be performed by using the expansion from Eq. (F.9)

$$e^{-iqr\sin\theta_q \sin\theta_r \cos(\phi_r - \phi_q)} = \sum_{n=-\infty}^{+\infty} (-i)^n e^{-in(\phi_r - \phi_q)} J_n(qr\sin\theta_q \sin\theta_r). \tag{F.15}$$

This yields for the ϕ_r integration

$$\begin{aligned} &\int_0^{2\pi} d\phi_r e^{i(m_\nu - m)\phi_r} e^{-iqr\sin\theta_q \sin\theta_r \cos(\phi_r - \phi_q)} \\ &= \int_0^{2\pi} d\phi_r e^{i(m_\nu - m)\phi_r} \sum_{n=-\infty}^{+\infty} (-i)^n e^{-in(\phi_r - \phi_q)} J_n(qr\sin\theta_q \sin\theta_r) \\ &= 2\pi(-i)^{m_\nu - m} e^{i(m_\nu - m)\phi_q} J_{m_\nu - m}(qr\sin\theta_q \sin\theta_r). \end{aligned} \tag{F.16}$$

The matrix element is then expressed as

$$M^q_{f\nu} = 2\pi(-i)^{m_\nu - m} e^{i(m_\nu - m)\phi_q} K^*_{\ell m} K_{\ell_\nu m_\nu} S(a, \ell, n, m, \ell_\nu, n_\nu, m_\nu, q, \theta_q), \tag{F.17}$$

where

$$\begin{aligned} S(a, \ell, n, m, \ell_\nu, n_\nu, m_\nu, q, \theta_q) &= \int_0^{+\infty} dr r^2 R^*_\ell(r) R_{\ell_\nu}(r) \\ &\times \int_0^\pi d\theta_r \sin\theta_r P^{|m|}_\ell(\cos\theta_r) P^{|m_\nu|}_{\ell_\nu}(\cos\theta_r) \\ &\times e^{-iqr\cos\theta_q \cos\theta_r} J_{m_\nu - m}(qr\sin\theta_q \sin\theta_r). \end{aligned} \tag{F.18}$$

The matrix element $M^q_{\nu i}$ is given by

$$\begin{aligned} M^q_{\nu i} &= \langle \ell_\nu, n_\nu, m_\nu | e^{-i\mathbf{q}\cdot\mathbf{r}} | \mathbf{k} \rangle \\ &= \frac{1}{\sqrt{\Omega}} \int d^3 r Y^*_{\ell_\nu m_\nu}(\theta_r, \phi_r) R^*_{\ell_\nu}(r) e^{i(\mathbf{k}-\mathbf{q})\cdot\mathbf{r}}. \end{aligned} \tag{F.19}$$

The dot product $(\mathbf{k}-\mathbf{q})\cdot\mathbf{r}$ is given by

$$(\mathbf{k}-\mathbf{q})\cdot\mathbf{r} = r\cos\theta_r(k - q\cos\theta_q) - qr\sin\theta_q\sin\theta_r\cos(\phi_r - \phi_q). \tag{F.20}$$

Integration over ϕ_r is now

$$\begin{aligned} &\int_0^{2\pi} d\phi_r e^{-im_\nu\phi_r} e^{-iqr\sin\theta_q\sin\theta_r\cos(\phi_r-\phi_q)} \\ &= \int_0^{2\pi} d\phi_r e^{-im_\nu\phi_r} \sum_{n=-\infty}^{+\infty} (-i)^n e^{-in(\phi_r-\phi_q)} J_n(qr\sin\theta_q\sin\theta_r) \\ &= 2\pi i^{-m_\nu} e^{-im_\nu\phi_q} J_{m_\nu}(qr\sin\theta_q\sin\theta_r), \end{aligned} \tag{F.21}$$

where we have used the identity from Eq. (F.11) to obtain the last expression. The matrix element becomes

$$M^q_{\nu i} = \frac{2\pi}{\sqrt{\Omega}} i^{-m_\nu} e^{-im_\nu\phi_q} K^*_{\ell_\nu m_\nu} T(a, \ell_\nu, n_\nu, m_\nu, q, \theta_q), \tag{F.22}$$

where

$$\begin{aligned} &T(a, \ell_\nu, n_\nu, m_\nu, q, \theta_q) = \int dr r^2 R^*_{\ell_\nu}(r) \\ &\times \int_0^\pi d\theta_r \sin\theta_r P^{|m_\nu|}_{\ell_\nu}(\cos\theta_r) e^{i(k-q\cos\theta_q)r\cos\theta_r} J_{m_\nu}(qr\sin\theta_q\sin\theta_r). \end{aligned} \tag{F.23}$$

This yields for matrix elements involving discrete intermediate states

$$\begin{aligned} &M^{q_2}_{f\nu} M^{q_1}_{\nu i} + M^{q_1}_{f\nu} M^{q_2}_{\nu i} = \frac{(2\pi)^2}{\sqrt{\Omega}} (-1)^{m_\nu} i^m K_{\ell m} |K_{\ell_\nu m_\nu}|^2 e^{-im\phi_1} \\ &\times [e^{i(m-m_\nu)(\phi_1-\phi_2)} S(a, \ell, n, m, \ell_\nu, n_\nu, m_\nu, q_2, \theta_2) T(a, \ell_\nu, n_\nu, m_\nu, q_1, \theta_1) \\ &+ e^{im_\nu(\phi_1-\phi_2)} S(a, \ell, n, m, \ell_\nu, n_\nu, m_\nu, q_1, \theta_1) T(a, \ell_\nu, n_\nu, m_\nu, q_2, \theta_2)], \end{aligned} \tag{F.24}$$

where we have set the angles of $\mathbf{q}_1$ and $\mathbf{q}_2$ to be (θ_1, ϕ_1) and (θ_2, ϕ_2), respectively.

Appendix G

Discretization of carrier and phonon modes

This appendix describes the practical aspects of the diagonalization of the Fröhlich Hamiltonian for interaction of carriers in quasi-bound states with LO phonons, investigated in section 5.2.

G.1 Discretization of the electronic continuum

In this section we discuss continuum wave functions of a spherical quantum dot and show how these are calculated. By continuum wave functions we refer to wave functions with energy $E > V_0$, where V_0 is the quantum-dot barrier. Bound states of a spherical quantum dot ($E < V_0$) are discussed in Appendix C. The continuum wave functions are written as

$$\Psi_\nu(\mathbf{r}) = Y_\ell^m(\theta, \phi) R_\ell(r), \tag{G.1}$$

where the radial wave functions are spherical Bessel functions [85],

$$R_\ell(r) = \begin{cases} C_\ell j_\ell(\kappa r) & r \leq a, \\ A_\ell j_\ell(kr) + B_\ell y_\ell(kr) & r > a. \end{cases} \tag{G.2}$$

j_ℓ is the spherical Bessel function and y_ℓ the spherical Neumann function. κ and k are related according to

$$\frac{\hbar^2 \kappa^2}{2m^*} = \frac{\hbar^2 k^2}{2m^*} + V_0, \tag{G.3}$$

where V_0 is the confinement potential strength and m^* is the carrier effective mass. κ can be interpreted as the wavenumber of the carrier *inside* the region of the quantum dot and k the wavenumber of the carrier *outside* the region. By setting $k = 0$, κ is determined solely by the depth of the quantum well. To determine the wavefunction fully, the following steps are pursued:

- κ and hence k are determined by the continuity of the logarithmic derivative $\frac{1}{R_\ell}\frac{dR_\ell}{dr}$ at $r = a$. This condition reads

$$\frac{(\kappa a)j_{\ell-1}(\kappa a) - (\ell+1)j_\ell(\kappa a)}{j_\ell(\kappa a)} = \frac{A_\ell\left[(ka)j_{\ell-1}(ka) - (\ell+1)j_\ell(ka)\right]}{A_\ell j_\ell(ka) + B_\ell y_\ell(ka)} + \frac{B_\ell\left[(ka)y_{\ell-1}(ka) - (\ell+1)y_\ell(ka)\right]}{A_\ell j_\ell(ka) + B_\ell y_\ell(ka)}, \tag{G.4}$$

  which, after a few algebraic steps, leads to

$$\begin{aligned} &A_\ell\left[(\kappa a)j_\ell(ka)j_{\ell-1}(\kappa a) - (ka)j_\ell(\kappa a)j_{\ell-1}(ka)\right] = \\ &B_\ell\left[(ka)j_\ell(\kappa a)y_{\ell-1}(ka) - (\kappa a)y_\ell(ka)j_{\ell-1}(\kappa a)\right] \end{aligned} \tag{G.5}$$

  We require that the wave function is equal to zero at the boundary of a large sphere with radius R_b,

$$A_\ell j_\ell(kR_b) + B_\ell y_\ell(kR_b) = 0. \tag{G.6}$$

  Solving for A_ℓ and inserting for A_ℓ into Eq. (G.5) yields, for $B_\ell \neq 0$,

$$\begin{aligned} &\left[(ka)j_\ell(\kappa a)y_{\ell-1}(ka) - (\kappa a)y_\ell(ka)j_{\ell-1}(\kappa a)\right] j_\ell(kR_b) \\ &+ \left[(\kappa a)j_\ell(ka)j_{\ell-1}(\kappa a) - (ka)j_\ell(\kappa a)j_{\ell-1}(ka)\right] y_\ell(kR_b) = 0. \end{aligned} \tag{G.7}$$

  The above equation can be solved for either k or κ, with aid of Eq. (G.3).

- From the continuity of R_ℓ at $r = a$ and the requirement that the wave function is zero at the boundary of the large sphere we can determine two of the constants A_ℓ, B_ℓ and C_ℓ in terms of the third one. In terms of A_ℓ we get

$$\begin{aligned} B_\ell &= -A_\ell\frac{j_\ell(kR_b)}{y_\ell(kR_b)} \qquad \text{[from (G.6)]} \\ C_\ell &= A_\ell\frac{j_\ell(ka)y_\ell(kR_b) - j_\ell(kR_b)y_\ell(ka)}{y_\ell(kR_b)j_\ell(\kappa a)}. \end{aligned} \tag{G.8}$$

- From the normalization condition we have

$$|C_\ell|^2 \int_0^a dr r^2 j_\ell^2(\kappa r) + \int_a^{R_b} dr r^2 |A_\ell j_\ell(kr) + B_\ell y_\ell(kr)|^2 = 1. \quad \text{(G.9)}$$

With aid of Eq. (G.8), Eq. (G.9) can be used to solve for A_ℓ since we have already solved for k and κ. Once A_ℓ is found, B_ℓ and C_ℓ can be determined from Eq. (G.8). The first integral in Eq. (G.9) can be found analytically,

$$\int_0^a dr r^2 j_\ell^2(\kappa r) = \begin{cases} \frac{1}{\kappa^2}\left(\frac{a}{2} - \frac{\sin(2\kappa a)}{4\kappa}\right), & \ell = 0, \\ \frac{a^3}{2}\left(j_\ell^2(\kappa a) - j_{\ell-1}(\kappa a) j_{\ell+1}(\kappa a)\right), & \ell > 0. \end{cases} \quad \text{(G.10)}$$

The second integral in Eq. (G.9) needs to be calculated numerically.

G.2 Discretization of phonon modes and diagonalization

The matrix element $u_{\mathbf{q}\nu}$ from Eq. (5.11) is given by

$$u_{\mathbf{q}\nu} = \alpha(q) \langle S \left| e^{-i\mathbf{q}\cdot\mathbf{r}} \right| \nu \rangle. \quad \text{(G.11)}$$

We write the plane wave $e^{-i\mathbf{q}\cdot\mathbf{r}}$ in terms of spherical Bessel functions and spherical harmonics,

$$e^{-i\mathbf{q}\cdot\mathbf{r}} = 4\pi \sum_{\ell_1} (-i)^{\ell_1} j_{\ell_1}(qr) \sum_{m_1=-\ell_1}^{\ell_1} Y^*_{\ell_1 m_1}(\theta_r, \phi_r) Y_{\ell_1 m_1}(\theta_q, \phi_q). \quad \text{(G.12)}$$

We insert Eq. (G.12) into Eq. (G.11) and use the orthonormality relation for the spherical harmonics,

$$\int d\theta \sin\theta d\phi Y^*_{\ell_1 m_1}(\theta, \phi) Y_{\ell m}(\theta, \phi) = \delta_{\ell_1, \ell} \delta_{m_1, m}. \quad \text{(G.13)}$$

Integration over the spherical angles (θ_r, ϕ_r) gives

$$u_{\mathbf{q}\nu} = \alpha(q) \sqrt{4\pi} (-i)^\ell Y_{\ell m}(\theta_q, \phi_q) \int_0^{+\infty} dr r^2 \chi_0^*(r) j_\ell(qr) R_\ell(r) \quad \text{(G.14)}$$

$$\equiv \alpha(q) Y_{\ell m}(\theta_q, \phi_q) F_\nu(q). \quad \text{(G.15)}$$

We have used here that $Y_{00}(\theta_r, \phi_r) = 1/\sqrt{4\pi}$ and we have defined

$$F_\nu(q) \equiv \sqrt{4\pi}(-i)^\ell \int_0^{+\infty} dr r^2 \chi_0^*(r) j_\ell(qr) R_\ell(r). \tag{G.16}$$

The eigenvalue equations, from Eq. (5.10), read

$$a_\nu(E_\nu - E) + \sum_{\mathbf{q}} \beta_{\mathbf{q}} u_{\nu\mathbf{q}} = 0 \tag{G.17}$$

$$\beta_{\mathbf{q}}(E_S + \hbar\omega_{\mathrm{LO}} - E) + \sum_{\nu} a_\nu u_{\mathbf{q}\nu} = 0, \tag{G.18}$$

where we have assumed dispersionless phonons, $\hbar\omega_{\mathbf{q}} \approx \hbar\omega_{\mathrm{LO}}$. The energy E_ν is given by $\hbar^2\kappa_\nu^2/(2m^*)$. We mentioned in section 5.2 that the number ν characterizes the quantum numbers for the electronic continuum, i. e. k, ℓ and m. We notice that the above eigenvalue equations do not depend on the quantum number m, only on ℓ (from $F_\nu(q)$ and E_ν). We also mentioned that the angular momentum quantum number ℓ will be set to 1 since, in our particular example, we wish to investigate the influence of carrier-phonon coupling in the case of a "P-like" quasi-bound state. The above eigenvalue equations thus only depend on k for constant ℓ. By enclosing the quantum dot in a large box of radius R_b, as discussed in the previous section, the wavenumber k becomes discrete and the energy level spacing fulfills $\Delta E_\nu \sim 1/R_b^2$.[1] We define n_k as the size of the electronic continuum (number of wavenumbers). We also point out here that k is one-dimensional due to the spherical symmetry of the problem.

We now discretize the phonon wavevector. First, we observe that $\beta_{\mathbf{q}}$ can be written as $\beta_{\mathbf{q}} = \beta_q Y_{\ell m}(\theta_q, \phi_q)$. This can be seen directly from Eq. (G.18) taking relation (G.15) into account. We transform the sum in Eq. (G.17) into an integral,

$$\sum_{\mathbf{q}} \longrightarrow \frac{\Omega}{(2\pi)^3} \int dq q^2 d\theta_q \sin\theta_q d\phi_q, \tag{G.19}$$

where $\Omega = 4\pi R_b^3/3$ is the quantization volume. We also insert expression

[1] The energy level spacing in a quantum well of infinite confinement follows this behavior. This is also what we have here for the large sphere due to our requirement that the wave function is zero on the boundary.

(G.15) into Eqs. (G.17) and (G.18). We then get

$$a_\nu(E_\nu - E) + \frac{\Omega}{(2\pi)^3}\int dq q^2 \beta_q \alpha^*(q) F_\nu^*(q) = 0 \tag{G.20}$$

$$\beta_q(E_S + \hbar\omega_{\mathrm{LO}} - E) + \sum_\nu a_\nu \alpha(q) F_\nu(q) = 0. \tag{G.21}$$

In Eq. (G.20) we have integrated over θ_q and ϕ_q. Eq. (G.21) was obtained by multiplying by $Y^*_{\ell m}(\theta_q, \phi_q)$ and then integrating over θ_q and ϕ_q. We now approximate the integral over q by a finite sum,

$$\int_0^{+\infty} dq f(q) \longrightarrow \sum_{i=1}^{n_q} \Delta q_i f(q_i), \tag{G.22}$$

where n_q is the size of the phonon wave vector. We then obtain

$$a_\nu E_\nu + \frac{\Omega}{(2\pi)^3}\sum_{i=1}^{n_q} \beta_{q_i} \Delta q_i q_i^2 \alpha^*(q_i) F_\nu^*(q_i) = E a_\nu \tag{G.23}$$

$$\beta_{q_i}(E_S + \hbar\omega_{\mathrm{LO}}) + \sum_\nu a_\nu \alpha(q_i) F_\nu(q_i) = E\beta_{q_i}. \tag{G.24}$$

The above equations define a $(n_k + n_q) \times (n_k + n_q)$ matrix with elements E_ν and $E_s + \hbar\omega_{\mathrm{LO}}$ on the diagonal. We notice that the matrix in Eqs. (G.23) and (G.24) is not Hermitian which can be seen from the off-diagonal elements. This comes from our reduction of **q**-space that comes about when we integrate over the angles. However if we want to determine the eigenenergies E by a numerical algorithm it is usually required that the input matrix is Hermitian. How can we solve this problem? We can multiply Eq. (G.24) by some constant and define new elements γ_j instead of a_ν and β_{q_i},

$$\gamma_j = \begin{cases} a_\nu & j \in [1, n_k] \\ c_i\beta_{q_i} & j \in [n_k + 1, n_k + n_q] \quad (i \in [1, n_q]). \end{cases} \tag{G.25}$$

Our requirement is the following,

$$\begin{aligned} \gamma_j &= c_j \beta_{q_j} \\ \frac{\Delta q_j q_j^2 \Omega}{(2\pi)^3}\beta_{q_j} &= c_j^* \gamma_j. \end{aligned} \tag{G.26}$$

We thus obtain

$$|c_j|^2 = \frac{\Delta q_j q_j^2 \Omega}{(2\pi)^3}. \tag{G.27}$$

A Hermitian matrix is thus obtained,

$$\gamma_j E_j + \sum_{i=n_k+1}^{n_k+n_q} \gamma_i \sqrt{\frac{\Delta q_i q_i^2 \Omega}{(2\pi)^3}} \alpha^*(q_i) F_j^*(q_i) = E\gamma_j \quad (1 \le j \le n_k) \tag{G.28}$$

$$\gamma_j (E_S + \hbar\omega_{\mathrm{LO}}) + \sum_{i=1}^{n_k} \gamma_i \sqrt{\frac{\Delta q_j q_j^2 \Omega}{(2\pi)^3}} \alpha(q_j) F_i(q_j) = E\gamma_j \quad (n_k < j \le n_k + n_q). \tag{G.29}$$

Appendix H

Auger carrier capture rates into states $|1S\rangle$ and $|1P\rangle$

In the following, we calculate the capture rate for the Auger process of two carriers interacting via Coulomb interaction in the wetting layer and, as a result, one carrier is captured into the quantum dot while the other is excited to a higher energy within the wetting layer. We start by calculating the scalar product,

$$M_\rho \equiv \left\langle \Phi_\perp \left| e^{i(\mathbf{k}_s - \mathbf{k}'_s)\cdot\boldsymbol{\rho}_c} \right| \Phi_{k_c} \right\rangle_\perp , \tag{H.1}$$

from which the sum in Eq. (6.23),

$$\begin{aligned} R_J = \frac{\pi}{2\hbar}\left(\frac{e^2}{\epsilon_r\epsilon_0}\right)^2 \frac{1}{S^2}\sum_{\mathbf{k}_s}\sum_{\mathbf{k}'_s}\sum_{\mathbf{k}_c} \frac{|H(|\mathbf{k}_s - \mathbf{k}'_s|)|^2}{|\mathbf{k}_s - \mathbf{k}'_s|^2}|M_\rho|^2 \\ \times f(\epsilon_{k_s})f(\epsilon_{k_c})(1 - f(\epsilon_{k'_s}))\delta\left(\frac{\hbar^2 k_s'^2}{2m_s} - \frac{\hbar^2 k_s^2}{2m_s} - \left(E^c_{\mathrm{WL}} + \frac{\hbar^2 k_c^2}{2m_c} - E_{\mathrm{d}}\right)\right), \end{aligned} \tag{H.2}$$

can be calculated. We will calculate R_J for capture into the states $|1S\rangle$ and $|1P\rangle$, respectively.

H.1 Capture into $|1S\rangle$

The in-plane part of the quantum-dot wave function is given by

$$\Phi_\perp(\boldsymbol{\rho}) = \frac{1}{\sqrt{\pi\beta_S^2}} \exp\left(-\frac{\rho^2}{2\beta_S^2}\right). \tag{H.3}$$

The in-plane matrix element is then given by [see Eq. (D.9)]

$$\begin{aligned} M_\rho &= \left\langle \Phi_\perp \left| e^{i(\mathbf{k}_s - \mathbf{k}'_s)\cdot\boldsymbol{\rho}_c} \right| \Phi_{k_c} \right\rangle_\perp \\ &= \frac{1}{\sqrt{S}} \int d^2\rho_c e^{i(\mathbf{k}_s - \mathbf{k}'_s + \mathbf{k}_c)\cdot\boldsymbol{\rho}_c} \Phi_\perp^*(\boldsymbol{\rho}_c) \\ &= \frac{2\sqrt{\pi}\beta_S}{\sqrt{S}} \exp\left(-\frac{(\mathbf{k}_s - \mathbf{k}'_s + \mathbf{k}_c)^2\beta_S^2}{2}\right). \end{aligned} \tag{H.4}$$

We write

$$\begin{aligned} |\mathbf{k}_s - \mathbf{k}'_s + \mathbf{k}_c|^2 &= |\mathbf{k}_s - \mathbf{k}'_s|^2 + k_c^2 + 2k_c|\mathbf{k}_s - \mathbf{k}'_s|\cos\phi \\ |\mathbf{k}_s - \mathbf{k}'_s|^2 &= k_s'^2 + k_s^2 - 2k'_s k_s \cos\theta, \end{aligned} \tag{H.5}$$

where θ is the angle between $\mathbf{k}_s$ and $\mathbf{k}'_s$ and ϕ is the angle between $(\mathbf{k}_s - \mathbf{k}'_s)$ and $\mathbf{k}_c$. The triple sum over $\mathbf{k}_s$, $\mathbf{k}'_s$ and $\mathbf{k}_c$ is transformed into a triple integral,

$$\sum_{\mathbf{k}_s}\sum_{\mathbf{k}'_s}\sum_{\mathbf{k}_c} \to \frac{S^3}{(2\pi)^6} \iiint d^2k_s d^2k'_s d^2k_c. \tag{H.6}$$

We then write the integration over the three wavevectors $\mathbf{k}_s$, $\mathbf{k}'_s$ and $\mathbf{k}_c$ as

$$\begin{aligned} \iiint d^2k_s d^2k'_s d^2k_c &= \int dk_s k_s d\phi_s \int dk'_s k'_s d\theta \int dk_c k_c d\phi \\ &= 2\pi \int dk_s k_s \int dk'_s k'_s \int d\theta \int dk_c k_c \int d\phi, \end{aligned} \tag{H.7}$$

where the factor 2π comes from an integration over ϕ_s because the integrand in Eq. (H.2) does not depend upon ϕ_s. We get

$$\begin{aligned} R_J = & \frac{\pi}{2\hbar}\left(\frac{e^2}{\epsilon_r\epsilon_0}\right)^2 \frac{S}{(2\pi)^5} \\ & \times \int dk_s k_s \int dk_s' k_s' \int d\theta \int dk_c k_c \int d\phi \frac{|H(|\mathbf{k}_s - \mathbf{k}_s'|)|^2}{|\mathbf{k}_s - \mathbf{k}_s'|^2} |M_\rho|^2 \\ & \times f(\epsilon_{k_s}) f(\epsilon_{k_c})(1 - f(\epsilon_{k_s'}))\delta\left(\frac{\hbar^2 k_s'^2}{2m_s} - \frac{\hbar^2 k_s^2}{2m_s} - \left(E_{\mathrm{WL}}^c + \frac{\hbar^2 k_c^2}{2m_c} - E_{\mathrm{d}}\right)\right). \end{aligned} \tag{H.8}$$

The only term in Eq. (H.2) that depends on ϕ is $|M_\rho|^2$. The integral over ϕ is easily performed, giving an integral representation of I_0, a Bessel function of the second kind [87],

$$\begin{aligned} \langle |M_\rho|^2 \rangle_\phi &= \int_0^{2\pi} d\phi |M_\rho|^2 \\ &= \frac{4\pi\beta_S^2}{S} \int_0^{2\pi} d\phi \exp\left(-(\mathbf{k}_s - \mathbf{k}_s' + \mathbf{k}_c)^2 \beta_S^2\right) \\ &= \frac{4\pi\beta_S^2}{S} \exp\left(-(|\mathbf{k}_s - \mathbf{k}_s'|^2 + k_c^2)\beta_S^2\right) \\ &\times \int_0^{2\pi} d\phi \exp\left(-2\beta_S^2 |\mathbf{k}_s - \mathbf{k}_s'| k_c \cos\phi\right) \\ &= \frac{8\pi^2\beta_S^2}{S} \exp\left(-(|\mathbf{k}_s - \mathbf{k}_s'|^2 + k_c^2)\beta_S^2\right) I_0(2\beta_S^2 |\mathbf{k}_s - \mathbf{k}_s'| k_c). \end{aligned} \tag{H.9}$$

The energy conservation requirement, expressed by the δ function in Eq. (H.2) reads

$$\frac{\hbar^2 k_s'^2}{2m_s} - \frac{\hbar^2 k_s^2}{2m_s} = E_{\mathrm{WL}}^c + \frac{\hbar^2 k_c^2}{2m_c} - E_{1\mathrm{S}}, \tag{H.10}$$

i. e. the energy is transferred from the captured carrier (c) to the wetting-layer carrier (s) which is promoted higher up in the wetting layer. We therefore obtain that k_c needs to fulfill

$$k_c^0 = \pm\sqrt{\frac{m_c}{m_s}(k_s'^2 - k_s^2) + \frac{2m_c}{\hbar^2}(E_{1\mathrm{S}} - E_{\mathrm{WL}}^c)}. \tag{H.11}$$

The δ function is rewritten as [54]

$$\begin{aligned}&\delta\left(\frac{\hbar^2 k_s'^2}{2m_s}-\frac{\hbar^2 k_s^2}{2m_s}-\left(E_{\mathrm{WL}}^c+\frac{\hbar^2 k_c^2}{2m_c}-E_{1\mathrm{S}}\right)\right)\\&=\frac{m_c}{\hbar^2 k_c}\left(\delta\left(k_c-k_c^0\right)+\delta\left(k_c+k_c^0\right)\right).\end{aligned}\tag{H.12}$$

We thus obtain

$$\begin{aligned}R_J^{|1S\rangle}=&\frac{1}{8\pi^2\hbar}\left(\frac{e^2}{\epsilon_r\epsilon_0}\right)^2\beta_S^2\frac{m_c}{\hbar^2}\int dk_s k_s f(\epsilon_{k_s})\int dk_s' k_s' f(\epsilon_{k_{c0}})\\&\times\int_0^{2\pi}d\theta\frac{|H(|\mathbf{k}_s-\mathbf{k}_s'|)|^2}{|\mathbf{k}_s-\mathbf{k}_s'|^2}\exp\left(-(|\mathbf{k}_s-\mathbf{k}_s'|^2+k_{c0}^2)\beta_S^2\right)\\&\times I_0(2\beta_S^2|\mathbf{k}_s-\mathbf{k}_s'|k_{c0}),\end{aligned}\tag{H.13}$$

where we have approximated $[1-f(\epsilon_{k_s'})]\approx 1$ and we have integrated over k_c with aid of the δ function.

H.2 Capture into $|1P\rangle$

The in-plane quantum-dot wave function for the first excited state, $|1P\rangle$, is given by

$$\Phi_\perp(\boldsymbol{\rho})=\frac{1}{\sqrt{\pi\beta_P^4}}\rho\exp\left(-\frac{\rho^2}{2\beta_P^2}\right)e^{\pm i\phi}.\tag{H.14}$$

The in-plane matrix element is found to be [see Eq. (D.9)]

$$\begin{aligned}M_\rho=&\frac{1}{\sqrt{S}}\int d^2\rho_c\Phi_\perp^*(\boldsymbol{\rho}_c)e^{i(\mathbf{k}_s-\mathbf{k}_s'+\mathbf{k}_c)\cdot\boldsymbol{\rho}_c}\\=&\frac{2\sqrt{\pi}|\mathbf{k}_s-\mathbf{k}_s'+\mathbf{k}_c|\beta_P^2}{\sqrt{S}}\exp\left(-\frac{(\mathbf{k}_s-\mathbf{k}_s'+\mathbf{k}_c)^2\beta_P^2}{2}\right).\end{aligned}\tag{H.15}$$

We observe that the capture rate in Eq. (H.2) depends on angles of wavevectors through $|\mathbf{k}_s-\mathbf{k}_s'|$ and $|\mathbf{k}_s-\mathbf{k}_s'+\mathbf{k}_c|$ as the capture rate into $|1S\rangle$. We express therefore $|\mathbf{k}_s-\mathbf{k}_s'|$ and $|\mathbf{k}_s-\mathbf{k}_s'+\mathbf{k}_c|$ as in Eq. (H.5), convert the triple sum over $\mathbf{k}_s'$, $\mathbf{k}_s$ and $\mathbf{k}_c$ into a triple integral [see Eq. (H.6)] and write the integral as in Eq. (H.7). As before, the integrand depends on ϕ through

$|M_\rho|^2$, which, integrated over ϕ yields

$$\begin{aligned}\langle|M_\rho|^2\rangle_\phi &= \int_0^{2\pi} d\phi |M_\rho|^2 \\ &= \frac{4\pi\beta_P^4}{S}\int_0^{2\pi} d\phi |\mathbf{k}_s - \mathbf{k}'_s - \mathbf{k}_c|^2 \exp\left(-\beta_P^2(|\mathbf{k}_s - \mathbf{k}'_s - \mathbf{k}_c|^2\right) \\ &= \frac{8\pi^2\beta_P^4}{S}\exp\left(-\beta_P^2(|\mathbf{k}_s - \mathbf{k}'_s|^2 + k_c^2)\right) \\ &\times\Bigg[(|\mathbf{k}_s - \mathbf{k}'_s|^2 + k_c^2) I_0(2\beta_P^2|\mathbf{k}_s - \mathbf{k}'_s|k_c) \\ &- 2|\mathbf{k}_s - \mathbf{k}'_s|k_c I_1(2\beta_P^2|\mathbf{k}_s - \mathbf{k}'_s|k_c)\Bigg].\end{aligned} \tag{H.16}$$

We rewrite the δ function as in Eq. (H.12), where k_c now fulfills

$$k_c^0 = \pm\sqrt{\frac{m_c}{m_s}(k_s'^2 - k_s^2) + \frac{2m_c}{\hbar^2}(E_{1\mathrm{P}} - E^{\mathrm{c}}_{\mathrm{WL}})}. \tag{H.17}$$

We can thus integrate over k_c in Eq. (H.2). We insert also the integral over ϕ, from Eq. (H.16). This gives

$$\begin{aligned}R_J^{|1P\rangle} &= \frac{1}{8\pi^2\hbar}\left(\frac{e^2}{\epsilon_r\epsilon_0}\right)^2 \beta_P^4 \frac{m_c}{\hbar^2}\int dk_s k_s f(\epsilon_{k_s})\int dk'_s k'_s f(\epsilon_{k_{c0}}) \\ &\times\int_0^{2\pi} d\theta \frac{|H(|\mathbf{k}_s - \mathbf{k}'_s|)|^2}{|\mathbf{k}_s - \mathbf{k}'_s|^2}\exp\left(-\beta_P^2(|\mathbf{k}_s - \mathbf{k}'_s|^2 + k_{c0}^2)\right) \\ &\times[(|\mathbf{k}_s - \mathbf{k}'_s|^2 + k_{c0}^2) I_0(2\beta_P^2|\mathbf{k}_s - \mathbf{k}'_s|k_{c0}) \\ &- 2|\mathbf{k}_s - \mathbf{k}'_s|k_{c0} I_1(2\beta_P^2|\mathbf{k}_s - \mathbf{k}'_s|k_{c0})],\end{aligned} \tag{H.18}$$

where I_0 and I_1 are Bessel functions of the second kind and we have approximated $[1 - f(\epsilon_{k'_s})] \approx 1$.

Bibliography

[1] E. Towe and D. Pan, IEEE J. Sel. Top. Quantum Electron. **6**, 408 (2000).

[2] D. Bimberg, M. Grundmann, and N. N. Ledentsov, *Quantum Dot Heterostructures* (John Wiley & Sons, New York, 1999).

[3] M. Grundmann, Physica E **5**, 167 (2000).

[4] O. B. Shchekin and D. G. Deppe, Appl. Phys. Lett. **80**, 3277 (2002).

[5] P. Borri *et al.*, IEEE J. Photon. Technol. Lett. **12**, 594 (2000).

[6] M. Sugawara *et al.*, Jpn. J. Appl. Phys. **40**, L488 (2001).

[7] R. Wang *et al.*, IEEE J. Photon. Technol. Lett. **13**, 767 (2001).

[8] R. Schwertberger, D. Gold, J. Reithmaier, and A. Forchel, IEEE J. Photon. Technol. Lett. **14**, 735 (2002).

[9] B. K. Ridley, *Quantum Processes in Semiconductors* (Clarendon Press, Oxford, 1988).

[10] L. A. Coldren and S. W. Corzine, *Diode Lasers and Photonic Integrated Circuits* (Wiley, New York, 1995).

[11] H. Bruus and K. Flensberg, Introduction to many-body quantum theory in condensed matter physics, Lecture notes (2002).

[12] V. I. Klimov, C. J. Schwarz, and D. W. McBranch, Phys. Rev. B **60**, R2177 (1999).

[13] V. I. Klimov, A. A. Mikhailovsky, S. Xu, and A. Malko, Science **290**, 314 (2000).

[14] T. Kurth, Ph.D. thesis, University of Hamburg, 1998.

[15] R. Nötzel, Semicond. Sci. Technol. **11**, 1365 (1996).

[16] K. Zhang *et al.*, Journal of Crystal Growth **227-228**, 1020 (2001).

[17] D. M. Bruls, J. W. A. M. Vugs, P. M. Koenraad, and H. W. M. Salemink, Appl. Phys. Lett. **81**, 1708 (2002).

[18] J. M. Luttinger and W. Kohn, Phys. Rev. **97**, 869 (1955).

[19] J. Y. Marzin and G. Bastard, Solid State Commun. **92**, 437 (1994).

[20] P. Lelong and G. Bastard, Solid State Comm. **98**, 819 (1996).

[21] R. Ferreira and G. Bastard, Appl. Phys. Lett. **74**, 2818 (1999).

[22] C. Pryor, Phys. Rev. B **57**, 7190 (1998).

[23] O. Stier, M. Grundmann, and D. Bimberg, Phys. Rev. B **59**, 5688 (1999).

[24] M. Holm, M.-E. Pistol, and C. Pryor, J. Appl. Phys. **92**, 932 (2002).

[25] L.-W. Wang, J. Kim, and A. Zunger, Phys. Rev. B **59**, 5678 (1999).

[26] J. A. Brum and G. Bastard, Phys. Rev. B **33**, 1420 (1986).

[27] S. M. Goodnick and P. Lugli, Phys. Rev. B **37**, 2578 (1988).

[28] P. W. M. Blom, J. E. M. Haverkort, P. J. van Hall, and J. H. Wolter, Appl. Phys. Lett. **62**, 1490 (1993).

[29] M. Preisel and J. Mørk, Phys. Rev. B **49**, 14478 (1994).

[30] H. Schneider and E. C. Larkins, Solid State Electron. **40**, 133 (1996).

[31] U. Bockelmann and G. Bastard, Phys. Rev. B **42**, 8947 (1990).

[32] H. Benisty, C. M. Sotomayor-Torres, and C. Weisbuch, Phys. Rev. B **44**, 10945 (1991).

[33] T. Inoshita and H. Sakaki, Phys. Rev. B **46**, 7260 (1992).

[34] U. Bockelmann and T. Egeler, Phys. Rev. B **46**, 15574 (1992).

[35] P. A. Knipp and T. L. Reinecke, Phys. Rev. B **52**, 5923 (1995).

[36] M. Braskén, M. Lindberg, and J. Tulkki, Phys. Stat. Sol. (a) **164**, 427 (1997).

[37] C. Cohen-Tannoudji, B. Diu, and F. Laloë, *Quantum Mechanics* (John Wiley & Sons, New-York, 1977), Vol. II.

[38] A. V. Uskov, J. McInerney, F. Adler, and H. Schweizer, Appl. Phys. Lett. **72**, 58 (1998).

[39] J. L. Pan, Phys. Rev. B **49**, 11272 (1994).

[40] A. V. Uskov, F. Adler, H. Schweizer, and M. H. Pilkuhn, J. Appl. Phys. **81**, 7895 (1997).

[41] H. Rücker, E. Molinari, and P. Lugli, Phys. Rev. B **45**, 6747 (1992).

[42] C.-Y. Tsai, C.-Y. Tsai, Y.-H. Lo, and L. Eastman, IEEE J. Quantum Electron. **31**, 2148 (1995).

[43] M. Grundmann *et al.*, Phys. Stat. Sol. (b) **203**, 121 (1997).

[44] T. W. Berg, S. Bischoff, I. Magnusdottir, and J. Mørk, IEEE Photon. Technol. Lett. **13**, 541 (2001).

[45] M. Grundmann and D. Bimberg, Phys. Rev. B **55**, 9740 (1997).

[46] T. W. Berg, S. Bischoff, I. Magnusdottir, and J. Mørk, in *Integrated Photonics Research* (OSA, Monterey, 2001), paper no. IMF3.

[47] J. Feldmann *et al.*, J. Appl. Phys. **89**, 1180 (2001).

[48] M. D. Giorgi *et al.*, Appl. Phys. Lett. **79**, 3968 (2001).

[49] I. Magnusdottir *et al.*, J. Appl. Phys. **92**, 5982 (2002).

[50] H. Haug and S. W. Koch, *Quantum Theory of the Optical and Electronic Properties of Semiconductors* (World Scientific, Singapore, 1990).

[51] M. Grundmann, O. Stier, and D. Bimberg, Phys. Rev. B **52**, 11969 (1995).

[52] L. V. Asryan and R. A. Suris, Appl. Phys. Lett. **74**, 1215 (1999).

[53] A. Vasanelli *et al.*, Physica E **11**, 41 (2001).

[54] T. Jonsson and J. Yngvason, *Waves and distributions* (World Scientific, Singapore, 1995).

[55] A. Franceschetti and A. Zunger, Phys. Rev. Lett. **78**, 915 (1997).

[56] T. Inoshita and H. Sakaki, Phys. Rev. B **56**, R4355 (1997).

[57] S. Hameau *et al.*, Phys. Rev. Lett. **83**, 4152 (1999).

[58] C. Weisbuch, M. Nishioka, A. Ishikawa, and Y. Arakawa, Phys. Rev. Lett. **69**, 3314 (1992).

[59] X.-Q. Li and Y. Arakawa, Phys. Rev. B **57**, 12285 (1998).

[60] X.-Q. Li, H. Nakayama, and Y. Arakawa, Phys. Rev. B **59**, 5069 (1999).

[61] O. Verzelen, R. Ferreira, and G. Bastard, Phys. Rev. B **62**, R4809 (2000).

[62] L. Jacak, J. Krasnyj, D. Jacak, and P. Machnikowski, Phys. Rev. B **65**, 113305 (2002).

[63] S. Sauvage *et al.*, Phys. Rev. Lett. **88**, 177402 (2002).

[64] T. Stauber, R. Zimmermann, and H. Castella, Phys. Rev. B **62**, 7336 (2000).

[65] O. Verzelen *et al.*, Jpn. J. Appl. Phys. **40**, 1941 (2001).

[66] C. Cohen-Tannoudji, J. Dupont-Roc, and G. Grynberg, *Atom-Photon Interactions* (John Wiley & Sons, New York, 1992).

[67] F. Vallée and F. Bogani, Phys. Rev. B **43**, 12049 (1991).

[68] I. Magnusdottir *et al.*, Appl. Phys. Lett. **81**, 4318 (2002).

[69] G. Bastard, Phys. Rev. B **30**, 3547 (1984).

[70] H. Luo *et al.*, Phys. Rev. Lett. **70**, 1307 (1993).

[71] D. Birkedal, K. Leosson, and J. M. Hvam, Phys. Rev. Lett. **87**, 227401 (2001).

[72] M. Preisel, Ph.D. thesis, University of Copenhagen, 1994.

[73] F. Adler *et al.*, J. Appl. Phys. **80**, 4019 (1996).

[74] B. Ohnesorge *et al.*, Phys. Rev. B **54**, 11532 (1996).

[75] S. Grosse *et al.*, Phys. Rev. B **55**, 4473 (1997).

[76] S. Marcinkevicius and R. Leon, Phys. Rev. B **59**, 4630 (1999).

[77] S. Raymond, K. Hinzer, S. Fafard, and J. L. Merz, Phys. Rev. B **61**, R16331 (2000).

[78] A. L. Efros, V. A. Kharchenko, and M. Rosen, Solid State Comm. **93**, 281 (1995).

[79] E. Segrè, *Nuclei and particles* (W. A. Benjamin, New York, 1964).

[80] H. C. Schneider, W. W. Chow, and S. W. Koch, Phys. Rev. B **64**, 115315 (2001).

[81] T. W. Berg, private communication, 2002.

[82] R. V. N. Melnik and M. Willatzen, in *Technical Proceedings of the MSM 2002 International Conference on Modeling and Simulation of Microsystems* (Nanoscience & Technology Institute, Danville, 2002), pp. 506–509.

[83] L. D. Landau and E. M. Lifschitz, *Quantum Mechanics*, 3rd ed. (Butterworth-Heinemann, Oxford, 1977).

[84] L. I. Schiff, *Quantum Mechanics* (McGraw-Hill, Singapore, 1968).

[85] A. Messiah, *Quantum Mechanics* (North-Holland Publishing Company, Amsterdam, 1961), Vol. I.

[86] J. D. Jackson, *Classical Electrodynamics* (John Wiley & Sons, New York, 1975).

[87] *Handbook of Mathematical Functions*, edited by M. Abramowitz and I. Stegun (Dover Publications, New York, 1970).